Temporal properties of gamma-ray bursts observed by *Swift*: indications of long-term central engine activity

Åsa Höglund

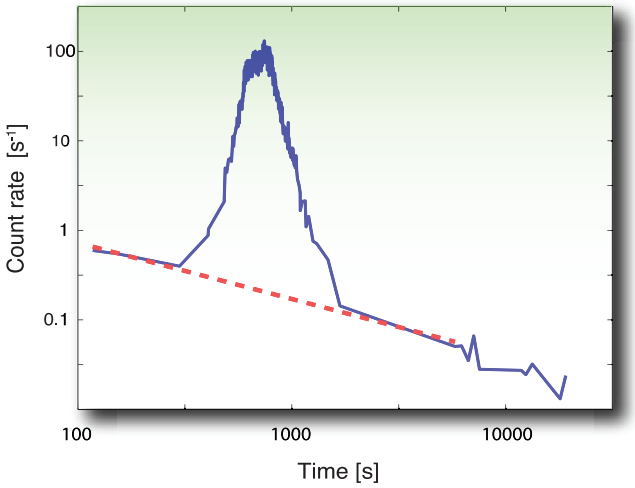

Master's Thesis 20 p

Department of Astronomy
Stockholm University

December 12, 2007

Abstract

Gamma-ray bursts (GRBs) are short and extremely energetic flashes of gamma-radiation. A typical light curve consists of gamma-ray pulses and a power law decaying afterglow of X-ray to optical wavelengths. In many light curves X-ray flares superimposed on the regular afterglow have been detected. The aim of this thesis is to determine the origin of these flares by conducting a morphological and temporal analysis of the pulses and flares, using *Swift* data. The sample consists of 27 gamma-ray pulses from 23 GRBs detected by *Swift's* BAT, and 27 X-ray flares from 15 GRBs detected by *Swift's* XRT. The pulses are fitted with the Kocevski, Ryde, Liang function.

I show that the temporal properties of the pulses and flares are very similar and that the intensity of the pulses and flares decreases with time. The flares have a rapid and large scale variability. The mean ratio between the width of the flares and the time of occurrence is 0.19 ± 0.09. The asymmetry of the pulses and flares are found to be described by the natural logarithm of the decay power law index. Furthermore, I find no correlation between the number of pulses and number of flares. In some cases pulses and flares occur simultaneously which implies that there is no clear dividing line between them. I therefore argue that the flares are created by a central engine that remains active for a long time, and not by external shocks. Possible explanations for the long-lasting activity of the central engine is fragmentation of the disk, and subsequent accretion, or a strong magnetic flux accumulated around the black hole that can stop the accretion flow.

The figure on the front page illustrates a part of the X-ray light curve of GRB 050502B containing a large flare. The red dashed line corresponds to an assumed emission underlying the flare. This flare is very strong with a peak flux of about 500 times that of the underlying afterglow.

Contents

1 Introduction **1**
- 1.1 Progenitor . . . 2
  - 1.1.1 The collapsar/hypernova model and the internal/external shock scenario . . . 3
    - 1.1.1.1 Evidence for the collapsar model . . . 5
- 1.2 Radiation processes . . . 6
  - 1.2.1 Black body radiation . . . 6
  - 1.2.2 Synchrotron radiation . . . 6
  - 1.2.3 Inverse Compton radiation . . . 7
  - 1.2.4 Pair annihilation . . . 8
- 1.3 The acceleration of charged particles in a relativistic shock . . . 8
- 1.4 Emission properties . . . 8
  - 1.4.1 Prompt phase . . . 9
  - 1.4.2 Afterglow phase . . . 10
- 1.5 X-ray flares . . . 13
  - 1.5.1 The origin of the X-ray flares . . . 14
    - 1.5.1.1 Refreshed shocks . . . 14
    - 1.5.1.2 Long-lasting central engine activity . . . 14
- 1.6 Effects that affect the pulse shape . . . 14
  - 1.6.1 Relativistic effects . . . 14
  - 1.6.2 The curvature effect . . . 15
  - 1.6.3 Redshift . . . 18
- 1.7 Aim of thesis . . . 18
  - 1.7.1 Outline . . . 18

2 Instruments and data **19**
- 2.1 Detection of gamma- and X-rays . . . 19
- 2.2 The *Swift* satellite . . . 19
  - 2.2.1 BAT – Burst alert telescope (15-150(350) keV) . . . 21
  - 2.2.2 XRT – X-ray telescope (0.2-10 keV) . . . 22
- 2.3 FITS files . . . 23

3 Method **24**
- 3.1 Background . . . 24
- 3.2 The analytical pulse function . . . 24
  - 3.2.1 The sensitivity of the pulse function . . . 26
- 3.3 Pulse analysis program . . . 26
  - 3.3.1 How to use `srice2.pro` . . . 28
- 3.4 The GRB sample . . . 29
  - 3.4.1 The BAT sample . . . 29
  - 3.4.2 The XRT sample . . . 32
- 3.5 Data reduction . . . 34

3.5.1 BAT data reduction . . . 34
3.5.2 XRT data reduction . . . 35

4 Results **39**
4.1 Comments about the results . . . 39
4.1.1 How to compute the rise and decay times . . . 40
4.1.2 The γ-ray and X-ray energy flux . . . 40
4.2 BAT pulse parameters . . . 40
4.2.1 The rise and decay indices . . . 40
4.2.1.1 Uncertainties in the rise and decay indices . . . 40
4.2.2 Properties of pulses with different pulse widths . . . 42
4.2.3 Properties of pulses occurring at different times . . . 42
4.2.4 The decay slope as a function of asymmetry . . . 43
4.2.5 Combinations of the rise and decay indices and the rise and decay times . . . 46
4.2.6 Redshift correction . . . 46
4.3 XRT pulse parameters . . . 46
4.3.1 The rise and decay indices . . . 46
4.3.2 Properties of pulses with different pulse widths . . . 47
4.3.3 Properties of pulses occurring at different times . . . 48
4.3.4 The decay slope as a function of asymmetry . . . 49
4.3.5 Combinations of the rise and decay indices and the rise and decay times . . . 50
4.4 Prompt emission – X-ray flare correlation . . . 50
4.5 Summary of results . . . 50

5 Discussion **54**
5.1 Pulse/double pulse and good/less good fits . . . 54
5.2 The rise and decay indices . . . 54
5.3 Properties of pulses with different pulse widths . . . 55
5.4 Properties of pulses occurring at different times . . . 55
5.5 The decay slope as a function of asymmetry . . . 57
5.6 Combinations of the rise and decay indices and times . . . 58
5.7 Number of emission episodes in BAT and XRT . . . 58
5.8 Other studies of the temporal properties of pulses and flares . . . 59
5.8.1 Studies of γ-ray pulses . . . 59
5.8.2 Studies of X-ray flares . . . 60
5.9 What are X-ray flares? . . . 61
5.10 Future prospects . . . 62

6 Conclusions **64**

Acknowledgments **66**

Bibliography **67**

A Data reduction scripts **70**
A.1 batlc.sh . . . 71
A.2 BAT_QMap.sh . . . 71
A.3 time-corr.sh . . . 72
A.4 short.sh . . . 72

B The pulse analysis program `srice2.pro` **73**
B.1 srice2.pro . . . 74

C BAT and XRT light curves **83**

D XRT light curves with assumed power law emission and background subtracted flares **87**

E BAT and XRT fit parameters **91**

Chapter 1

Introduction

Gamma-ray bursts (GRBs) are short and extremely energetic flashes of gamma radiation followed by an afterglow of slowly fading radiation in X-ray to optical wavelengths, sometimes with large flares of X-ray radiation super positioned. The pulses range in time from milliseconds to several minutes and are observed about once a day. The GRBs release an enormous amount of energy, about 10^{51} ergs assuming that the outflow is collimated, and are the most luminous events since the Big Bang. The GRBs are seen in all parts of the sky and at all distances. The isotropic GRB distribution over the sky can bee seen in figure 1.1, and it indeed indicates a cosmological origin (outside our galaxy). In addition, the mean redshift measured with the *Swift* telescope is 2.42 (Bagoly et al., 2006), so they are in fact at cosmological distances, and so they are probes of the early universe. The largest redshift ever measured of a GRB is 6.29 which means that the explosion occurred 12.8 billion years ago.

GRBs are observed by space telescopes since γ- radiation is unable to reach the earth's surface. The first GRB was detected in 1967 by the Vela satellites and since then several thousands have been detected, but their origin still puzzles astronomers. Nevertheless, the understanding of them, and their inner engines has recently increased much, due to the launch of the *Swift* satellite. *Swift* is a satellite which slews autonomously and rapidly to the source, and thereby makes rapid localizations of bursts, and makes multi wavelength observations of their afterglows. The rapid localizations also enable measurements of redshift. Observations indicate

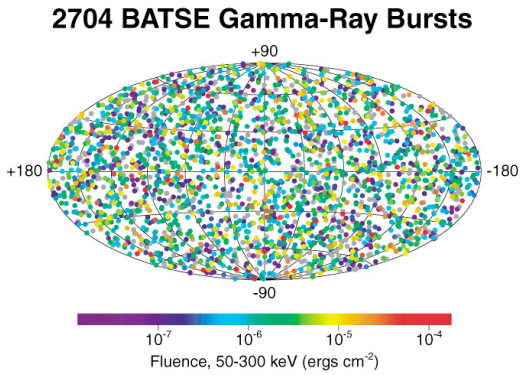

Figure 1.1: The distribution of 2704 gamma-ray bursts over the sky observed with the BATSE instrument on board the Compton gamma-ray observatory (CGRO) satellite. From: http://www.physics.rutgers.edu/ugrad/442/batse-sky.jpg.

that there are two main classes of GRBs, depending on the length of the pulses (Kouveliotou et al., 1993) but they are not entirely distinct. The burst duration versus the number of bursts detected by the BATSE instrument on board CGRO is displayed in figure 1.2(a). The CGRO satellite had an energy range of 20 keV to 30 GeV (the BATSE energy range was 10 keV to 100 MeV) and was working between 1991 and 2000. GRBs with durations shorter than two seconds have in general harder spectra (more photons of high energy) than the GRBs with duration longer than 2 seconds (Rosswog, 2004), but the distribution isn't distinct here either. The hardness is measured as the ratio of photons in a high and low energy channel. The correlation between the duration of the bursts and their hardness is displayed in figure 1.2(b) (BATSE data). HR is defined as the ratio between the fluence in the 100-300 keV energy band and the 50-100 keV energy band. (Fluence is time integrated flux.) The GRBs with durations less than two seconds are therefore

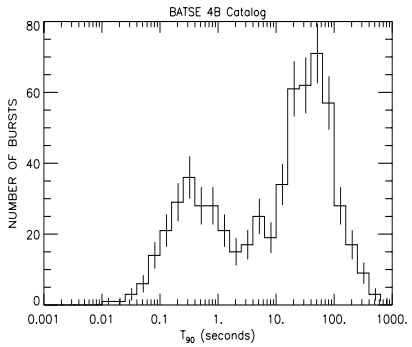

(a) The distribution of the burst duration. Two peaks can be seen at $\sim$ 0.3 s and $\sim$ 40 s. (From: http://www.batse.msfc.nasa.gov/batse/grb/duration/.)

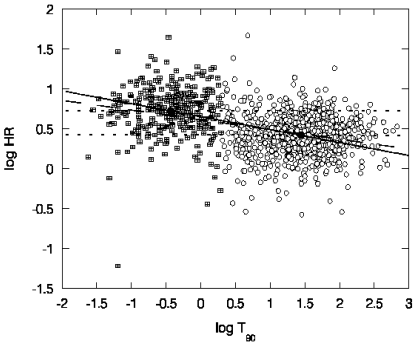

(b) The correlation between hardness and duration for burst from BATSE. HR is defined as the ratio of the fluency in the 100-300 keV energy band and that in the 50-100 keV energy band, and T_{90} is the time between which 5 and 95% of the flux is obtained. (Qin et al., 2000)

Figure 1.2: The distribution of burst duration and hardness- duration correlation.

called short and hard, and those with durations longer than two seconds are called long and soft. About two thirds of all GRBs are long GRBs. The short and hard bursts are thought to originate from a merger of a binary system of two neutron stars or a neutron star and a black hole (Mészáros (2001), Mészáros (2006)), while the long and soft bursts are assumed to arise from very massive and rapidly rotating stars whose cores collapses to black holes. The latter scenario is referred to as the collapsar/hypernova model and it is described more thoroughly in section 1.1.1. In this model, while the black hole is forming a blast wave of material and radiation is sent out, in narrow jets with opening angles of about 2-20° (Sari et al., 1999). This implies that a large fraction of bursts are never seen. Frail et al. (2001) estimates that the GRB rate should be at least 500 times larger than observed rate today. The observed fluxes range from 10^{-7}–10^{-4} erg cm^{-2} s^{-1}, which corresponds to total energies of about 10^{51} ergs.

1.1 Progenitor

In order to explain the origin of the long bursts several models have been developed. One of the most accepted theories is the collapsar/hypernova model, in which the GRB is thought to originate from a supernova- like event, when the core of a

very massive and rapidly rotating star collapses to a black hole. The in-falling material from the core creates an accretion disk due to the star's rotation, which in turn creates a relativistic jet which pushes through the core, and the outer stellar envelope, and escapes along the direction of the rotation axis. (Mészáros, 2006), while the outer layers of the stars explode in very energetic kinds of supernovae, called hypernovae. The star is called a collapsar. An artists illustration of a collapsar is shown in figure 1.3. The process is described more thoroughly below.

Stars at the end of their lifetime seize to create radiation by fusion in their cores. This means that the gravitational pull from the stellar material no longer is balanced by the radiation pressure. If the mass of a star is greater than about 8 solar masses it explodes in a supernova to form a neutron star or a black hole, but if the star is at least 40 solar masses (Nomoto et al., 2007) it collapses differently from a supernova, it explodes in a hypernova, releasing about 100 times as much energy as an ordinary supernova. For a star to create a GRB the mass thus has to be approximately 40 solar masses. The properties of the stars that create GRBs are described by Woosley & Heger (2006). In addition to being massive the star has to be rotating very rapidly (one to two orders of magnitude larger than for most common pulsars (Woosley & Heger, 2006)) in order to create the accretion disk and therefore the jets. The accretion disk has to be be massive. The inner engine must continue with the process for a long time since some of the bursts are long (up to 100 s). In order to let the jet reach the surface the outermost layer (hydrogen-layer) of the star must have been blown away before (by a stellar wind) – it has to be a Wolf-Rayet star. These criteria bring that GRBs occur less often than ordinary supernova explosions ($\sim 1\%$ of all supernovae are hypernovae). Only about 10^{-6} of all stars creates GRBs (Mészáros, 2001) at the end of their lifetime.

1.1.1 The collapsar/hypernova model and the internal/external shock scenario

In the collapsar/hypernova model a black hole is created from a very massive and rapidly rotating star while the outer layers of the star explodes in a very energetic supernova explosion, called a hypernova explosion. Due to the rapid rotation of the star the in-falling material of the core creates an accretion disk around the rotation axis. Material in the star close to the rotation axis has a smaller momentum than the material far away from the axis. This material falls into the accretion disk, which creates a funnel in the star with low density along the rotation axis.

When the material falls down to the accretion disk potential energy is released, and radiation is produced. There is also spin energy of the black hole. This energy can be extracted and follow magnetic field lines out through the star in a process called the Blandford Znajek process. Of the material from the accretion disk some is absorbed by the black hole but some is pushed by the photons out from the star through the funnel. This matter and energy escapes through the star along the direction of the rotation axis, because there the density of stellar material is the lowest. It creates a blast wave of stellar material and radiation. When the blast wave encounters material in the star γ-ray photons are created due to turbulence, but since the surroundings are optically thick, the photons can't escape. The blast wave continues out from the star and pushes the stellar material outwards. When it reaches the surface of the star it is released as relativistic jets with velocities close to the speed of light. Figure 1.4 displays the density and the energy density at the black hole. In figure 1.5 the process is described schematically. It could be that the accretion rate is not uniform and therefore the material and radiation is not continuous but released as numerous shells with different Lorentz factors Γ. (The Lorentz factor Γ is a measurement of the velocity of particles moving at relativistic velocities: $\Gamma = (1-\beta^2)^{-1/2}$, where $\beta = v/c$, v the velocity of the particle, and c the

Figure 1.3: An illustration of a collapsar. From: www.astro.psu.edu/users/nnp/grb.html.

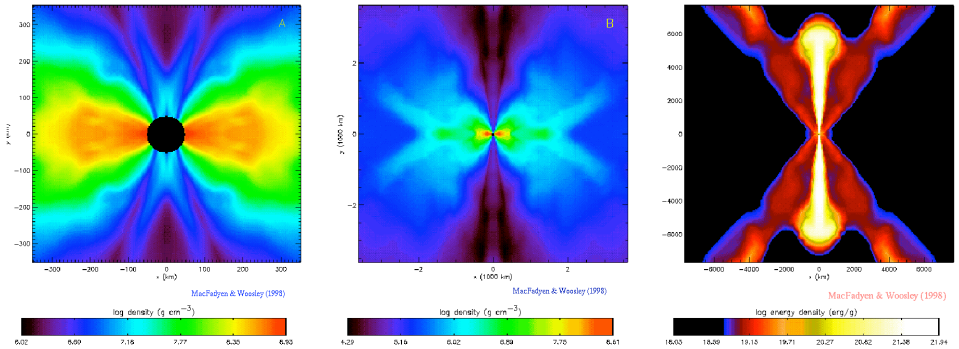

(a) The density structure at the accretion disk at 7.6 seconds. (From a model from MacFadyen & Woosley (1999).)

(b) The density structure at the accretion disk at larger scale at 15.63 seconds. (MacFadyen & Woosley, 1999).

(c) A model of the energy density at the black hole. (MacFadyen & Woosley, 1999)

Figure 1.4: The energy density and density at the progenitor star.

speed of light. Γ is used to describe the velocity of a bulk motion, while γ is used to describe the velocity of single particle.) Alternatively instabilities created as the jet moves through the star lead to a variable outflow from the star (simplified as shells). When a faster shell catches up with a slower one a shock is created. A shock is a propagating disturbance which is created when the properties of a medium changes abruptly, for example when the density suddenly increases due to an explosion.

In the collision between two shells synchrotron γ-ray photons are created from electrons in the impact (see section 1.2.2). These photons can then be up-scattered to higher temperatures by the inverse Compton effect (see section 1.2.3). The shocks created due to the collision of the shells in the jet are called internal shocks.

Two shells which have collided create a merged shell which continues to move outwards. Finally all the shells ejected from the star have merged into a single shell which is moving outwards into the interstellar medium. When this shell collides with the interstellar medium a shock is created, called the external shock. Behind the shock energy is dissipated and radiation is emitted through synchrotron emission. It is assumed that part of the dissipated energy creates magnetic fields and another part goes into accelerating particles (leptons, which then cool by emitting synchrotron radiation). See section 1.3. The interaction of the shell with the interstellar medium is what produces the afterglow. As the shell ploughs up material

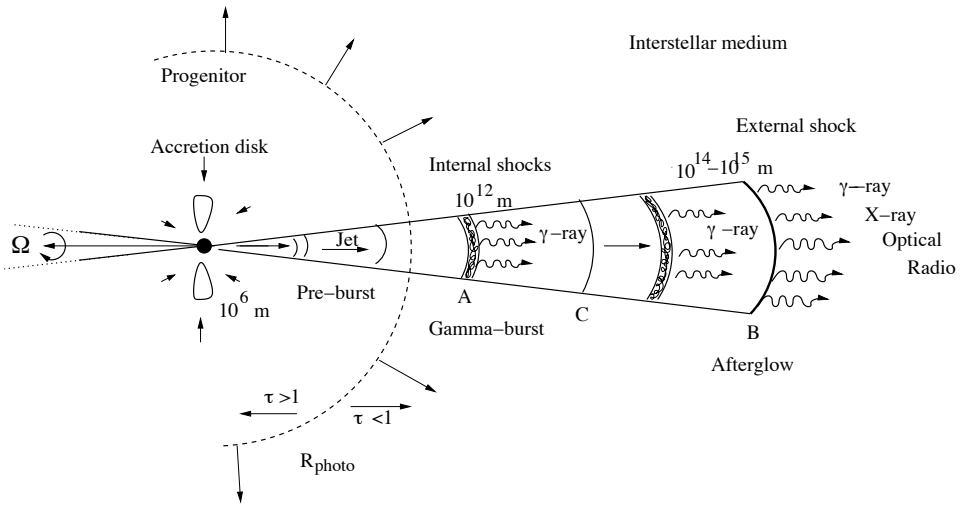

Figure 1.5: The collapsar/hypernova model. A jet beam ejecting from a rapidly spinning star forming a black hole. Shells sent out from the star colliding with each other create γ-rays. The letters A, B and C are connected to the corresponding A, B and C in the light curve of the scenario in figure 1.6.

in front of it, it transfers kinetic energy to the particles behind the shock. When the material cools it emits photons by for example synchrotron radiation. As the shell transmits energy to the ploughed up material it itself loses its kinetic energy and therefore contribute with less and less energy to the material behind it as it travels further out from the progenitor, which makes the afterglow radiation fade. This happens at a distance of $10^{14} - 10^{15}$ m from the center.

The above is called the internal-external shock scenario. The γ-ray pulses are thought to be created from internal shocks (within the jet) and the afterglow and X-ray flares are suggested to be created from an external shock (from the interaction of the outermost shell with the interstellar medium). A problem with the internal-external shock scenario is however the efficiency. The bulk kinetic energy of the shell is not converted to energy density with a high efficiency (Beloborodov, 2001). It would require a very high velocity of the shell in order to obtain such strong magnetic fields necessary to create the high energy synchrotron radiation emitted. Nevertheless, much evidence speak for the model.

1.1.1.1 Evidence for the collapsar model

There are several indications that supernovae are connected to the GRBs. One is that when a GRB has occurred several times radiation from supernovae has been observed from the same region of the sky, after the afterglow has faded away. This makes it probable that the supernova and the GRB originate from the same object. The supernova 1998bw was found at approximately the same position as GRB 980425, and the explosions took part with less than a day between. According to van Paradijs (2001) it would be a probability of less than 10^{-6} for this to be a coincidence. Additionally, the GRBs are often observed in active star forming regions, such as in irregular galaxies or in the arms of spiral galaxies, which contribute more supernovae. Star forming regions contain massive stars. Since massive stars evolve fast they are never found in regions where the star formation has stopped long ago. The fact that only massive stars create supernovae is also consistent with theory. Furthermore, the supernovae that have been found to be connected to a GRB lack hydrogen absorption lines in their spectra, which is consistent with that the star

has lost its outer layers of hydrogen. GRB 030329 exploded so close that its optical spectrum could be taken, and it was very similar to that of SN1998bw. Additionally, X-ray observations display signatures of oxygen heated to high temperatures, which would happen when a supernova explosion would heat oxygen atoms. It can be noted however that not every GRB is followed by the emission of a supernova (for example GRB 011121) which could pose a problem to the collapsar model in its simplest version.

1.2 Radiation processes

It is believed that the radiation created in GRBs is from synchrotron radiation or inverse Compton scattering. Gamma-rays can also be produced by pair annihilation. Another process concerning GRBs is black body radiation.

1.2.1 Black body radiation

If the electrons in a gas mainly interact through collisions they are said to be in thermal equilibrium, and a Maxwell-Boltzmann distribution of their speeds is obtained. The temperature T of the gas is then expressed as $T = 3k < v >^2 /2$, where k is Boltzmann's constant and v the speed of each electron. The Maxwell-Boltzmann function is a probability density function. The function is showed in equation 1.1 for a distribution of speeds (m is the electron mass).

$$f(v) = 4\pi \left(\frac{m}{2\pi kT}\right)^{\frac{3}{2}} v^2 e^{\frac{-mv^2}{2kT}} \tag{1.1}$$

If the photons also are in thermal equilibrium with the electrons (it is optically thick) their spectra is described by a Planck spectra. This is often also called a thermal spectrum. In thermal equilibrium there is no transport of radiation. The intensity of the radiation depends only on the temperature and it is described by the Planck function B_ν:

$$B_\nu(T) = \frac{2\nu^2}{c^2} \cdot \frac{h\nu}{e^{\frac{h\nu}{kT}} - 1}. \tag{1.2}$$

(ν is the frequency of the radiation and h is Planck's constant.)

1.2.2 Synchrotron radiation

Relativistic electrons in a magnetic field emit synchrotron radiation. (Non relativistic electrons produce cyclotron emission.) The magnetic field causes the electrons to gyrate which causes them to radiate due to the acceleration. An electron with Lorentz factor γ_e traversing a magnetic field will emit radiation with the frequency

$$\nu_{syn} = \frac{3}{2} \cdot \frac{q_e B_\perp}{m_e c} \gamma_e^2, \tag{1.3}$$

where $B_\perp$ is $B\sin\alpha$, where α is the pitch angle, q_e and m_e is the charge and mass of the electron respectively and c is the speed of light. This means that electrons of higher Lorentz factors emit higher energy photons. An electron that emits radiation loses kinetic energy. The power radiated by an synchrotron-electron is

$$P_{syn} = \frac{4}{3} \sigma_T c \beta^2 \gamma_e^2 U_B, \tag{1.4}$$

where σ_T is the Thompson cross section, $\beta = v/c$, with v being the velocity of the electron and U_B the energy density in the magnetic field ($U_B = B^2/8\pi$). This is

typically a high power, or cooling rate, which means that the synchrotron emission process converts kinetic energy from the electrons to radiation very efficiently. That means that synchrotron emission is important. The cooling time of an electron is (since $P \sim E/t \Rightarrow t \sim E/P$)

$$t_{syn} = \frac{\gamma_e m_e c^2}{P}. \tag{1.5}$$

As the electron spiral around the magnetic field line it radiates. An electron moving at a relativistic velocity emits radiation that is beamed in the direction of the velocity. An observer will see a pulse of radiation in the shape of a cone with width $\sim 2/\gamma_e$ (where γ_e as above is the Lorentz factor of the electron). The frequency distribution of this light pulse is given by the synchrotron function (Rybicki & Lightman , 1979).

Electrons are usually assumed to be distributed as a power law distribution of Lorentz factors due to acceleration mechanisms. All of these electrons radiate and produce the synchrotron radiation that is observed. A power law (expressed as $y = x^p$) distribution is described by equation 1.6. Typical values of p are 2 or 3.

$$N(\gamma_e) = N_0 \gamma_e^{-p}. \tag{1.6}$$

Since synchrotron radiation is emitted from several electrons with different Lorentz factors the observer sees different frequency distributions. These are approximated by δ functions. The sum of the individual δ functions makes the total synchrotron spectrum. This is also a power law. The slope of the synchrotron spectrum depends on the slope of the electron (power law) distribution. The spectral index s of the photon power law distribution is defined as $s = (p-1)/2$.

All the photons from the emitted synchrotron radiation do not always reach the observer. The photons can scatter against the same electrons that produced the synchrotron emission (the surroundings are optically thick). This means that an observer only sees the emission from a layer near the surface, much less than if all synchrotron photons had escaped, and the flux in the spectra is thus reduced. A low energy photon is absorbed with higher probability than a high energy photon. For photons of higher and higher energy the effect is less – the observer sees more photons of higher energies, so the effect is mostly visible in the low-frequency part of the spectrum. This effect is called synchrotron self absorption. It creates a break in the spectrum, where the optical depth, $\tau = 1$, corresponding to where the mean free path is about the size as the blast wave.

1.2.3 Inverse Compton radiation

Inverse Compton scattering takes place when a photon collides with a moving electron. If the moving electron has sufficient kinetic energy compared to the photon energy may be transferred from the electron to the photon. The power emitted by an electron of kinetic energy $\gamma_e mc^2$ is given by

$$P_{Com} = \frac{4}{3}\sigma_T c \beta^2 \gamma_e^2 U_{rad}, \tag{1.7}$$

where U_{rad} is the energy density in radiation. Multiple scatterings can produce a noticeable change in the photon energy. Comptonization is when low energy photons with energy ϵ_i are scattered to higher energies by multiple scattering of electrons with energy $kT > \epsilon_i$. The relative change in energy of escaping photons is defined by the Compton y-parameter.

A power law distribution of electrons produces a power law distribution of photons. See Rybicki & Lightman (1979). The inverse Compton spectra, similar to

the synchrotron spectra, is composed of frequency distributions with lower intensity at higher energy. An addition of them creates a power law.

Synchrotron photons that have been up- scattered by the inverse Compton process (by the same electrons that produced the synchrotron emission) can obtain high energies. This process is called synchrotron-self-Compton.

1.2.4 Pair annihilation

When an electron and a positron collide two or more γ-ray photons can be created. Most commonly two photons are created, each with an energy which equals the rest energy of the electron or positron (511 keV). The process is common in environments with very high electron and positron densities. The process with two photons created is described by the relation

$$e^+ + e^- \rightleftarrows \gamma + \gamma. \tag{1.8}$$

1.3 The acceleration of charged particles in a relativistic shock

It is thought that the bulk kinetic energy of the shells is partitioned into energy in electrons (U_E) and to magnetic energy density (U_B) in the collision between them. The energy density in electrons means that the electrons get a random motion. The creation of magnetic energy density means that magnetic fields are created, since $U_B = B^2/8\pi$. It is believed that the magnetic fields are created through amplification of fluctuations in the jet plasma, by a mechanism dubbed the "relativistic mixed mode instability" (see Frederiksen et al. (2004)). The shells consist of plasma with electrons, positrons and protons, and these are surrounded by electric and magnetic fields. When fluctuations occur in these electromagnetic fields, due to displacements between the electrons and protons, the magnetic field strength varies. From the co-moving frame of a shell, particles with relativistic velocities (from the other shell) hit the shell. The variation of the magnetic field strength means that the charged particles assemble at different places in the plasma, and current channels are created. These are drawn to each other and thus creates a larger electric field. A larger electric field means a larger magnetic field, and as the magnetic field strength increases more and more charged particles are assembled in the current channels. It is a self-amplifying process.

A large magnetic field means that there is a large force on the charged particles, since the Lorentz force is described by $\bar{F} = q(\bar{E} + \bar{v} \times \bar{B})$, and particles affected by a large force are accelerated much.

1.4 Emission properties

The general behavior of a light curve is shown in figure 1.6. It consists of a prompt phase of γ-ray pulses (A in figure 1.6) and an afterglow phase of fading X-ray and UV radiation (B in figure 1.6). In about 50% of the bursts large X-ray flares are super positioned on the afterglow (O'Brien et al. (2006), Burrows et al. (2006)) (C in figure 1.6).

Each pulse in the prompt phase is assumed to be caused by a distinct emission episode. One possibility is that a pulse is produced in every shell collision due to synchrotron emission, or it directly reflects the variability of the central engine.

The X-ray flares are assumed to be created either from refreshed shocks, by slow shells ejected during the prompt phase that catch up with the afterglow at late

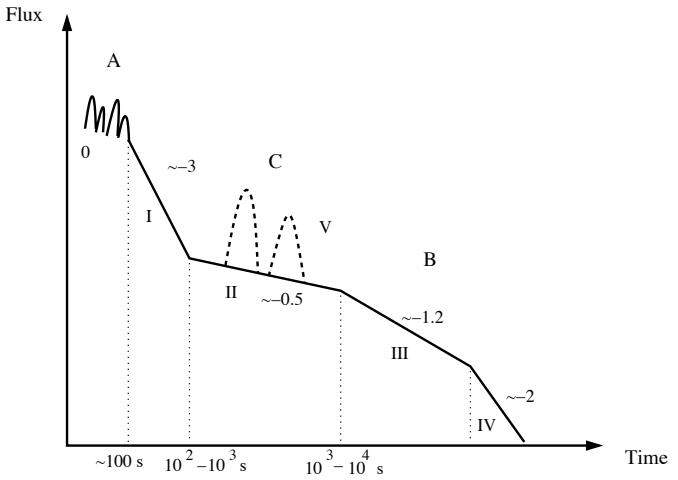

Figure 1.6: A schematic X-ray afterglow light curve (plotted in a log-log graph) based on data from the *Swift* XRT. (Based on Zhang (2006a).) A, B and C corresponds to A, B and C in figure 1.5. A describes the prompt emission with γ-ray pulses. B displays the decaying afterglow in X-ray and optical wavelengths. In about half of all GRBs observed X-ray flares are super positioned on the afterglow light curve (C)).

times, or internally in the jet from shells emitted after the prompt emission. In this case the central engine is believed to stay active for a long time, or be re-started.

1.4.1 Prompt phase

The radiation from the prompt phase is believed to be synchrotron radiation. The spectra of the prompt phase are often described by the Band model, which is a smoothly broken power law. The Band model is an empirical relation but could occur due to synchrotron radiation. The Band function is described by the relation (Willingale et al., 2007):

$$F(E) = \begin{cases} E^{-\beta_X} e^{-\frac{E}{E_c}}, & E \leq E_c(\beta_\gamma - \beta_X) \\ E^{-\beta_\gamma} e^{\beta_\gamma - \beta_X} \cdot ((\beta_\gamma - \beta_X) \cdot E_c)^{\beta_\gamma - \beta_X}, & E \geq E_c(\beta_\gamma - \beta_X), \end{cases} \tag{1.9}$$

where β_X and β_γ are the spectral indices for the two power laws (at low and high energy) and E_c is the break energy. An example of a spectrum fitted with the Band model is given in figure 1.7. The example is from M. Battelino's masters thesis at Stockholm University.

When the burst proceeds, the spectrum of a burst often gets softer. Two empirical relations have been found that describe this softening; the hardness-intensity correlation (HIC) and the hardness-fluence relation (HFC). The HIC relates the instantaneous peak energy E_p of the spectra and energy flux F and is expressed as

$$F(t) = F_0 \left(\frac{E_{pk}(t)}{E_{pk,0}} \right)^\eta \tag{1.10}$$

where F_0 is the initial value of the flux and $E_{pk,0}$ the initial value of the peak energy. The index η is the relation index. The HFC relates the peak energy and the time-integrated photon flux, and is expressed as

$$E_{pk}(t) = E_{pk,0} e^{-\frac{\phi(t)}{\phi_0}}, \tag{1.11}$$

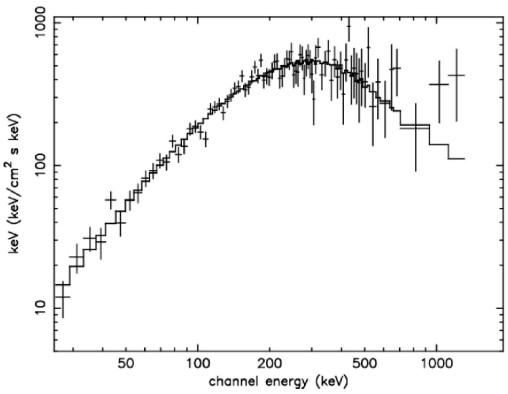

Figure 1.7: An example of a spectrum fitted with the Band function.

where $E_{pk}(t)$ is the peak energy at time t in the spectrum, $\phi(t) \equiv \int_0^t F(t)dt \quad [cm^{-2}]$ is the photon fluence integrated from the time 0, where $E_{pk}(t) = E_{pk,0}$. ϕ_0 is an exponential decay constant.

At first the emitted radiation in the blast wave is optically thick, but as the blast wave expands it eventually gets optically thin. The prompt emission spectra so should contain a thermal component from the photosphere. The spectra have by Ryde (2005) been suggested to be a hybrid model of a black body and a power law.

The light curves of the bursts show a large diversity and neither of them looks the same. Examples of prompt emission light curves can be seen in figure 1.8.

1.4.2 Afterglow phase

After the initial burst of gamma radiation from a GRB, radiation of lower frequencies can usually be observed. This radiation ranges from X-ray and optical to radio, and is called the afterglow. The afterglow emission slowly fades with time but can be detected for weeks, months or even years after the GRB. An afterglow follows after almost every GRB and it is the afterglow that has provided most of the information about them. For example measurements of redshifts, and therefore distances and absolute luminosities, has been possible to determine due to the detection of the afterglow, which has shown that most of the GRBs occur at cosmological distances, that is billions of years ago. Additionally, after the afterglow has faded away emission from the host galaxy can in many cases be observed, which can provide information about the types of galaxies where the GRBs occur. The afterglow emission is less luminous than the actual GRB emission. However, some flares can contain as much energy as in the prompt phase.

The afterglow is assumed to be synchrotron emission from electrons accelerated when the shell at front of the jet collides with the external medium (the external shock). The collision with the interstellar medium supplies energy to the electrons behind the shock, which makes the shock lose its kinetic energy. While the shock is slowing down less energy is transmitted to the electrons behind the shock and so the luminosity of the afterglow decreases. Electrons are assumed to be accelerated into a power law distribution of the Lorentz factors γ_e in the blast wave.

Both the light curve and the spectrum of the afterglow consist of several power law segments. The spectrum of the afterglow consists of four power law segments (with three break points). Two separate spectra can be obtained. These are described in equations 1.12 and 1.13. One is shown in figure 1.9.

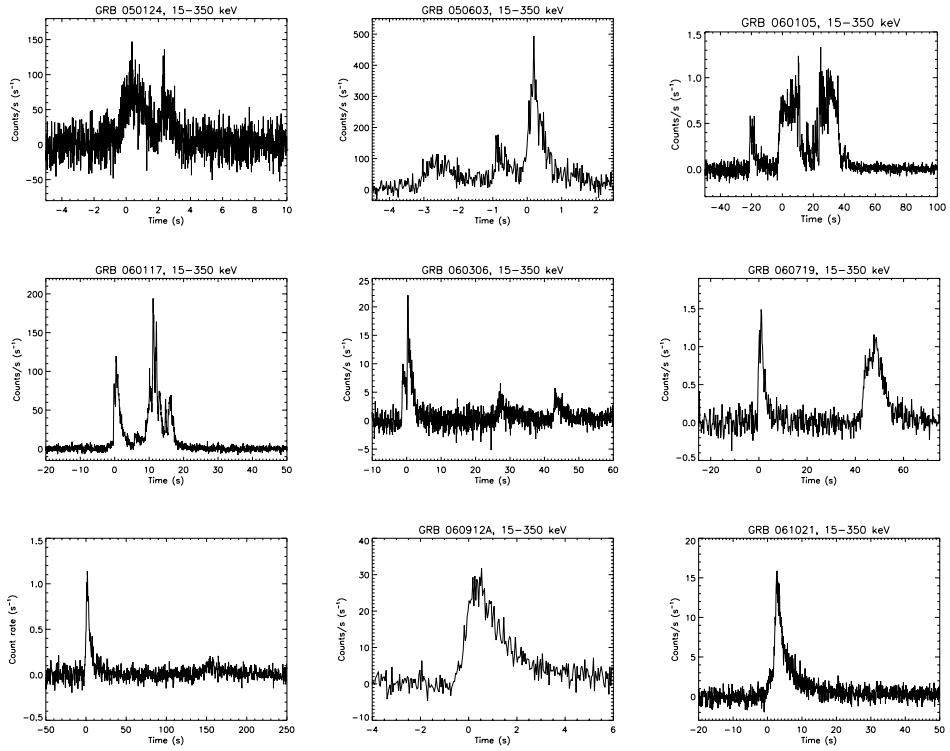

Figure 1.8: A sample of nine light curves from the *Swift* satellite. The flux variation and the length of separate GRBs differ much, as do the shapes of the pulses.

Fast cooling:

$$F_\nu \propto \begin{cases} \nu^2, & \nu < \nu_a \\ \nu^{1/3}, & \nu_a < \nu < \nu_c \\ \nu^{-1/2}, & \nu_c < \nu < \nu_m \\ \nu^{-p/2}, & \nu_m < \nu \end{cases} \tag{1.12}$$

Slow cooling:

$$F_\nu \propto \begin{cases} \nu^2, & \nu < \nu_a \\ \nu^{1/3}, & \nu_a < \nu < \nu_m \\ \nu^{-(p-1)/2}, & \nu_m < \nu < \nu_c \\ \nu^{-p/2}, & \nu_c < \nu \end{cases} \tag{1.13}$$

The break points are:

$\nu_a \equiv \nu(\gamma_a)$ is the lowest break point which corresponds to the frequency below which the GRB is optically thick, $\tau > 1$. Below this frequency there is self absorption of the synchrotron photons by the electrons. The spectrum gets the form of Rayleigh- Jeans - black body radiation and is proportional to ν^2.

ν_m is related to the minimum energy an electron has after it has passed the shock.

ν_c is the cooling frequency, where the efficiency of cooling compared to acceleration of the electrons is larger.

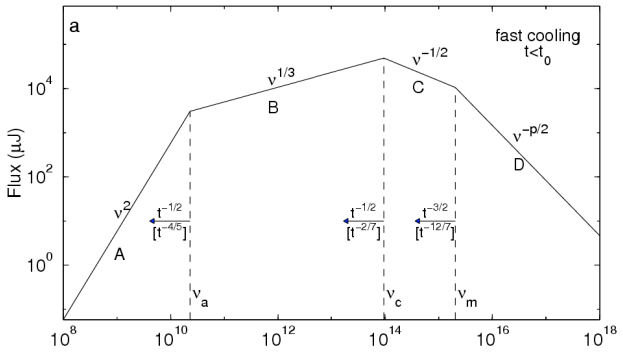

Figure 1.9: Synchrotron fast cooling spectrum of a relativistically moving shock from electrons distributed as a power law. Fast cooling is expected at early times after the burst (Granot et al., 2000) and slow cooling is expected at later times (Sari et al., 1998).

Which of the two spectra that are observed depends on if the frequency $\nu_m > \nu_c$ (fast cooling) or if $\nu_c < \nu_m$ (slow cooling). At early times the electrons cool with fast cooling but at later times with slow cooling. This is because ν_c eventually gets larger than ν_m.

Observations of the afterglow light curves can provide information about the origin of the prompt emission, for example the GRB surroundings and the activity of the central engine. Different afterglow light curves differ from one another but they are all composed of several, but not necessarily all, of the following components (Zhang, 2006a). The results correspond to X-ray light curves and are from *Swift*. This is also presented in figure 1.6.

0. Prompt phase: The phase ranges from milliseconds to a couple of hundreds of seconds and consists of gamma radiation. (This was known before *Swift*.)

I. Steep decay phase: The decay slope is about -3 or steeper, which usually differ from the other afterglow phases. The phase is usually connected to the prompt emission and extends to about 10^2 – 10^3 s.

II. Shallow decay phase: The decay slope is typically ~ -0.5 or flatter and the phase extends to 10^3 – 10^4 s. It could be explained by refreshed shocks. (See section 5.9 for a description about refreshed shocks.)

III. External shock emission: Usually the decay slope is about -1.2. (Known before *Swift*.)

IV. Post Jet break phase: The phase usually has a decay slope of -2. (Known before *Swift*.)

V. X-ray flares: About half of all GRBs (both long and short) have X-ray flares super positioned on the afterglow (Zhang (2006a), Mangano et al. (2007), O'Brien et al. (2006)), which are characterized by very steep rising and decaying slopes. See section 5.9 for more characteristics about these flares, and their possible origin.

It is widely believed that the emission from GRBs is synchrotron radiation created in relativistic jets when shells of different Γ collide (Rees & Mészáros, 1994). Relativistically moving electrons from the blast wave produce relativistically beamed radiation with angle $\sim 2/\Gamma$ in the direction of the velocity. This

means that only a surface area of the jet front subtended by an angle $\sim 2/\Gamma$ will be visible to the observer. As the jet slows down more and more of the surface will be seen. When the surface seen by the observer gets larger than the surface of the jet there is no more photons from a larger part of the jet seen by the observer. This is seen as a break in the light curve.

The steep decay phase is interpreted as the tail of the prompt emission (Zhang et al., 2006c) which suggests that the prompt emission and the afterglow are two distinct events, and which supports the idea that the prompt emission is of internal origin. Figure 1.10 shows a light curve obtained from a *Swift* observation.

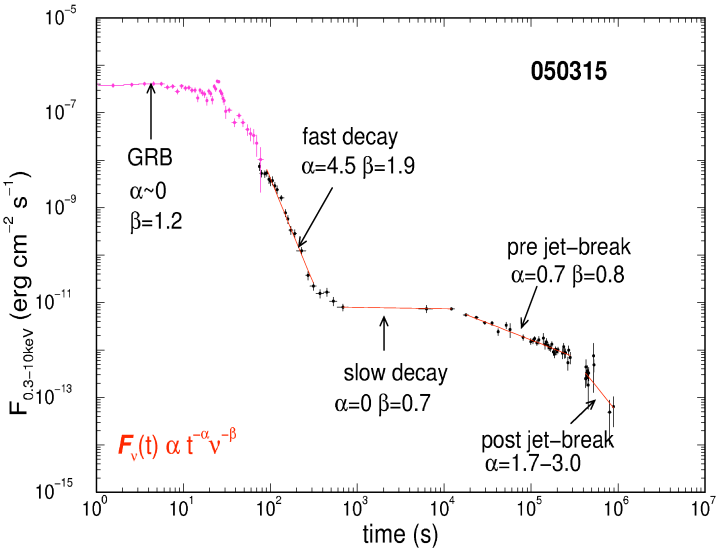

Figure 1.10: A *Swift* X-ray afterglow light curve. From Panaitescu (2006). As can be seen in the figure the flux is expressed as $F_\nu \propto t^{-\alpha}\nu^{-\beta}$. The index α describes the slope of the flux in the light curve while β is the spectral index.

1.5 X-ray flares

One of the most interesting components of the afterglow light curves are the X-ray flares that are detected at about $10^2 - 10^5$ s after the GRB prompt emission in nearly half of all GRBs, both long and short ones. Properties of the flares are:

1. The flares have rapid rise and fall times.
2. The slope underlying the flares is often the same before and after the flare.
3. The flux increases can be large. (For GRB 050502B there was about a factor of 500 increase in the flux from the afterglow (Falcone et al., 2006).)
4. Sometimes flares occur days after the prompt emission.
5. Multiple flares exist in some GRBs.
6. Typically, the fluence of the flares decrease with time and they get wider with time.
7. Flares exist in both long and short GRBs.

1.5.1 The origin of the X-ray flares

There are mainly two models that explain the existence of flares in the afterglows of GRBs, the refreshed shock model and the long-lasting central engine model.

1.5.1.1 Refreshed shocks

In the refreshed shock model slow shells ejected during the prompt phase are assumed to catch up with the afterglow at late times, which would cause a re-brightening of the afterglow. This is what is assumed to create the shallow decay part of the light curve (after $10^2 - 10^3$ s). Arguments that speak in favor of this model is that the decline of the steep decay part in the afterglow is so large that the source must have been switched off quickly (Kumar et al., 2007). There is nevertheless problems with this model also. A question is whether a slow shell can create the large flux that some of the flares have. The energy creating the flares need to be comparable to that of the initial blast wave.

1.5.1.2 Long-lasting central engine activity

The long-lasting central engine activity model assumes that the central engine remains active for days, or is re-started. This means that the flares are from internal origin. The model is good at explaining the large fluxes, and the rapid rise and decay times of the flares. Additionally, that the slope of the emission underlying the flares often is the same before and after the flares points to that this emission and the flares come from different processes. An argument against the model is that it is hard to explain large flares that occur several hours after the prompt emission, since the accretion process is over in a short time (Woosley, 1993).

1.6 Effects that affect the pulse shape

Several processes exist, which alter the shapes of the pulses so that the observed pulses look different than what the pulses did when they were emitted. There are relativistic effects, effects due to the curvature of the jet and redshift.

1.6.1 Relativistic effects

Relativistic effects has to be taken into account since the jet released from the GRB is moving at a relativistic velocity. From the theory of relativity we know that observed energy appear larger than when emitted and times appear larger than in the co-moving frame. The size of the change depends on the Γ factor in the direction of the observer between the observers coordinate system and the system of the jet. $\mathcal{D}$ describes the Γ factor with account taken for the angle θ from the line of sight. The definition of $\mathcal{D}$ is

$$\mathcal{D} \equiv \frac{1}{\Gamma(1 - \beta\mu)}, \tag{1.14}$$

where $\mu = \cos\theta$ (for the angle θ in figure 1.12(a)). The observed energy from a system moving relativistically is described by

$$E = E' \cdot \mathcal{D} \tag{1.15}$$

where E' is the energy in the co-moving system and E the energy in the observers system. Similarly, the observed time is described by $t = t' \cdot \mathcal{D}$ (with t' being the time in the co-moving system and t the time in the observers system). The effect is called time dilation. But since the jet is moving relativistically in the same direction as it emits photons the Doppler effect also has to be taken into account.

The situation is shown in figure 1.11. Two photons are released from the shell in the co-moving frame at time t'_1 and t'_2. The time difference between the releases (in the co-moving system) is thus $t'_2 - t'_1$. During the time the shell emits the photons it moves against the observer. It will thus be closer to the observer when the second photon is emitted. Though there is a specific time interval between that the two photons are released, the second photon has a shorter way than the first photon to travel to the observer, which means that the time for it to reach the observer is shorter. The second photon will thus be observed at a earlier time than it would have been if the shell hadn't moved, and the observed time $\Delta t = t_1 - t_2 \neq \Delta t'$. This is described by the relativistic Doppler effect. It includes the time dilation effect and is described in equation 1.16.

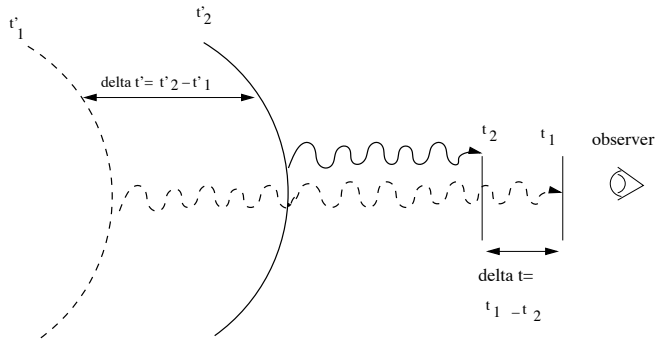

Figure 1.11: A schematic illustration of the relativistic Doppler effect.

$$t = \frac{t'}{2\mathcal{D}^2} \tag{1.16}$$

The relativistic Doppler effect thus changes the appearance of the observed pulse to look narrower than when it was emitted.

Since flux is a measure of energy per unit time and area, the observed flux is also affected by these changes. The observed flux is, since $E = E' \cdot \mathcal{D}$ and $t = t'/2\mathcal{D}^2$, expressed as

$$F = 2F' \cdot \mathcal{D}^3, \tag{1.17}$$

where F is the energy flux in the observers frame, and F' is the corresponding quantity in the co-moving frame. When radiation is emitted from a source moving at a relativistic velocity straight against the observer, the flux is thus boosted with $2\mathcal{D}^3 = 2\Gamma^3$.

1.6.2 The curvature effect

The front of the jet moving out from the center of the star gets a curved surface since it expands spherically. The curvature effect occurs because the jet front has curvature and is not a plain surface. The situation at the jet front is showed in figure 1.12(a).

When two shells collide the merged shell is lit up due to the release of synchrotron photons from the electrons in the impact. Even though the whole shell is lit up at the same time, photons emitted at B in figure 1.12(a) reach the observer at a later time than photons emitted at A because of the longer way to travel. The photons at B also has a lower Γ in the line of sight than the ones emitted at A (because the jet expands spherically) and therefore they give a smaller contribution to the energy flux at the observer.

A pulse consists of photons emitted from all parts of the shell. If the jet front would be a plain surface, the photons emitted from all parts of the shell would reach the observer at the same time, and photons from every part of the shell would have the same boost in energy.

For a jet front that has curvature the situation is different. The situation when the shell is lit, with the jet seen straight from above is showed in figure 1.12(b). An observer first sees the photons from the center and when time passes photons from an annulus around the center that gets larger and larger. Since the photons closer to the center have a larger Γ in the direction of the observer, they make a larger contribution to the energy flux light curve at the observer. When the shell is lit it is therefore mainly radiation from the center that is seen. When time passes photons from larger annuli reach the observer, which therefore give a small contribution to the flux in the light curve.

When the shell stops glowing, at first it is only radiation from the center that doesn't reach the observer. The observer still sees the radiation from the outer annuli (see figure 1.12(c)).

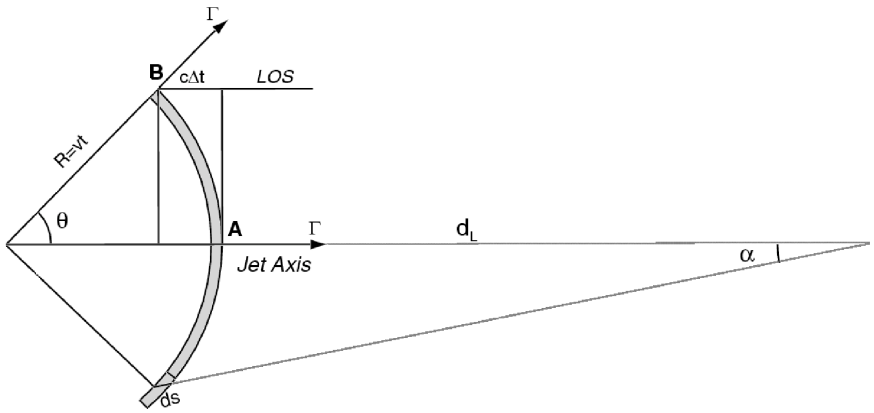

(a) Due to the geometry of the jet front the pulse decay phase in the observers frame is modified. This effect is called the curvature effect. It arises since the photons emitted from different regions of the jet front reach the observer at different times, and have different Γ factors. (Figure from Ryde & Petrosian (2002).)

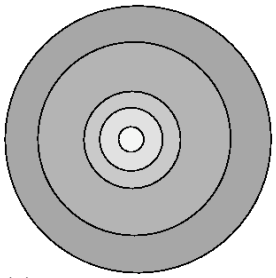

(b) The observer first sees radiation from the center of the jet. As time passes photons from annuli of larger and larger radii are seen.

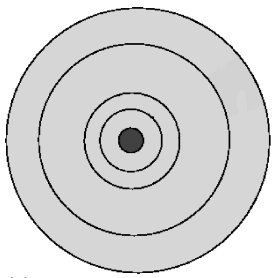

(c) When the shell stops glowing at first only the photons from the center does not reach the observer. The photons from the rest of the jet are still visible.

Figure 1.12: The geometry at the jet front.

The energy flux light curves for the co-moving frame and the observers frame are showed in figure 1.13. The left figure shows the real pulse, as it is emitted in

the co-moving frame, while the right figure shows the situation as it is observed, affected by the curvature effect.

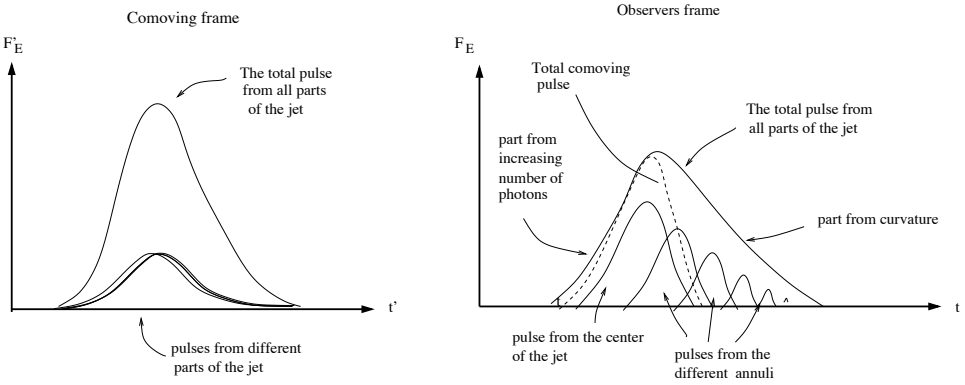

Figure 1.13: The appearance of the pulse in the co-moving and observers frame.

A pulse can be described as consisting of many δ pulses. Every δ pulse is affected by the curvature. This is called convolution. It describes the observed flux in the spectrum and light curve and is expressed as

$$F(E,t) = F_0 \int_t^{\infty} \frac{f(t-x)}{(1+\frac{x}{\tau_{\rm ang}})^2} \mathcal{B}_{\alpha,\beta}\left(\frac{E}{E_{\rm p}(t,x)}\right) dx, \tag{1.18}$$

where

$$E_{\rm p}(t,x) = E_{\rm p,0}\Big(1+\frac{x}{\tau_{\rm ang}}\Big)^{-1} (f(t-x))^{-\frac{1}{\eta_{\rm int}}}. \tag{1.19}$$

$F(E,t)$ in equation 1.18 describes the flux as a function of energy and time. F_0 is the flux at time $t = 0$. The first factor of the integral describes the co-moving light curve. f is the co-moving pulse function. It could be a δ function. x is the integration variable, and τ_{ang} is the angular time scale ($\tau_{ang} = \Delta t = R/2c\Gamma^2$, see below), where R is the radius of the jet curvature. The second factor of the integral describes the appearance of the spectrum. $\mathcal{B}$ is the Band function, which is often used to describe the spectra of bursts. α and β are the spectral indices on either side of the break in the spectrum. The energy of the break is E_p. Equation 1.19 describes the evolution of E_p. $E_{p,0}$ is the initial value and $\eta_{\rm int}$ is the relation index. When integrated over all energy, equation (1.18) reduces to equation (1.20).

$$F_{\rm bol}(t) = F_0 \int_t^{+\infty} \frac{f(t-x)}{(1+\frac{x}{\tau_{\rm ang}})^2} dx \tag{1.20}$$

The observed rise phase of the pulse approximately describes the rise phase of the real pulse in the co-moving frame, but the appearance of the decay phase is a result of the curvature of the jet front. Since the curvature can be different for different GRBs, and the effect therefore varies, it cannot be determined how much of the pulses decay phases that depends on the curvature effect.

Following the notations in figure 1.12(a) Δt is expressed as

$$\Delta t = \frac{R}{c}(1-\mu) \tag{1.21}$$

$$\Leftrightarrow \mu = 1 - \frac{c\Delta t}{R}. \tag{1.22}$$

For the angle $\theta = 1/\Gamma$ equation 1.21 is expressed as $\Delta t = R(1 - \cos(1/\Gamma))/c$. Taylor expansion of the cosine expression give that this is written as

$$\Delta t \approx \frac{R}{2c\Gamma^2}, \tag{1.23}$$

which is called the angular time scale, τ_{ang}. Inserting equation 1.22 into expression 1.14 yield the expression

$$\mathcal{D} = \frac{1}{\Gamma(1 - \beta - \frac{\beta c \Delta t}{R})}. \tag{1.24}$$

Taylor expansion of the expression for Γ ($\Gamma = (1-\beta^2)^{-1/2}$) yield that $\beta = 1-(2\Gamma)^{-1}$, which inserted into equation 1.24 yield the expression

$$\mathcal{D} \approx \frac{2\Gamma}{1 + \frac{\Delta t}{\tau_{ang}}} \tag{1.25}$$

for $\mathcal{D}$. When $\Delta t > \tau_{ang}$ then $\mathcal{D} \propto t^{-1}$.

1.6.3 Redshift

Due to the expansion of the universe observed wavelengths are longer than when emitted, observed times larger, and energies and fluxes smaller in the following ways ($'$ describes the coordinates in the co-moving system).

$$\lambda = \lambda' \cdot (1 + z) \tag{1.26}$$

$$t = t' \cdot (1 + z) \tag{1.27}$$

$$E = \frac{E'}{1 + z} \tag{1.28}$$

$$F \sim \frac{E}{t} = \frac{E'}{t' \cdot (1 + z)^2} \tag{1.29}$$

This effect is much smaller than the relativistic effect. It can nevertheless be of interest to see if properties of the GRBs change with redshift.

1.7 Aim of thesis

The aim of this thesis is to determine whether the X-ray flares detected in about half of all GRBs during the afterglow are related to the prompt emission in the long-lasting central engine activity model or if they are created due to refreshed shocks. The method is to analyze the pulse behavior of the prompt gamma-ray pulses from light curves obtained with *Swift*'s BAT and compare with the behavior of the X-ray flares from light curves observed with *Swift*'s XRT.

1.7.1 Outline

In chapter 2 the *Swift* satellite and its two instruments to detect gamma- and X-ray radiation are described. In chapter 3 the background to fitting light curve pulses with functions is discussed, the sample is presented and descriptions about the data reduction are made. In chapter 4 the results are presented, and in chapter 5 they are discussed. Finally the conclusions that are drawn are presented in chapter 6.

Chapter 2

Instruments and data

2.1 Detection of gamma- and X-rays

Gamma-rays are so energetic that they pass right through mirrors and cannot therefore be reflected onto a detector. To detect gamma-ray photons a coded mask is therefore used, which while being illuminated by γ-rays casts a shadow pattern on a detector to derive the position of the light source.

X-rays are also energetic and tend to pass through most materials (mirrors), but they can be focused using grazing incidence, which means that the X-rays hit a mirror with an angle almost parallel to the plane of the mirror. The X-rays are so reflected onto a detector. Thus the mirrors in an X-ray telescope has to be almost parallel to the telescope's line of sight. To cover as much area as possible several mirrors are placed inside another.

Since GRBs emit γ-rays in their prompt emission and X-ray to optical radiation in their afterglows, instruments that are able to detect radiation in all energy bands are necessary to cover the entire gamma-ray burst process. To gain as much information as possible it is important that the observations start very soon after the burst trigger. This is done with the *Swift* satellite.

2.2 The *Swift* satellite

The *Swift* satellite was launched in November 2004 and is a multi wavelength telescope with three instruments to detect GRBs and their afterglows; the BAT (Burst alert telescope) which detects the prompt emission of gamma-rays, the XRT (X-ray telescope) which detects X-rays and the UVOT (UV-optical telescope) for detection of UV and optical light. See drawings of the spacecraft in figure 2.1. The *Swift* satellite (Gehrels et al., 2004) performs autonomous rapid slews and observes about 100 bursts per year with detailed X-ray and UV-optical afterglow detections from about one minute to several days after the burst. The short time from detection to observation of the afterglow is what makes *Swift* special compared with the previous GRB telescopes. *Swift* will study about 1000 bursts, with $0.3 - 2.5$ arc sec positions, over a period of about three years. The goals of the mission are mainly to

- determine the origin of GRBs
- classify GRBs and search for new types
- study the interaction of the blast wave with the interstellar medium
- use GRBs to study the early universe

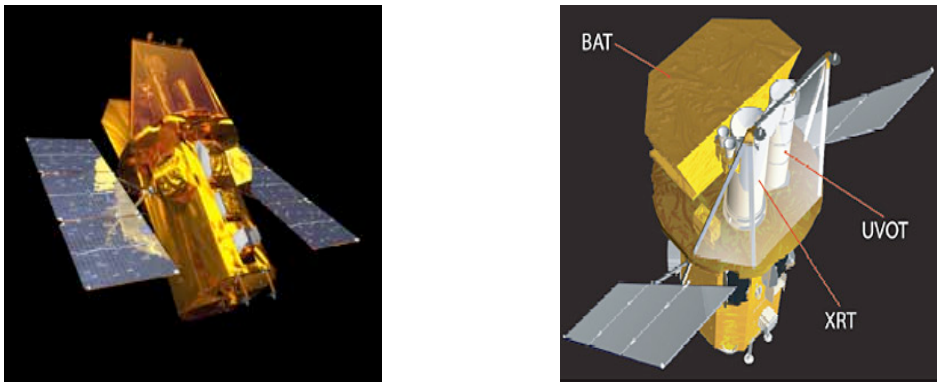

Figure 2.1: The *Swift* satellite. The picture on the right illustrates the three instruments working on *Swift*. From *Swift* web site.

The BAT (Barthelmy et al., 2005) is a wide field of view gamma-ray detector that search the sky for GRBs. The XRT (Burrows et al., 2005) and the UVOT are narrow field of view instruments which are aligned with the BAT. The main purpose of BAT is to detect bursts and calculate their position (which it does with an accuracy of about 4'), and as quickly as possible distribute the information so that the telescope can perform a slew to point the two narrow-field instruments XRT and UVOT at the burst location for observations in all three wavebands simultaneously. The XRT refines the position to within 5" and perform spectroscopy in the energy band 0.2-20 keV. The UVOT refines the position even further to 0.3" and makes optical finding charts. The precise positions will make it possible to identify the host galaxy.

The slew is finished and the broad band observations will take place within 20-70 s after a burst detection, much sooner than the previous satellites, which makes *Swift* observe the emission orders of magnitude brighter than the previous satellites did. Determinations of redshift are made by *Swift* for all bursts possible. If iron emission lines are detected redshift will be measured with an accuracy of about 10%. Additionally emission and absorption behavior can reveal information of the environment surrounding the GRB. The observations are sent to the ground control with the TDRSS link and the data (FITS files are created from both BAT and XRT) is then put on the HEASARC archive home page from where it can be downloaded. ASCII files of the XRT data can also be found at the *Swift* XRT light curve repository at `http://www.swift.ac.uk/xrt_curves/`.

When a photon hits the detector plane it is registered as an event with time, detector number and energy. One can imagine the data in a three dimensional data matrix with time, energy and flux on the three axes. Figure 2.2 shows an example of a data matrix from GRB 960330, from a simulation of the hybrid model of the GRB spectra (from M. Battelino's masters thesis). The light curve of a GRB for a specific photon energy is obtained from the intersection between the data matrix and a plane parallel to the time and flux axes for the certain energy. Similarly a spectrum at a certain time is obtained from the intersection between the data matrix and a plane parallel to the energy and flux axes, for the time in question. The bolometric light curve, which contains photons of all energies, is obtained by integrating the flux over all energies, and similarly the total spectrum for the entire burst, which contains photons observed at all times, is obtained by integrating the flux over all times.

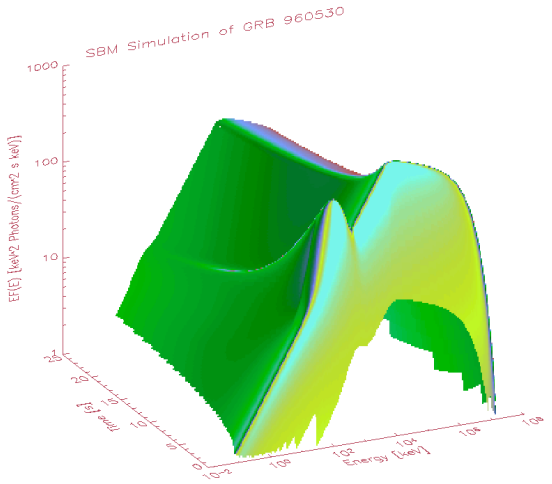

Figure 2.2: Simulated GRB spectrum using a hybrid model of a power law and a black body, presented in a data matrix. (From M. Battelino's masters thesis at Stockholm observatory.)

2.2.1 BAT – Burst alert telescope (15-150(350) keV)

The BAT detector (Burst alert telescope) is a wide field of view imaging hard X-ray telescope which detects photons in the energy range 15-350 keV. The telescope works best up to energies of 150 keV, so to make spectral analyzes 150 keV is the upper energy limit, but the telescope is able to detect photons up to 350 keV. The BAT consists of essentially two parts – a (two dimensional) coded aperture mask and a detector plane. The coded aperture mask is placed one meter above the detector plane, which is about 3 m^2. The coded aperture mask consists of about 54 000 lead plates in a random pattern with 50% open and 50% closed that block the light. Gamma-rays that hit the mask create a shadow pattern on the detector. From the shadow pattern the position of the gamma-ray source can be found.

The BAT has a 1.4 steradians field of view and a large energy range in order to study bursts from a large part of the sky with varying intensities. Since GRBs vary in milliseconds, the BAT has an accuracy of $\sim$ 200 microseconds. A shield, placed both under the detector and around the mask, protects from background noise. The BAT has a $\sim$ 7 keV resolution and a sensitivity of $\sim 10^{-8}$ erg cm^{-2} s^{-1}. The BAT is about five times more sensitive than BATSE and has a shorter time from detection to observation.

The BAT works in both a survey mode that accumulate hard X-ray data, and a burst mode that produces burst positions. While searching for bursts the BAT works in the survey mode and collects count data every five minute for 80 energy intervals. The survey mode is pre-programmed. When a burst occurs the BAT switches to photon counting mode where every photon that hits the detector plane is registered as an event, with time, detector number and energy. To detect a burst the BAT looks for excesses in the count rate of gamma-ray photons above the background and constant sources with a "figure of merit" algorithm. The burst trigger threshold is about 8 sigma above background noise, a value that can be changed. If the BAT detects a burst the figure of merit algorithm decides whether a slew is worth requesting, that is if the burst has more "merit" than the pre-planned observations.

The BAT's field of view include the fields of views of the XRT and the UVOT, which enables emission from the burst to be studied simultaneously with X-ray and

UV-optical emission from the afterglow.

When a burst is detected by BAT its position is immediately sent to the ground with the TDRSS link and distributed through the GCN (Gamma-ray burst coordinate network) to the astronomical community. Positions of bursts detected by other telescopes can also be uploaded to BAT. These events are treated exactly the same as events discovered by BAT itself.

No background subtraction is needed for the BAT data because mask weighting is the same as background subtraction. When performing mask weighting detectors which are fully illuminated are assigned a weight of -1, and those not illuminated at all are assigned a weight of $+1$. The detectors partly illuminated get a weight in between $+1$ and -1. The detectors which are just a little illuminated are used to compute the background. The photons detected at all these detectors, that are just a little illuminated, are added, and and a average value per detector is computed. This average value is then subtracted from all detectors, and left is only the source photons.

2.2.2 XRT – X-ray telescope (0.2-10 keV)

The XRT is a focusing X-ray telescope, with a field of view of 23.6×23.6 arc min, in the energy range 0.2-10 keV. It is a grazing incidence telescope which focuses X-rays onto a CCD-detector with 600×602 pixels (each pixel size is $40\mu\text{m} \times 40\mu\text{m}$), and an area of 110 cm^2. The detector work in -100 °C to minimize dark current. The energy resolution changes from 190 eV at 10 keV to 50 eV at 0.1 keV. Since the afterglow flux decreases the XRT can measure fluxes which covers more than 7 orders of magnitude. The XRT autonomously changes the readout mode as the flux changes. The readout modes are:

- The image mode (45 Crab[1]<flux< 25 mCrab) is only used to position bright sources. It measures the total energy deposited per pixel and does not register each photon. The exposure time can be changed from the ground.
- The photo diode mode (60 Crab <flux< 0.6 Crab) produces light curves with a time resolution of 0.14 ms. It has been disabled due to a micrometeorite hit.
- The timing mode (flux 600-1 mCrab) has a high CCD readout and achieve high time resolution but has a low position information. It also performs spectroscopy.
- The photon counting mode (flux $<$ 1 mCrab) obtains full spatial and spectral information, but has a low time resolution.

The CCD is surrounded by a shied which protects against cosmic rays and a filter is placed in front of it to block optical light. When an incoming X-ray photon hits the CCD, the CCD registers its time and energy.

Within 10 seconds the XRT has determined the position of the GRB to 5" accuracy. After 20-70 seconds after the burst up to days or weeks it can study the X-ray emission. XRT will in many cases begin to observe before the prompt emission has ended.

First the XRT determines the position of the source by taking a picture with the image mode. Within 5 seconds the position is determined to better than 2.5 arc sec. As the flux changes the XRT switches automatically to the timing mode and photon counting mode to measure the light curve and spectrum of the burst. For all modes the data is saved in event list files. The files are FITS files.

[1]A Crab is sometimes used as a flux density unit in the energy band 2-10 keV. One Crab corresponds to a flux density of about $2.4 \cdot 10^{-8}$ erg cm^{-2} s^{-1}.

2.3 FITS files

A FITS file (FITS = flexible image transport system) is a file format which is often used by the astronomical community for convenient data exchange between different places whose standards differ. A FITS file consists of several headers which describe how the data is organized. It can also provide information of, for example, instrument status. To manipulate the FITS data tools called FTOOLs are used.

Chapter 3

Method

3.1 Background

Information about the temporal behavior of GRB pulses is important since it might provide clues about the physics of the inner engine. Since GRBs are proposed to result from an ejection of numerous shells with various Lorentz factors that create light pulses in collisions between them, the GRB light curve can reproduce the activity of its inner engine.

In general light curves are very complex which makes them hard to analyze, but some consist of pulses with a very smooth shape, with a fast rise and exponential decay (FRED pulses)[2]. Since some GRBs consist of only one FRED pulse, the FRED pulse is expected to display the fundamental physics of the GRBs corresponding to a collision. The form of the FRED could in part be an effect of the curvature effect. The complex GRBs are thought to be superpositions of several FRED pulses and are often too complicated to analyze. Analyzes are instead made on smooth single pulses. Several functions have been developed in order to describe these pulses (see for example Kocevski et al. (2003), Norris et al. (1996) and Chincarini et al. (2007b)). The fitting of the pulses with a function reveals statistical properties of the GRBs. Since the light curves of the GRBs look so different, examining the pulse shapes in them is a good way to look for similarities amongst them. The variation of pulse model parameters can provide a clue to the process creating the bursts.

Fundamental parameters concerning the pulse shapes are the full-width half maximum ($FWHM$), the full width at 75% of maximum ($FW75\%$), the amplitude or maximum flux (f_{max}), the rise- and decay time (t_r and t_d), the asymmetry a (the fraction of the rise time and the decay time) and the rise and decay power law indices (r and d). Another important measure is the spectral lag, which is the time displacement of the flux peak in different energy intervals.

3.2 The analytical pulse function

To analyze time profiles of FRED pulses Kocevski et al. (2003) present an analytic function of the flux as a function of time, $F(t)$, described by four parameters – F_m, t_m, r and d, where F_m is the maximum flux (at $t = t_{peak}$), t_m is the time at the maximum flux, r is the rise power law index and d the decay power law index. The derivation of the function is based on the two empirical relations of the bursts spectra described in section 1.4.1, the hardness intensity correlation (HIC) and the hardness-fluence correlation (HFC). The HIC, which relates the hardness

[2]Not necessarily exponential decay but rather power law.

of the spectra at a certain time and the energy flux at the same time is expressed as

$$F_E = F_0 \left(\frac{E_{pk}}{E_{pk,0}} \right)^{\eta} \tag{3.1}$$

and the HFC, which relates the peak energy and the time-integrated photon flux is expressed as

$$E_{pk}(t) = E_{pk,0} e^{-\frac{\phi(t)}{\phi_0}}. \tag{3.2}$$

(See section 1.4.1 for explanations of the involved variables.) By combining these expressions a differential equation is obtained:

$$E = -\frac{F_0}{\phi_0 E_0^{\eta}} E^{\eta} \tag{3.3}$$

As shown by Kocevski et al. (2003) this leads to that the flux can be expressed as

$$F(t) = F_m \left(\frac{t}{t_m} \right)^r \left(\frac{d}{d+r} + \frac{r}{d+r} \left(\frac{t}{t_m} \right)^{r+1} \right)^{-\frac{r+d}{r+1}}. \tag{3.4}$$

The function can so describe single pulses in GRBs with the four parameters r, d, F_m and t_m, by observing the light curve of the GRB. The variable t is the time since the trigger, assuming that the pulse starts at the trigger. For the function to describe pulses that start at later times, t in the function must be replaces with $t - t_0$, where t_0 is the real start time of the pulse. The variable $-t_0$ is sometimes referred to as c.

To examine the behavior of the function for small and large times, where the pulse starts and ends, the values of the function when $t \to 0$ and $t \to \infty$ are computed. When $t \to 0$, $F(t) \to t^r$ (see Kocevski et al. (2003)) and when $t \to \infty$, $F(t) \to t^r \cdot (t^{r+1})^{-\frac{r+d}{r+1}} = t^r \cdot t^{-r-d} = t^{-d}$. The function so behaves as a power law with $F(t) \to t^r$ when $t \to 0$, and $F(t) \to t^{-d}$ when $t \to \infty$. Figure 3.1 shows the analytical pulse function (equation 3.4) for $t_0 = -10$ s, $r = 3$, $d = 5$, $t_{max} = 20$ s and $f_{max} = 1.5$ Counts/s, displayed together with the pulse parameters. To see

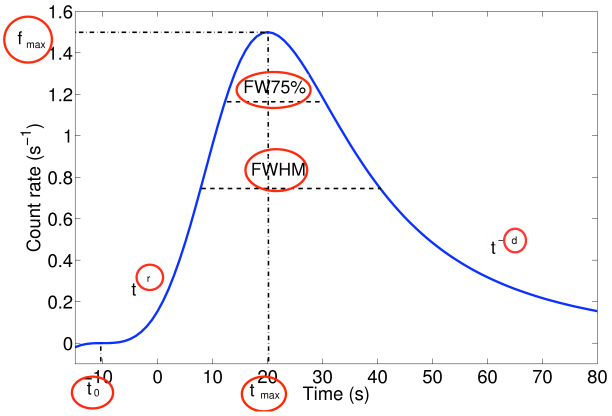

Figure 3.1: The analytical pulse function with $t_0 = -10$ s, the rise power law index $r = 3$, decay power law index $d = 5$, $t_{max} = 20$ s, $f_{max} = 1.5$ counts/s. As $t \to 0$ $F(t) \to t^3$, and as $t \to \infty$ $F(t) \to t^{-5}$.

how much of the pulse which really has a power law behavior, the power law for the rise and decay phases are plotted with the function in figure 3.2. As can be seen the function only has a power law behavior for small or large values of t.

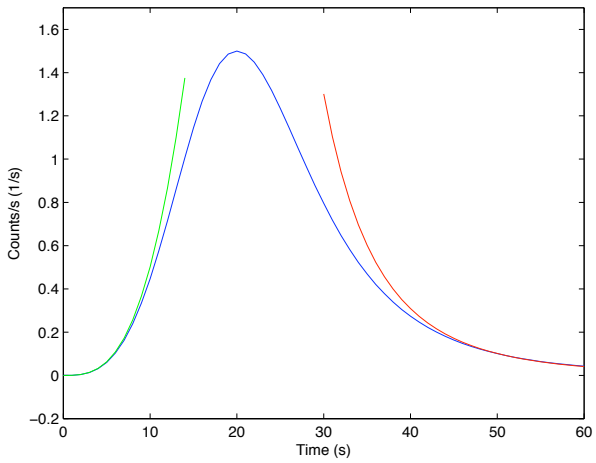

Figure 3.2: The analytic pulse function with the power laws $N(t) = t^r$ and $N(t) = t^{-d}$. The power laws only agree with the pulse function for large or small values of t.

3.2.1 The sensitivity of the pulse function

To get a feeling for how the pulse varies with the different parameters the function is plotted with different values of r, d and c. Three different cases are displayed in figure 3.3. Figure 3.3(a) shows the analytical function with three different values of the rise parameter r; 1, 3 and 5. In these cases $d = 3$ and $c = 10$. Figure 3.3(b) displays the function's behavior when the decay parameter, d, is varied between 1, 3 and 5, while $r = 3$ and $c = 10$. Finally, figure 3.3(c) displays the situation when the t_0-parameter is varied between -5, 10 and 25 (while $r = d = 3$.).

3.3 Pulse analysis program

The aim is to characterize pulse shapes in different energy bands (data from BAT and XRT) and to do that an IDL program called `rice.pro` (Kocevski et al., 2003) is used. `rice.pro` fits the pulses with function 3.4 and utilizes the Marquardt-Levenberg nonlinear fit method which adjust values of the parameters in the pulse function and minimize the difference between the function and the pulse with a least χ^2-fit. Parameters (r, d, t_{max}, f_{max}, $FWHM$ and $FW75\%$) from the shape of the function that corresponds to the best fit are obtained directly from the fit. `rice.pro` is made to fit the function to pulses in the light curves of BATSE data, so the program has to be modified in order to fit *Swift* light curves, and is thereafter named `srice2.pro`. It can be found in appendix B.

To be able to read the BAT light curves (which are FITS files) the modifications include adding an option in the program to first be able to select the BAT files when pressing `file` and `load`, and a `channel` button to be able to select an energy channel. To open and read the FITS file `srice2.pro` is extended with `XVOIGT_BAT` which the program goes to when BAT is chosen. The commands used in `XVOIGT_BAT` include `dialog_pickfile` which opens a window to make it possible to select the light curve file that should be opened by the program, and `mrdfits`, which opens the selected FITS file and read information from the FITS file's headers and saves it in the variables `data1` and `data2`. The times from the FITS file are then collected with `data1.time` and saved as a column vector as the variable `atimes`, and the

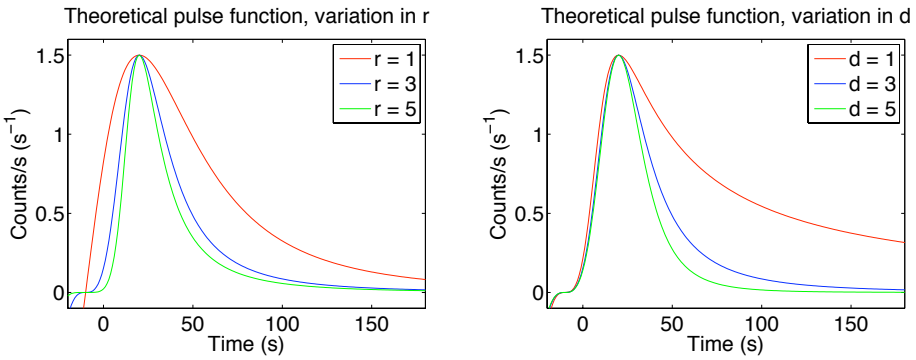

(a) r is varied.

(b) d is varied.

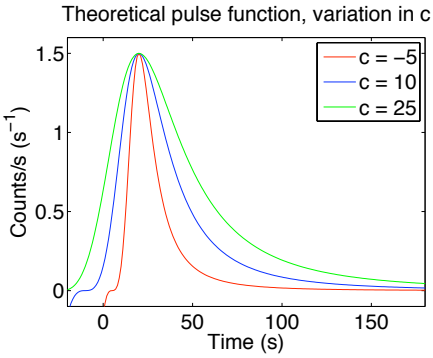

(c) c is varied.

Figure 3.3: For all cases $t_{max} = 20$ s and $f_{max} = 1.5$ counts/s. These are not varied since they only change the position and height scale of the situation. The values of the parameters c, r and d are altered in the different cases.

rate is read by `data1.rate` and saved as a matrix with column vectors defining the rate of each of the four energy channels selected in BAT (see section 3.4.1) in the variable name `arate`. The command `size` computes the number of data points the time vector `atimes` consists of and saves it in `aantal`, and a matrix with two identical columns is then created, because it is needed later in the program.

When the `BAT` option is selected the light curve from the chosen file is plotted on the screen by the use of `if axis eq 'BAT' then begin` command. To plot the light curve in energy channel 1 and 3, when a channel is chosen, the program is extended with `XVOIGT_CHAN1` and `XVOIGT_CHAN3`. In `XVOIGT_CHAN1` the commands `plottext=1.0` and `plotwhat=1` are used. `plotwhat=1` picks out the selected energy channel from the rate matrix (and names it 'counts'). It is then plotted on the screen in the same way as for the total light curve.

To be able to read the XRT light curves (ASCII files) an option `XVOIGT_XRT` is added to be able to select the light curve file. After pressing `Load` and `XRT` the program contacts `XVOIGT_XRT` to open a light curve data file. In `XVOIGT_XRT` the extension `*xrt` is added in the `dialog_pickfile` command to match the extension of the ASCII files. The command `openr` opens the data file. The line `inputdata=fltarr(2,slask)` is added to define the format of the ASCII data file. It is a matrix with two columns and with the number of elements in the columns written on top of the program. The `readf` command is added to read the file. The values of the times and 'counts' of the ASCII file are selected by the commands `times(0,*)=inputdata(0,*)` and `counts=inputdata(1,*)` respectively. The light

curve is plotted on the screen.

The changes also include adjusting the minimum and maximum values in the sliders for the different parameter, to fit the *Swift* data, and to print the fit parameters, and their errors, along with the χ^2 value of the fit directly in the terminal window.

3.3.1 How to use `srice2.pro`

When `srice2.pro` is opened a graphical window is shown on the computer screen. Figure 3.4 illustrates the window with the light curve of GRB 060912A. By pressing

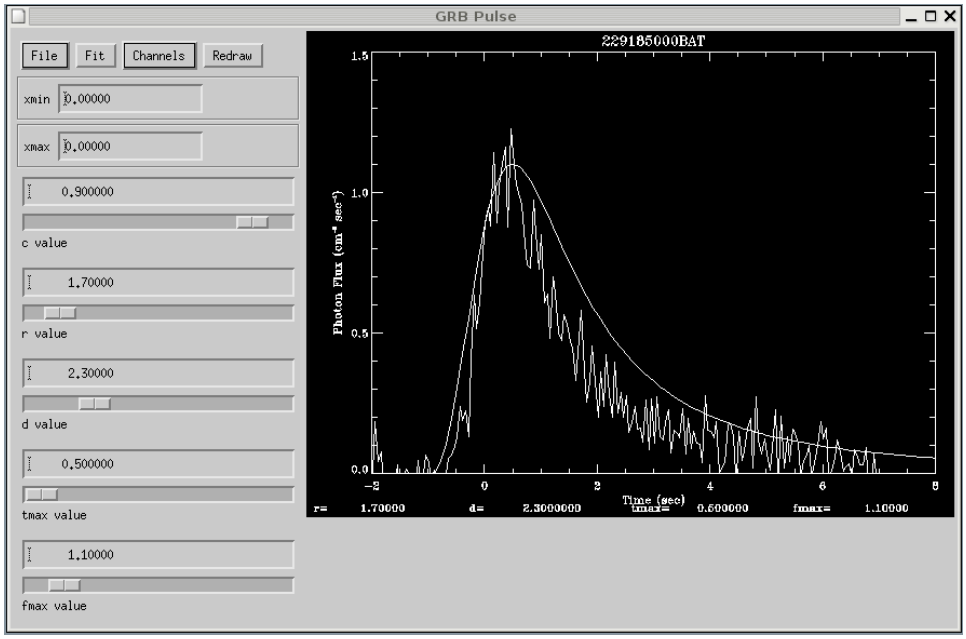

Figure 3.4: The IDL program `srice2.pro` as it is shown on the computer screen.

the `Load` and `BAT` buttons in `File` in the menu at the top left the light curve file can be selected and opened. When a file is selected the light curve together with the pulse function that is being fitted (equation 3.4) are shown in the window at the right of the figure. The shape of the function can be altered by using the slides in the left of the figure. The parameters that can be altered are c, r, d, t_{max} and f_{max}. The c parameter ($c = -t_0$) is excluded from the fitting to obtain higher certainties in the other parameters, but its value is set to the onset of the pulse, which is found manually. To obtain parameters from a fit the slides must be changed so that the appearance of the theoretical function is similar to the observed pulse. The initial values of the pulse function must be relatively close to the actual pulse shape to get the Marquardt-Levenberg method to converge and find the correct minimum in the χ^2-space, and thereby the fit parameters. When changing the slides the pulse function's shape changes and when they look similar the `Fit` button can be pressed to obtain the least square fit parameters. These are printed directly in the terminal window and can be put into a text file.

To fit the pulses in energy channel 1 and 3 the above procedure is repeated, after pressing the `Channel` button where the channel of interest can be chosen. For the light curve in the example the pulse is visible in energy channels 1 and 3, and the situation is displayed in figure 3.5. In this case the shape of the total pulse and the shapes of the pulses in each energy channel don't differ noticeably.

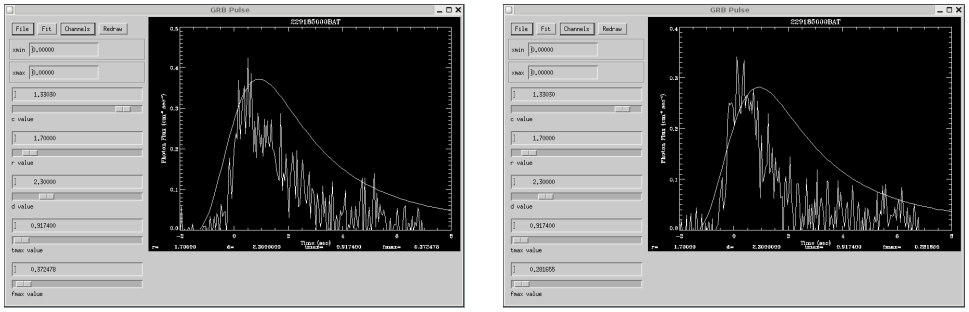

(a) channel 1 (b) channel 3

Figure 3.5: `srice2.pro` for channel 1 and 3.

3.4 The GRB sample

Since short and long bursts are thought to originate from different kinds of processes, and the temporal behavior of short and long bursts are different, only the long bursts are studied here. The aim is to characterize shapes of single, long gamma-ray pulses in the prompt emission and X-ray flares in the afterglow. To be able to fit the pulses in the pulse fit program the pulses need to be well separated and be clearly visible above the background. Two different samples for the prompt pulses and X-ray flares are obtained.

3.4.1 The BAT sample

Data for the BAT prompt emission is available at the *Swift* archive on `http://heasarc.gsfc.nasa.gov/cgi-bin/W3Browse/swift.pl`. On the web site `http://swift.gsfc.nasa.gov/docs/swift/archive/grb_table/` it is possible to view a table over the detected GRBs and some of their properties, e.g. the T_{90} duration, the fluence in the 15-150 keV energy range, the 1-sec peak photon flux in the 15-150 keV energy range and the redshift (if computed). Figures of the light curves are also available. To get clearly visible strong pulses a criteria is that the BAT 1-sec peak photon flux > 2 ph cm^{-2} s^{-1}. Data is downloaded between the period 050124 to 061222. This results in a total of 67 burst (only long bursts are included). The light curves of these 67 burst are examined, and they are classified with either A, B or C, depending on the appearance of the pulse. The pulses classified with A are strong and have a smooth shape. The ones classified with B are pulses that have semi good appearances, and the ones classified with C has a far too complicated light curve, with no clear pulses that can be used in the pulse fit program. Only the A sample is used since nice shapes of the pulses are needed in the pulse fit program. That makes a sample of 23 bursts (and 27 pulses – some bursts have more than one pulse). The sample is displayed in table 3.1 and figure 3.6.

When making a BAT light curve the energy interval (15-350 keV) is divided into smaller energy intervals, or channels. These are: channel 1 (15-25 keV), channel 2 (25-50 keV), channel 3 (50-100 keV) and channel 4 (100-350 keV). The total light curve is obtained by adding the counts in all energy channels.

Also displayed in table 3.1 are which bursts that have redshifts (sample 'BAT redshift') and X-ray flares (sample 'BAT X-ray flares') in their afterglows. These sub-samples should be used to examine redshift affection, and examine the properties of the X-ray flares, and to see if there is any correlation between the numbers of pulses in the BAT prompt emission and the XRT afterglow flares. However, the BAT X-ray flares sample is not used as the flare sample. The flares need to be

strong and have a smooth shape. A different sample is instead used (see section 3.4.2). To obtain pulses that can be used in the pulse fit program the data has to be reduced.

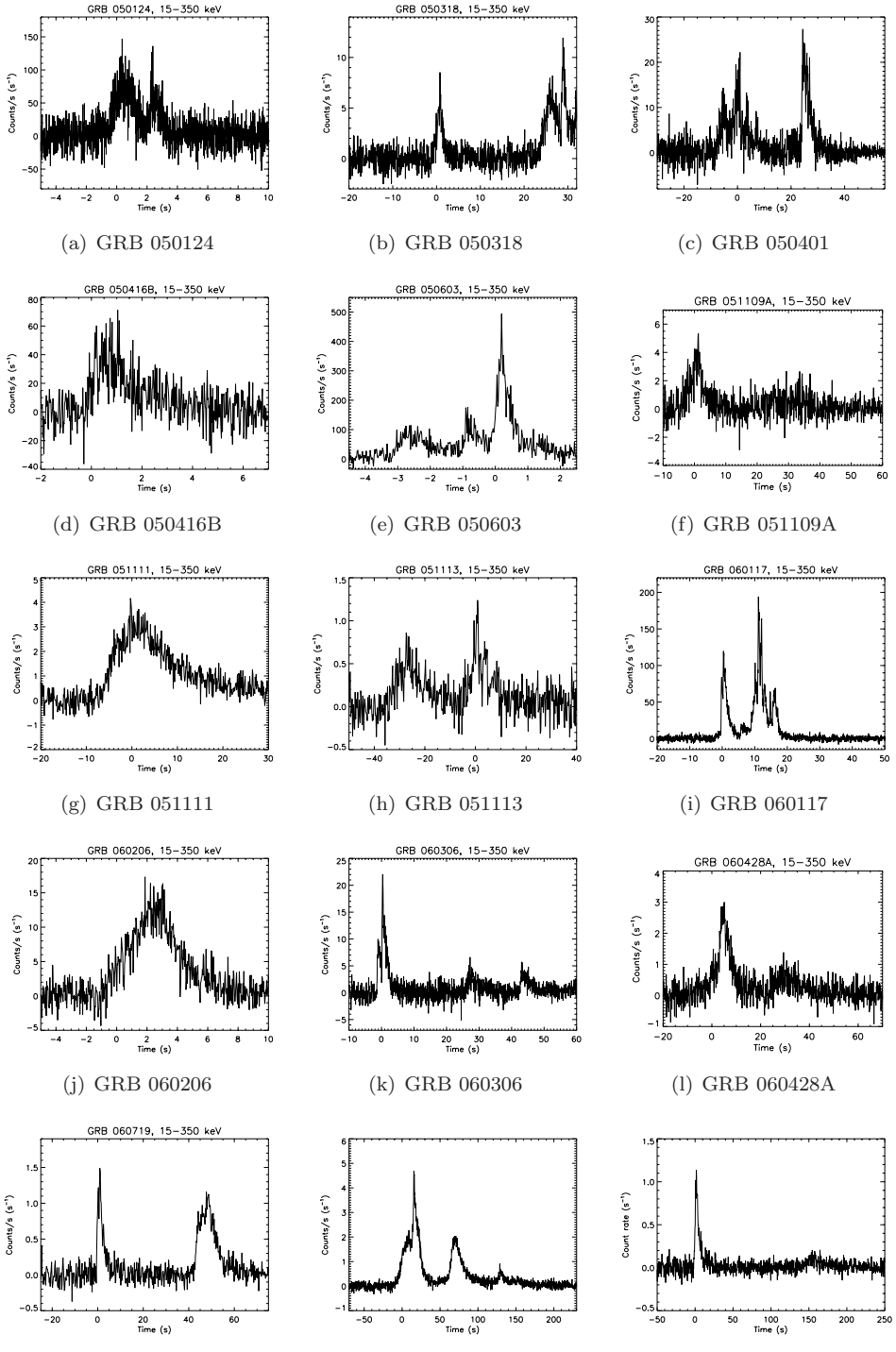

(a) GRB 050124 (b) GRB 050318 (c) GRB 050401

(d) GRB 050416B (e) GRB 050603 (f) GRB 051109A

(g) GRB 051111 (h) GRB 051113 (i) GRB 060117

(j) GRB 060206 (k) GRB 060306 (l) GRB 060428A

(m) GRB 060719 (n) GRB 060814 (o) GRB 060904B

Figure 3.6: The BAT sample light curves.

GRB	Trigger number	Pulse	Good pulse (marked with *)	z	X-ray flares
050124	103647	1		-	NFD, however SD and DG
		2			
050318	111529			1.44	NFD, however SD and DG
050401	113120			2.9	NOF the first 3000 s, after that SD and DG
050416B	141797			-	NFD, however SD
050603	131560	1		2.821	NFD, however SD
		2			
		3	*		
051109A	163136			2.346	Possible weak flare at 150 s
051111	163438		*	1.549	No prominent flare but large DG
051113	163765			-	XRT data is unavailable
060117	177666			-	XRT data is unavailable
060206	180455		*	4.05	Possible flare at 4000 s, however SD and DG
060306	200638			-	NFD the first 1000 s, however SD and DG
060428A	207364		*	-	Possible weak flare at 700 s, however SD and DG
060719	220020			-	Observed flare at 1100 s
060814	224552	1	*	0.84	Observed flare at 150 s
		2	*		
060904B	228006			0.703	Very strong flare observed at 200 s
060908	228581		*	2.43	Observed flare at 100 s
060912A	229185		*	0.937	Possible weak flare at 700 s, however SD and DG
060919	230115			-	NFD, however SD and DG
061019	234516			-	NFD, however SD and DG
061021	234905		*	-	NOF the first 500 s, after that SD and DG
061121	239899			1.314	Possible weak flare at 70 s
061126	240766			-	NFD, however SD and DG
061222A	252588		*	-	Possible weak flare at 150s
Total number:	23	27	10	11	Possibly 10 (of 23)

Table 3.1: The BAT sample of 23 A-classified GRBs with BAT 1-sec peak photon flux > 2 ph cm^{-2} s^{-1}, sorted after the time of observation. (GRB 050820B and GRB 050701 are excluded from the sample because their trigger number isn't available, and GRB 060124 is excluded because there is a data gap in the middle of the data.) Some of the bursts have more than one good pulse. Columns 5 and 6 display sub-samples of the GRBs with redshifts (sample 'BAT redshift') and X-ray flares (sample 'BAT X-ray flares'). The star at some GRBs (in column 4) shows if the GRB has a good pulse, that is well fitted in the pulse fit program. NFD and NOF stands for no flare detected and no observed flare, respectively. SD stands for scarce data, while DG means data gap.

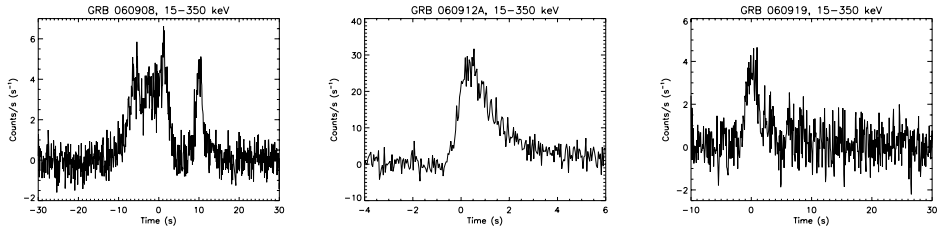

(p) GRB 060908 (q) GRB 060912A (r) GRB 060919

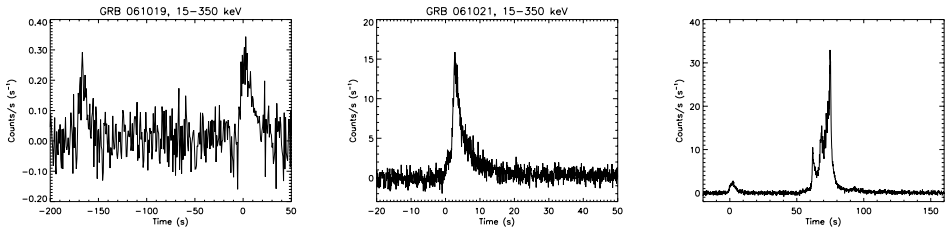

(s) GRB 061019 (t) GRB 061021 (u) GRB 061121

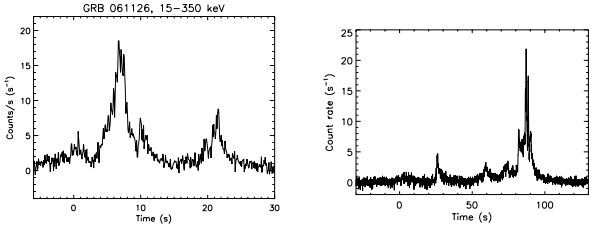

(v) GRB 061126 (w) GRB 061222A

Figure 3.6: (continued)

3.4.2 The XRT sample

To examine the shapes and behaviors of flares, GRBs which have strong flares, clearly visible above the background are needed. Also here the pulses should be nice, single pulses. The 'sample BAT X-ray flares' is not used as the flare sample because most of the flares aren't strong enough. However, XRT light curves can be viewed at the *Swift* XRT light curve repository at `http:// www.swift.ac.uk/xrt_curves/`, and from there GRBs with strong flares are chosen, by eye. They are the ones which contain flares with the largest $\Delta F/F$, where F is the flux of the afterglow and ΔF is the flux of the flare. 15 GRBs are chosen with a total of 27 flares. This sample is used as the X-ray flare sample.

To compare the number of emission episodes in the XRT data with the number of emission episodes in in the prompt emission, corresponding BAT light curves of the X-ray flare sample can be viewed at the *Swift* archive. The XRT light curves and their corresponding BAT light curves are displayed in figure C.1 in appendix C. The sample is displayed in table 3.2, along with the number of emission episodes in the BAT prompt emission and the emission episodes in the XRT afterglow.

To obtain pulses that can be used in the pulse fit program the background of the light curves has to be removed.

GRB	Trigger number	Number of BAT emission episodes	Number of XRT emission episodes
050502B	116116	2	2
050730	148225	3	5
050822	151486	2	3
050922B	156434	3	2
051117A	164268	1	4
060111A	176818	1	3
060204B	180241	1	2
060210	180977	3	3
060418	205851	1	1
060604	213486	2	1
060607A	213823	2	2
060714	219101	2	2
060904A	227996	1	2
060929	231702	1	1
061202	241963	1	1
Total number:	15	26	34

Table 3.2: The XRT sample. GRBs with X-ray flares and their corresponding number of emission episodes in the BAT prompt emission and in the XRT afterglow. GRB 060124 is excluded from the sample since it is too difficult to determine the slope of the underlying power law emission. It is difficult to determine the number of emission episodes in some GRBs since some light curves has such a complicated shape. Since the time it takes for XRT to slew at the target, the light curve starts a while after the trigger which makes that all the flares may not be detected.

3.5 Data reduction

When selecting a GRB on the *Swift* web site the data available for it is displayed, and files of interest can be selected and downloaded. For the BAT data (the prompt emission) only the first observation with the trigger number followed by 000 is of interest. The data available for downloading (for BAT) is the BAT data, auxiliary data, TDRSS data and Logs. The BAT data consists of, amongst others, event files (extension: .evt) and housekeeping files (extension: .hk). The event files contain data from when a burst is detected, and just before the burst occurs, and the hk files contain information from the file headers. The auxiliary data consists of orbit information and information about the spacecraft. The TDRSS data is messages sent to the ground as soon as the telescope observes a new burst, about for example the burst's position. Each instrument has its own messages. The Logs contain a summary of the available information and a list of files that have been created.

The TDRSS data, Logs, auxiliary data and BAT data are selected and downloaded. The data files are FITS files but saved as a tar-file when downloading. Data from the XRT is obtained from the *Swift* XRT light curve repository at `http://www.swift.ac.uk/xrt_curves/`. The data of interest is the basic photon counting data and basic windowed timing data, and it is in ASCII format (American Standard Code for Information Interchange). The data includes the times and background subtracted count rates.

3.5.1 BAT data reduction

To reduce the BAT data scripts based on the reduction threads available on the *Swift* web site, but altered here for our purposes (see appendix A) are used. The script `batlc.sh` (see appendix A) is used to extract a light curve (file name with extension .lc, a FITS file) from the BAT data (event files). The light curves are created using mask weighting (which is the same as background subtraction, see section 2.2.1) to ensure that the photons collected only come from the source of interest. `batlc.sh` uses the command `batbinevt` which uses an event file from the data and assemble the count rates for a specific energy interval in the time bins. The out file of `batbinevt` is a light curve. In `batbinevt` values of parameters like time bin and energy intervals can be changed.

If a quality map (contains information about good and bad pixels) needed in `batlc.sh` is missing from the downloaded data a script called `BAT_QMap.sh` (see appendix A) is run to create the missing file. After that `batlc.sh` is run again to retrieve the light curve. `BAT_QMap.sh` uses the command `batbinevt` to create a detector plane image (DPI) of the event data. A DPI is a histogram over the number of counts in two dimensions. Then, by using the time of the observation, a file called the enable/disable map is selected and downloaded from the web site `ftp://heasarc.gsfc.nasa.gov/swift/data/trend/`. A enable/disable map contains information about pixels that were bad during earlier observations. The DPI is then searched for noisy pixels with the command `bathotpix`. The pixels that are too cold or too hot relative to the center value are discarded. The outfile of `BAT_QMap.sh` is a quality map.

After the script `batlc.sh` has been run a light curve has been created, but the time in the light curve is counted from where the satellite begun observing, in 2004, not from where the trigger actually starts. To set the trigger time to zero when the burst starts, a script called `time-corr.sh`, that I have written (see appendix A), is used. The program uses the command `fcalc` which subtracts the trigger time from all elements in the time vector in the light curve file, and thus creates a time corrected light curve. With the script `short.sh` (see appendix A) only the pulse and its close surroundings are chosen from the created light curve. The command

used in `short.sh` is `fcopy` which allows the time interval of interest to be selected by applying a criteria for the time vector in the light curve file, and copies the part of the file with the chosen times, and the associated count rates into another file.

The flux unit from BAT is "counts per fully illuminated detector". This means that consideration is taken for where in the field the source is. If the source is near the edge of the field only few photons would be detected, and it would seem as the burst is weak. To consider the detectors which are fully illuminated is the same thing as moving the source to the middle of the field of view. In the reduction the size of the time bins are set. By dividing the count rates with the times of the bins the unit of counts/s is obtained.

After these scripts have been run the light curve file is ready to be used in the curve fitting program `srice2.pro`.

3.5.2 XRT data reduction

Data for the XRT light curves are obtained directly from the web, from the site `http://www.swift.ac.uk/xrt_curves/`. For details on how the data is produced, see Evans et al. (2007). The data includes the times and background subtracted count rates and is downloaded in ASCII format.

The XRT sample (seen in figure 3.7) consist of X-ray light curves with flares super positioned. To obtain flares from the XRT light curves (to fit in `srice2.pro`) the background has to be removed. The background is assumed to consist of one or more power law segment(s), see section 1.4.2. To remove the background a straight line is fitted to points before and after the flare (in some cases only one point before and one after, depending on the appearance of the background). The values of the count rates underlying the power law segments are then removed from the light curve, and left is the background subtracted flares.

As an example the light curve of GRB 050502B is shown in figure 3.8(a). The light curve has a flare super positioned on the background emission at about 500 s. To remove the background a straight line is fitted to points before and after the flare, see figure 3.8(b). This fitted function is then subtracted from the light curve, and the result is a pulse without background, see figure 3.8(c). Notice the change in the shape of the pulse from figure 3.8(b) and (c)).

The procedure is repeated for all flares in the sample, but with different numbers of points used in the fit to a straight line, depending on the appearance of the light curve. The light curve of GRB 050730 has at least two flares super positioned on the background (see figure 3.9(a)). In this case it seems like one flare lies on a slope and the other on a constant background. Therefore the background subtraction is different for the different parts of the light curve, as the lines in figure 3.9(b) indicate. The obtained pulsea are showed in figure 3.9(c). The XRT light curves, in zoomed flares with the straight lines fitted to the background, and background subtracted flares are displayed in figure D.1 in appendix D. It is important to remove the background correctly since it changes the shapes of the flares. When fitting a line to the background not just the in zoomed part of the light curve, but the total light curve should be looked at, so the background power law segments seem to fit in the larger scale also.

A total sample of 27 background subtracted flares have been obtained, see figure 3.10. These are now ready to be used in `srice2.pro`.

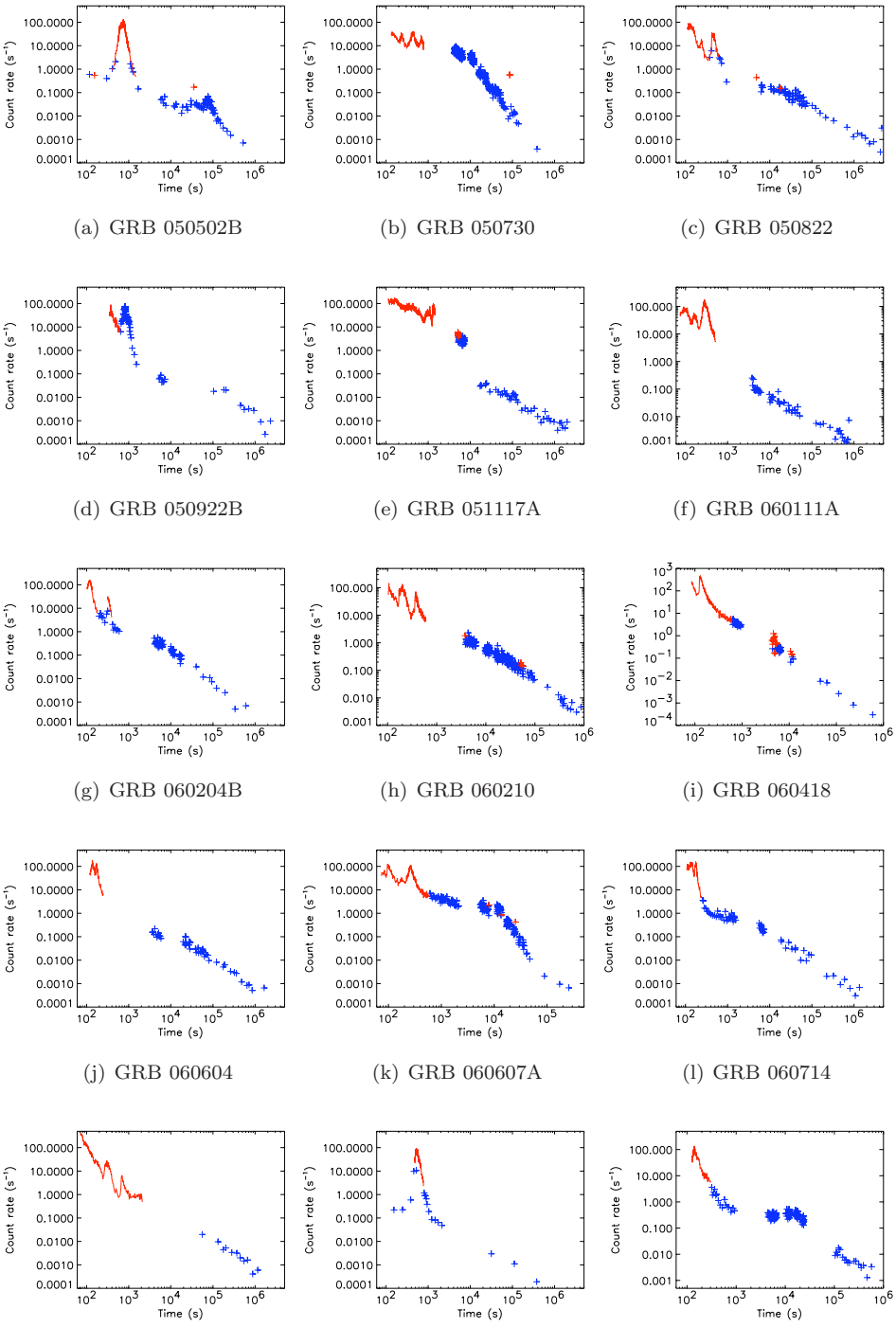

(a) GRB 050502B (b) GRB 050730 (c) GRB 050822

(d) GRB 050922B (e) GRB 051117A (f) GRB 060111A

(g) GRB 060204B (h) GRB 060210 (i) GRB 060418

(j) GRB 060604 (k) GRB 060607A (l) GRB 060714

(m) GRB 060904A (n) GRB 060929 (o) GRB 061202

Figure 3.7: The XRT sample light curves. The data from the different used modes of the XRT is displayed in different colors. Data from the windowed timing mode is displayed in red, while data from the photon counting mode is displayed in blue. The PC data is plotted with plus-signs because there is so little data, and lines between point would give a wrong impression about the light curve. Some of the WT data (that occurs after large data gaps) is also plotted as plus-signs for the same reason.

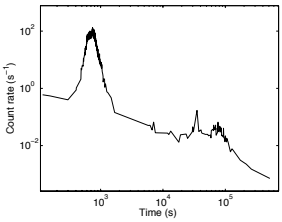

(a) The XRT light curve of GRB 050502B. The light curve contains a large flare which is super positioned on the declining afterglow emission.

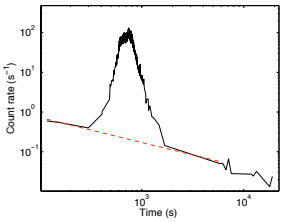

(b) The flare in the light curve in a closer look. The dashed red line corresponds to the assumed underlying background which is to be removed. This figure a bit modified can also be seen on the front page.

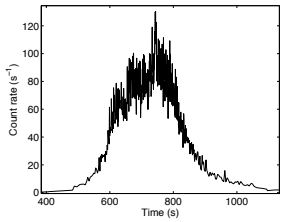

(c) The background subtracted flare.

Figure 3.8: The XRT light curve of GRB 050502B, the flare part of the light curve in zoomed, and the background subtracted X-ray flare.

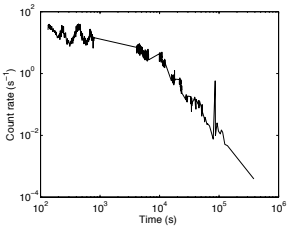

(a) The XRT light curve of GRB 050730 which includes some flares in the beginning.

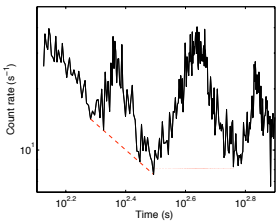

(b) The flares in the light curve in zoomed. The dashed red line shows the assumed underlying background which is to be removed. In this case it seems to consist of two power law segments.

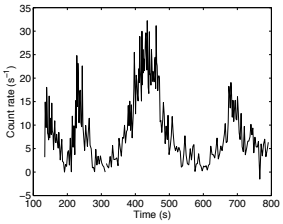

(c) The background subtracted flares.

Figure 3.9: The XRT light curve of GRB 050730, the flare part of the light curve in zoomed, and the background subtracted flares.

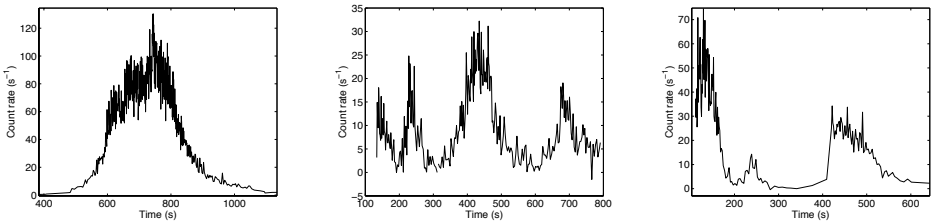

(a) GRB 050502B (b) GRB 050730 (c) GRB 050822

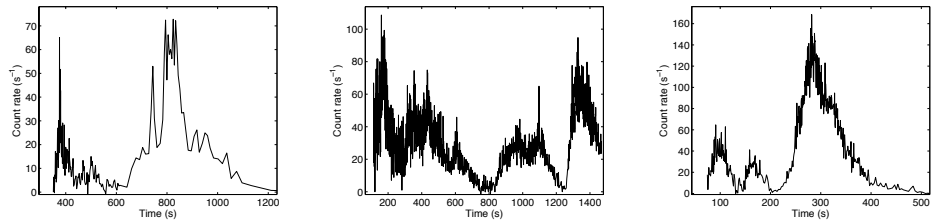

(d) GRB 050922B (e) GRB 051117A (f) GRB 060111A

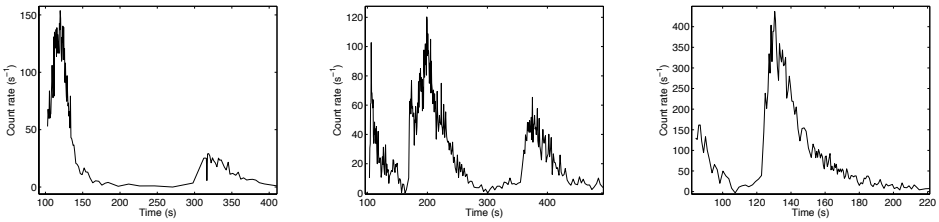

(g) GRB 060204B (h) GRB 060210 (i) GRB 060418

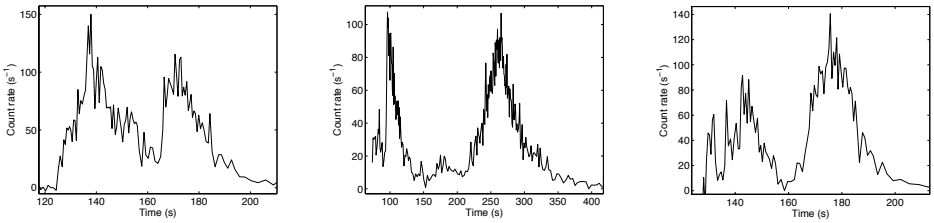

(j) GRB 060604 (k) GRB 060607A (l) GRB 060714

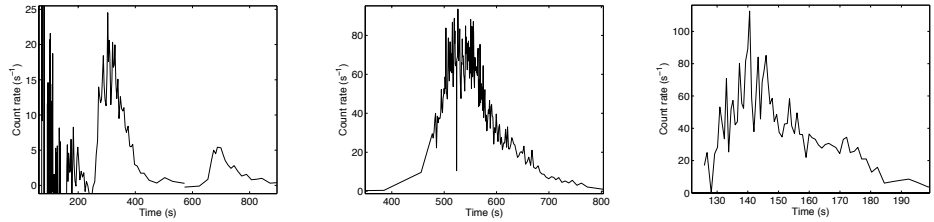

(m) GRB 060904A (n) GRB 060929 (o) GRB 061202

Figure 3.10: The background subtracted X-ray flares from the X-ray flare sample. The flare in GRB 050502B doesn't look like a single pulse. It rather looks as it consists of three pulses. For that reason only the part to the right is used in a fit, not the whole pulse.

Chapter 4

Results

The pulses from the BAT and XRT samples are fitted with `srice2.pro`. To be able to see a possible correlation between the parameters from the fits several plots are made, which are showed below. In this chapter I summarize the results found from the fits. These are then discussed in chapter 5.

4.1 Comments about the results

For BAT, the good fits (corresponding to the GRBs with stars in column 4 in table 3.1) are plotted in red, and the less good fits are plotted in in blue. In the figures there are a circle and two crosses plotted. The circle corresponds to the pulse in GRB 061202, whose light curve is shown in figure 4.1. This is not a clear single pulse, as the ones in the BAT sample. It can either consist of one or two pulses, depending on the interpretation or "ideas" about its appearance. Fits have been made for the pulse considered as one pulse (these parameters are plotted as the circle in the figures) but also for it as considered as two pulses (with the fits for the two pulses plotted as the two crosses). Both cases are plotted in the figures, to see which case that fits most with the other pulses. Since it isn't a typical well separated single pulse the fit parameters for the pulse (either seen as one or two pulses) are not included in any results. The parameters for the pulse/pulses are only plotted to see if the they behave differently than the other clean single pulses. By examining its behavior conclusions can hopefully be made on whether a pulse like this should be used as a single pulse or not.

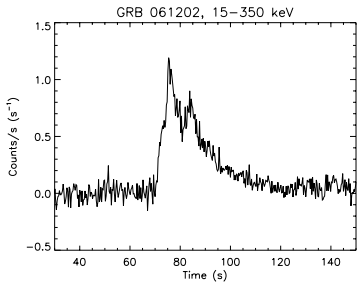

Figure 4.1: The light curve of GRB 061202 consists of a pulse which could be treated either as one pulse, with a varying background, or a superposition of two pulses.

4.1.1 How to compute the rise and decay times

The rise time is the time between where the pulse during its rise phase gets a flux that is half of its maximum flux, and the time of its maximum flux. Correspondingly the decay time is the time between the time of the pulse's peak and the time during the decay phase where the pulse's flux is half of its maximum value. From the fits the rise or decay times of the pulses are not obtained, but t_{max} and f_{max} are, and from them the rise and decay times can be computed. To obtain these first the obtained parameters from a fit are used to plot the pulse, after moving it down a value of $f_{max}/2$. This means that the pulse's half maximum is at the x-axis. The intersection between the x-axis and the pulse corresponds to the times t_1 and t_2. The rise time is then computed by $t_r = t_{max} - t_1$, and the decay time is computed from $t_d = t_2 - t_{max}$.

4.1.2 The γ-ray and X-ray energy flux

When plotting the flux light curves units of counts/s has been used. Many times the counts rates for the XRT pulses are higher than for the BAT pulses (compare the light curves of the prompt pulses in figure 3.6 with the light curves of the flares in figure 3.10). However, the count rates are from different instruments and can't be compared with each other. The count rates can nevertheless be translated into energy fluxes, and these can be compared.

To compute the energy flux for a BAT light curve the PIMMS web site `http://heasarc.gsfc.nasa.gov/Tools/w3pimms.html` is used. On the web site the detector and quantity to converted from and to are chosen. For example convert from "Swift/BAT count rate per detector" to flux. The input and output energy ranges should be filled in. To convert from count rate to flux in the same energy interval the same value is filled in in both places. It could however be interesting to compare BAT fluxes with XRT fluxes in a specific GRB. This is done by filling in the BAT energy range as the input energy range, and the XRT energy range as the output energy range.

The count rates and energy fluxes for GRB 060904B are showed in figure 4.2. In this way the energy fluxes in the different energy bands can be compared. The BAT count rates are also converted into energy flux in the energy range of XRT, so that the fluxes can be compared in the same energy band. This is showed in figure 4.3. Note that there is a little pulse in BAT at the same time as the flare in XRT.

4.2 BAT pulse parameters

The fits of the pulses in the total energy range (energy channel 1-4 (15-350 keV)) from the light curves from BAT yield the parameters displayed in table E.1. The parameters obtained from the fits are r, d, t_{max}, f_{max}, $FWHM$ and $FW75\%$, with errors, c without errors, and the χ^2-value for all the fits.

4.2.1 The rise and decay indices

The distributions of r and d are showed in figure 4.4(a) and (b). The average values of r and d are calculated to 2.7 ± 1.1 and 3.3 ± 1.7, respectively. The decay index d as a function of r is plotted in figure 4.4(c). This shows no correlation.

4.2.1.1 Uncertainties in the rise and decay indices

As can be seen in table E.1, there are sometimes large uncertainties in the r and d power law indices. The uncertainties can be explained by the parameters being

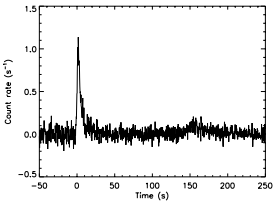

(a) A pulse in GRB 060904B. The flux is measured in counts/s.

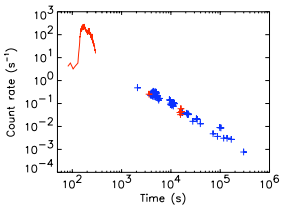

(b) XRT light curve of GRB 060904B. Flux in counts/s.

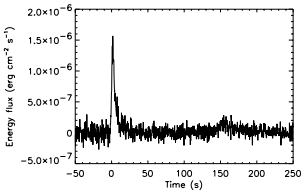

(c) The pulse in GRB 060904B with flux in erg cm^{-2} s^{-1}.

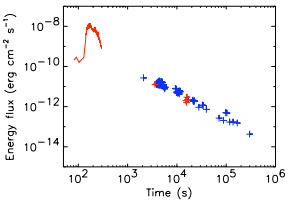

(d) XRT light curve of GRB 060904B with flux in erg cm^{-2} s^{-1}.

Figure 4.2: BAT and XRT light curves with the flux measured in counts/s and erg cm^{-2} s^{-1}.

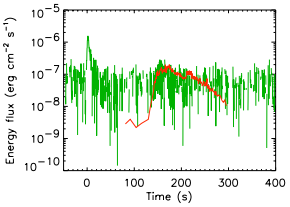

(a) XRT data (red) converted into the energy range of BAT.

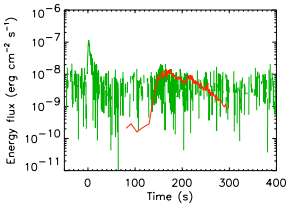

(b) BAT data (green) converted into the energy range of XRT.

Figure 4.3: XRT energy flux converted into the BAT energy range, and BAT energy flux converted into the energy range of XRT. The data from BAT is plotted in green.

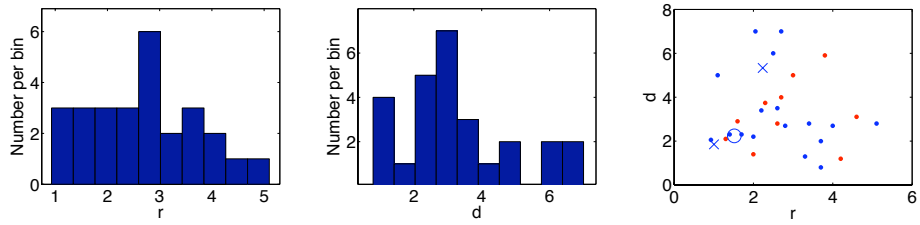

(a) (b) (c)

Figure 4.4: The distribution of r and d, and d as a function of r for the whole sample.

correlated. The rise index r as a function of d for the whole BAT sample is showed in figure 4.4(c). This shows no correlation. However, when fitting a single pulse in `srice2.pro`, it is sometimes possible that different sets of initial conditions generate

different fits. The parameters that changes between these fits are often r and d. The values of the other parameters doesn't seem to change much. To examine this closer for a pulse r is varied, without changing the values for t_0, t_{max} or f_{max}, and the fit is re-made several times to see if d from the fit changes; if it is the values of the parameters are noted. This is made for GRB 061021. The values of r and d obtained from the fits are displayed in figure 4.5. They are indeed correlated. The correlation coefficient is 0.97.

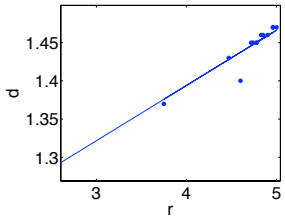

Figure 4.5: d as a function of r for GRB 061021. The different values of r and d are obtained from different fits, obtained from different initial values. Hence, in a single pulse the indices r and d are correlated.

4.2.2 Properties of pulses with different pulse widths

In figure 4.6(a) t_r is plotted as a function of $FWHM$. The plot shows a clear linear correlation with the value of 0.98 for the linear correlation coefficient R. Linear regression with unknown errors is performed and the slope is measured to 0.34 ± 0.01. Reasonably a correlation between t_d and $FWHM$ will also exist. The decay time t_d plotted as a function of $FWHM$ is plotted in figure 4.6(b), and also show a correlation. The correlation coefficient is very large, $R = 0.99$, and the slope is measured to 0.66 ± 0.02. Since both t_r and t_d show correlations with $FWHM$ there should also be a correlation between t_r and t_d, and that is also found to be the case, see figure 4.6(c). The correlation coefficient is in this case 0.96 and regression yield the value of 0.50 ± 0.03 for the slope. In figure 4.6(d) the correlations of t_r and t_d and $FWHM$ are showed in a three dimensional graph.

Between $FWHM$ and t_d/t_r there is a weak correlation that long bursts are more symmetric. This can be seen in figure 4.6(e). Nonetheless, the ratios are approximately constant. The mean value is $< t_d/t_r >= 1.94 \pm 0.69$, which also can be seen in the figure. The pulse width $FW75\%$ plotted as a function of $FWHM$ shows a clear linear correlation (figure 4.6(f)). The slope is 0.59 ± 0.01, and the linear correlation coefficient has a value of $R = 1.00$. In figure 4.8(a) the distribution of t_d/t_r is shown. The values of t_d/t_r range between 1.2 and 4.4.

4.2.3 Properties of pulses occurring at different times

The peak flux as a function of the peak time is showed in figure 4.7(a). The peak flux decreases for increasing t_{max} values. In figure 4.7(b) $FWHM$ as a function of t_{max} is shown. There doesn't seem to be a correlation. Figure 4.7(c) and (d) shows r and d as functions of t_{max}. Neither here there seem to be correlations.

Figure 4.8(b) shows the distribution of $FWHM/t_{max}$. The values range between -14.3 and 10.8, with an average value of 1.5 ± 4.1. Figure 4.8(c) shows $FWHM/t_{max}$ as a function of t_{max}. Disregarding two outliers, the ratios are approximately constant with increasing values of t_{max}. The large ratios of $FWHM/t_{max}$, at small values of t_{max}, are explained by that $FWHM$s are divided by values less than one of t_{max}.

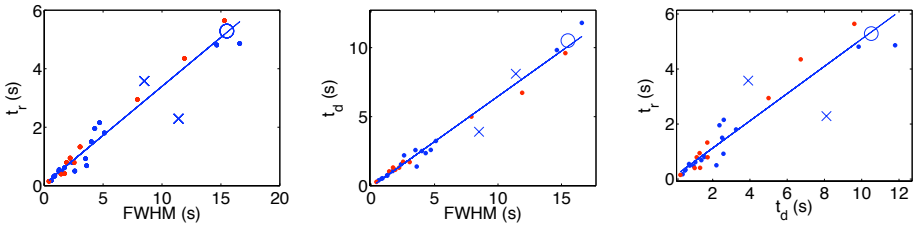

(a) t_r as a function of $FWHM$. The slope is 0.34 ± 0.01 and the correlation coefficient $R = 0.98$.

(b) t_d as a function of $FWHM$. The correlation coefficient $R =$ 0.99 and the slope is 0.66 ± 0.02.

(c) t_r as a function of t_d. The slope is 0.50 ± 0.03 and the correlation coefficient is 0.96.

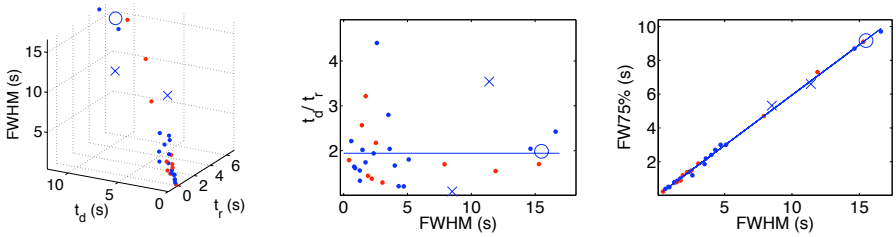

(d) The correlations of t_r, t_d and $FWHM$ in a three dimensional graph.

(e) t_d/t_r as a function of $FWHM$. The average value is 1.94 ± 0.69.

(f) $FW75\%$ as a function of $FWHM$. The line has a slope of 0.59 ± 0.01 and the correlation coefficient is 1.00.

Figure 4.6: Relations between t_r, t_d and $FWHM$. The figure also shows the relation between the asymmetry and $FWHM$, and between $FW75\%$ and $FWHM$.

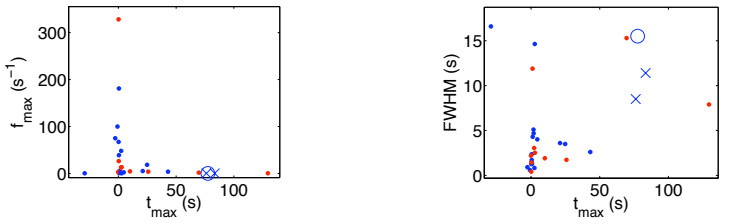

(a) f_{max} as a function of t_{max}.

(b) FWHM as a function of t_{max}.

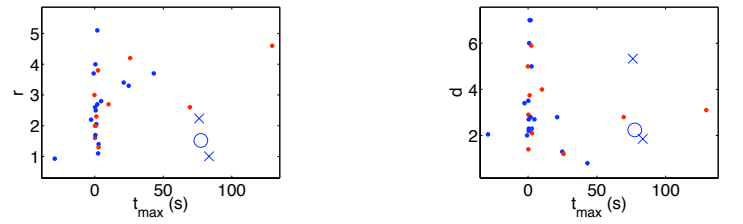

(c) r as a function of t_{max}.

(d) d as a function of t_{max}.

Figure 4.7: f_{max}, $FWHM$, r and d as functions of t_{max}.

4.2.4 The decay slope as a function of asymmetry

In figure 4.9(a) d is plotted as a function of $t_r/FWHM$. Since

$$\frac{t_r}{FWHM} = \frac{t_r}{t_r + t_d} = \frac{1}{1 + \frac{t_d}{t_r}}, \tag{4.1}$$

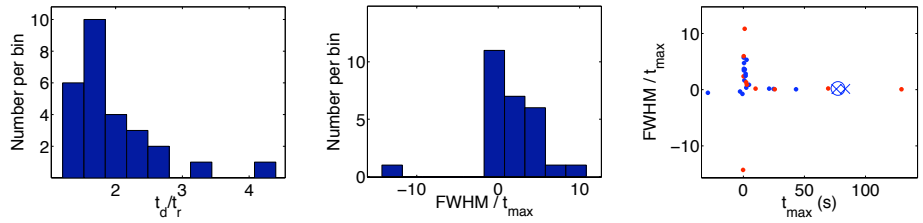

(a) (b) (c)

Figure 4.8: The distribution of t_d/t_r and $FWHM/t_{max}$, and $FWHM/t_{max}$ as a function of t_{max}.

this is the same as plotting d as a function of $1/(1 + t_d/t_r)$. As mentioned before t_d/t_r is almost constant. A correlation is shown but it is not clear whether it is a logarithmic function, an exponential or something else. If the values follows a power law:

$$y = Ax^k \tag{4.2}$$

plotting the logarithms of the values for the "x and y axes" should show a straight line, since

$$\log(y) = \log(Ax^k) = k \cdot \log(x) + \log(A) \tag{4.3}$$

has the form of a straight line, $y = kx + m$. If the values instead follow an exponential:

$$y = Ae^{kx}, \tag{4.4}$$

taking the natural logarithm of the "y values" give

$$\ln(y) = \ln(Ae^{kx}) = k \cdot x + \ln(A) \tag{4.5}$$

which also is the form of a straight line. To see if the data follows a power law or an exponential a test is to take the logarithm of the "x- and y axes" and the natural logarithm of the "y values", and plot it, to see if any of it produces a straight line. If both does, the correlation coefficient can be used to examine which that shows the strongest correlation.

If values are distributed as a power law, so that the logarithms of the "axes" makes a straight line and regression is made, the received m value is equivalent to log (A), as in equation 4.3, where A is from the form of the power law (equation 4.2). To receive A, 10^m has to be taken. If the values instead are distributed as an exponential, so that taking the natural logarithm of the "y values" creates a straight line and linear regression is made, the m value from the regression corresponds to $\ln(A)$ from equation 4.5. Similarly, in order to get A in equation 4.4, e^m has to be performed.

To examine whether the data in figure 4.9(a) follows a power law or exponential the logarithms of the "axes" are taken and the correlation coefficient R is calculated, and the natural logarithm is taken of the "y values", and another correlation coefficient is calculated. Both produces a straight line, but the largest correlation coefficient corresponds to taking the natural logarithm, and therefore the values correspond to a exponential. Figure 4.9(b) shows the situation after taking the natural logarithm of the "y values". The correlation coefficient is 0.88. Linear regression yield a value of 6.5 ± 0.7 for the slope and a value of -1.2 ± 0.3 for m, which is equivalent with the exponential having a form of $y = 0.30 \cdot e^{6.5x}$. The exponential plotted with the values are showed in figure 4.9(c).

In figure 4.9(d), d as a function of $t_d/FWHM$ is plotted. The same procedure as above is performed after subtracting unity from the "y values" to make them

start at $y = 0$. Since t_d and t_r are correlated, figure 4.9(a) and (d) should show similar behaviors. After the natural logarithm of the "y axis" is taken, the data follows a straight line with slope -11.2 ± 1.9 and $m = 7.6 \pm 1.2$ (figure 4.9(e)), and the correlation coefficient is -0.76. The exponential behavior of the values in figure 4.9(d) is thus expressed as $y = 1998e^{-11.2x}$.

A plot of d as a function of t_r/t_d is shown in figure 4.9(f). There should be a correlation here since there is one between d and $t_r/FWHM$, as shown in figure 4.9(a) and between $FWHM$ and t_d, as shown in figure 4.6(b). A correlation is shown. The largest correlation coefficient is obtained when taking the natural logarithm of the "y axis", the values corresponding to a exponential. The same procedure as above is performed (but not subtracting unity from the values). After doing that the data follows a straight line, and linear regression yields the values 3.5 ± 3.9 for the slope and -0.9 ± 2.3 as the m value (figure 4.9(g)). The correlation coefficient is measured to 0.98. The correlation in figure 4.9(f) thus follows an exponential with the form $y = 0.41e^{3.5x}$.

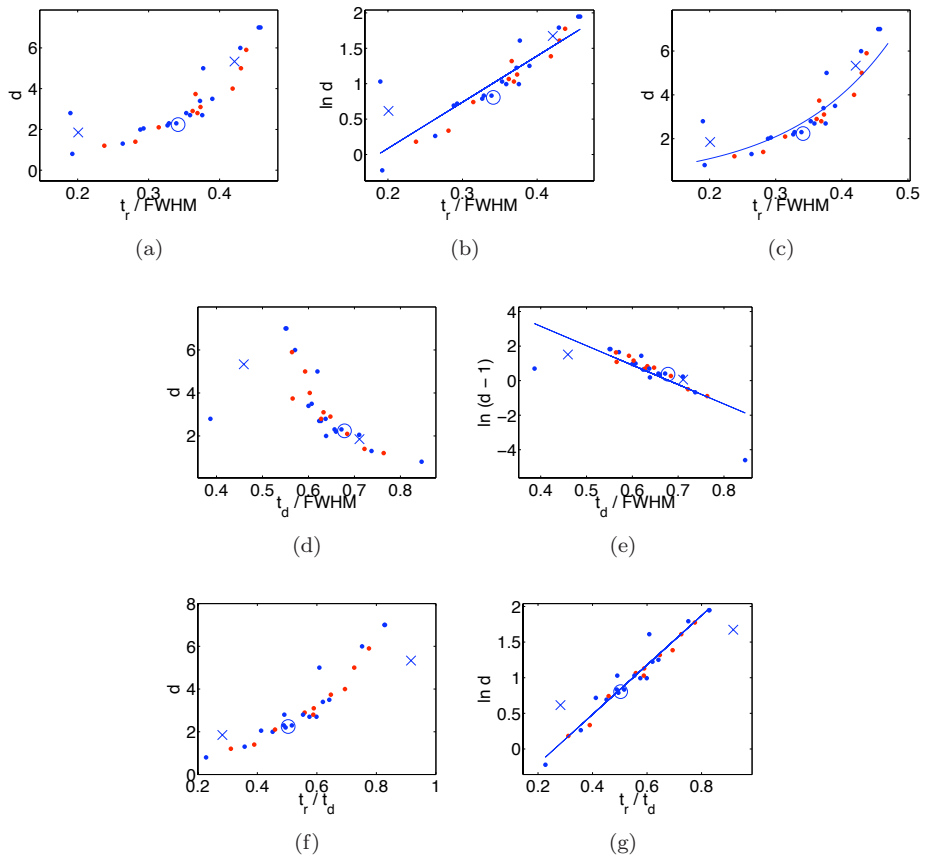

Figure 4.9: (a) d as a function of $t_r/FWHM$. (b) The natural logarithm of d as a function of $t_r/FWHM$. The slope of the correlation is 6.5 ± 0.7, m is -1.2 ± 0.3, and the correlation coefficient is 0.88 (c) d as a function of $t_r/FWHM$ with the exponential function $d = 0.30 \cdot e^{6.5 \frac{t_r}{FWHM}}$. (d) d as a function of $t_d/FWHM$. (e) The natural logarithm of $d - 1$ as a function of $t_d/FWHM$. (f) d as a function of asymmetry (t_r/t_d). (g) The natural logarithm of d as a function of the asymmetry.

4.2.5 Combinations of the rise and decay indices and the rise and decay times

In figure 4.10 different combinations of the parameters r, d, t_r and t_d are shown. Figure 4.10(a) shows t_d/r as a function of t_d. The correlation coefficient is $R = 0.89$ and the slope is 0.76 ± 0.08. Figure 4.10(b) show t_d plotted against t_r/r. Since there is a correlation between t_r and t_d, figure 4.10(a) and (b) should have a similar behavior, which also is the case. The correlation coefficient R is 0.93, and k and m is 0.35 ± 0.03 and -0.2 ± 0.1, respectively. Similar correlations are also expected from t_d/d as a function of t_r (the correlation coefficient is $R = 0.79$ and the slope is 0.7 ± 0.1) and t_r/d as a function of t_r (the correlation coefficient R is measured to 0.92 and the slope is 0.37 ± 0.03) (figure 4.10(c)) and (d)), as well as t_r/r as a function of t_r (the correlation coefficient $R = 0.85$ and the slope 0.63 ± 0.08) and t_d/r as a function of t_r (the correlation coefficient $R = 0.77$ and the slope 1.3 ± 0.2) (figure 4.10(e) and 4.10(f)) and t_d/d as a function of t_d (the correlation coefficient $R = 0.92$ and the slope is 0.42 ± 0.04) and t_r/d as a function of t_d (the correlation coefficient R is 0.99 and the slope 0.20 ± 0.01) (figure 4.10(g) and (h)).

4.2.6 Redshift correction

So far the analysis has not taken into account that the observed bursts are at different redshift. According to equation 1.27 pulses observed from bursts with large redshifts appear longer. If a burst that emits a one second pulse is at redshift $z = 1$ the pulse is observed as 2 seconds on earth, if the burst takes place at redshift $z = 2$, the observed pulse is 3 seconds, and so on.

Since the redshift is only available for a few bursts the analysis above has been made without correcting for it. To see if correcting for the redshift would affect the results found two of the plots are re-made, with only the bursts that have known redshifts, and compared to the earlier results. The new plots are made with the GRBs with redshift from table 3.1, the sample 'BAT redshift'. First, the redshift corrected decay time and rise time are plotted against each other, in figure 4.11(a). A correlation is found with a correlation coefficient of 0.98. The proportionality constant is calculated to 0.59 ± 0.04. The value calculated without correcting for redshift is 0.50 ± 0.03. The values are very close.

In figure 4.11(b) redshift corrected f_{max} as a function of redshift corrected t_{max} is displayed. Also in this case the correlation is very similar to the one gotten without correcting for redshift. It is just the scale that have changed. The pulses would have larger count rates and be observed at earlier times, if they would be observed in the co-moving frame.

The conclusion is that the results don't seem to be affected much of the different redshifts of the bursts, and so neglecting the redshift does not alter the correlations strongly.

4.3 XRT pulse parameters

As for the BAT pulses the parameters obtained from the fits with `srice2.pro` are r, d, t_{max}, f_{max}, $FWHM$ and $FW75\%$, with errors, c without errors, and the χ^2-value for all fits. The parameters are shown in table E.2. The values are plotted below in the same way as for the BAT data.

4.3.1 The rise and decay indices

The distributions of r and d are showed in figure 4.12(a) and (b). The average values are calculated to 2.8 ± 2.0 and 3.2 ± 1.5 respectively. Figure 4.12(c) shows

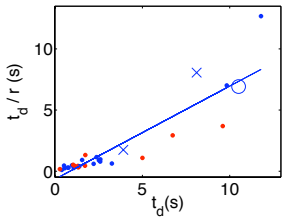

(a) t_d/r as a function of t_d. The proportionality has a constant of 0.76 ± 0.08 and the correlation coefficient $R = 0.89$.

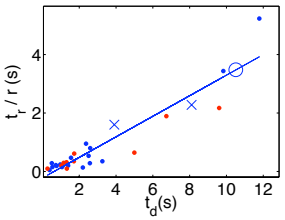

(b) t_r/r as a function of t_d. The correlation coefficient $R = 0.93$. The slope is 0.35 ± 0.03.

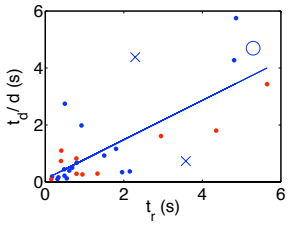

(c) t_d/d as a function of t_r. The correlation coefficient $R = 0.79$. The slope in this case is 0.7 ± 0.1.

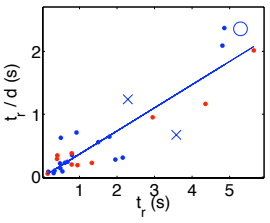

(d) t_r/d as a function of t_r. The slope is 0.37 ± 0.03 and the correlation coefficient $R = 0.92$.

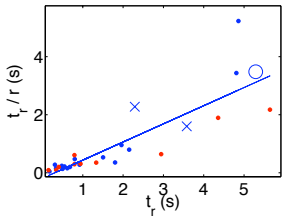

(e) t_r/r plotted against t_r. The slope is 0.63 ± 0.08, and the correlation coefficient $R = 0.85$.

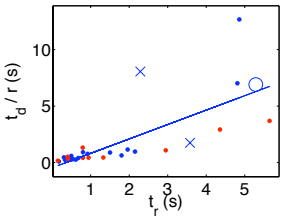

(f) t_d/r as a function of t_r. The correlation coefficient $R = 0.77$ and the slope is 1.3 ± 0.2.

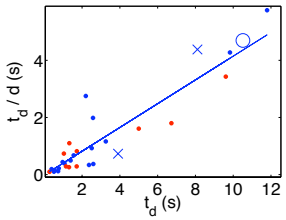

(g) t_d/d plotted against t_d. The correlation coefficient $R = 0.92$ and the slope has a value of 0.42 ± 0.04.

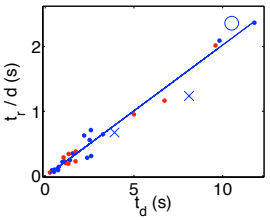

(h) t_d plotted against t_r/d shows a correlation with coefficient $R = 0.99$. The slope is measured to 0.20 ± 0.01.

Figure 4.10: Different combinations of r and d, t_r and t_d.

the decay index as a function of the rise index, showing no correlation.

4.3.2 Properties of pulses with different pulse widths

As for the data from BAT the rise time and decay time are plotted as functions of $FWHM$, and the rise time as a function of the decay time. See figure 4.13(a), (b) and (c). For t_r as a function of $FWHM$ there is a correlation with a slope of

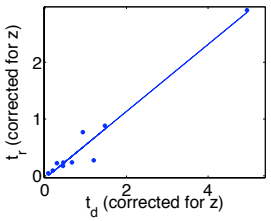

(a) t_r as a function of t_d, now corrected for redshift.

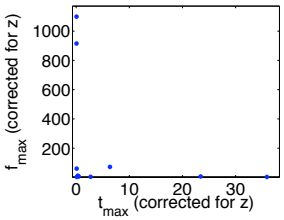

(b)

Figure 4.11: Redshift corrected t_r as a function of redshift corrected t_d, and redshift corrected f_{max} as a function of redshift corrected t_{max}.

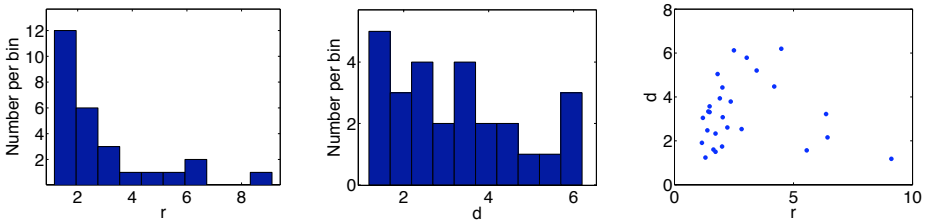

(a) (b) (c)

Figure 4.12: The distributions of r and d, and d as a function of r.

0.32 ± 0.02 where the correlation coefficient is 0.97. For t_d as a function of $FWHM$ the slope is measured to 0.67 ± 0.02 and the correlation coefficient is 0.99. For t_r as a function of t_d there is a correlation with correlation coefficient 0.92. The slope of the correlation is in this case measured to 0.46 ± 0.04. Figure 4.13(d) shows a 3D plot of the correlations between the rise time, decay time and $FWHM$. The ratio t_d/t_r as a function of $FWHM$ is shown in figure 4.13(e). The values show a weak correlation that long bursts are more symmetric. Nonetheless, the ratio t_d/t_r is approximately constant with varying $FWHM$. The mean value of t_d/t_r is computed to $< t_d/t_r >= 1.95 \pm 0.65$ (also plotted in the figure). Figure 4.13(f) shows $FW75\%$ as a function of $FWHM$, which shows a strong correlation (with correlation coefficient $R = 1.00$). The slope is 0.58 ± 0.01. Figure 4.15(a) shows the distribution of t_d/t_r. The values range between 1.3 and 4.2.

4.3.3 Properties of pulses occurring at different times

The peak flux as a function of the peak time is shown in figure 4.14(a). Note that the peak times are the times from the BAT trigger. There is a tendency for decreasing f_{max} for increasing t_{max}. Figure 4.14(b) shows $FWHM$ as a function of t_{max}. A linear correlation is found with a slope of 0.13 ± 0.02, and a correlation coefficient of $R = 0.78$. Figure 4.14(c) and (d) shows r and d as functions of t_{max}. For r as a function of t_{max} it is clear that for increasing t_{max} r decreases. The same tendency exist for d as a function of t_{max} but it is not as clear. Figure 4.15(b) shows the distribution of $FWHM/t_{max}$. The values range between 0.1 and 0.4 and the average value is calculated to 0.19 ± 0.09. Figure 4.15(c) shows $FWHM/t_{max}$ as a function of t_{max}. The ratio $FWHM/t_{max}$ is approximately constant for increasing values of t_{max}, but has a weak tendency for decreasing ratios as t_{max} increases.

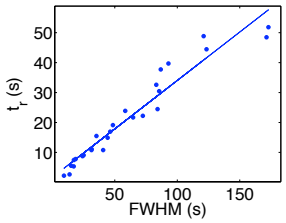

(a) t_r as a function of $FWHM$. The slope is measured to $0.32\pm$ 0.02 and the correlation coefficient R is 0.97.

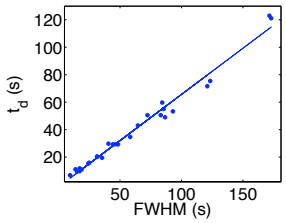

(b) t_d as a function of $FWHM$. The correlation coefficient $R =$ 0.99 and the slope is 0.67 ± 0.02.

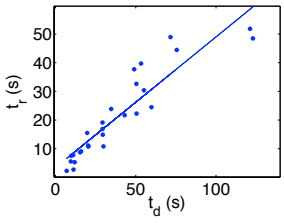

(c) t_r as a function of t_d. The slope is 0.46 ± 0.04 and the correlation coefficient $R = 0.92$.

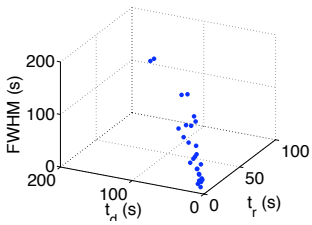

(d) The correlations between t_r, t_d and $FWHM$.

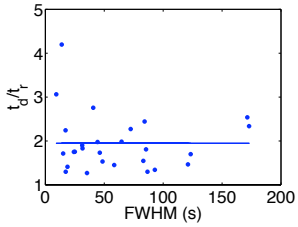

(e) t_d/t_r as a function of $FWHM$. The average value is 1.95.

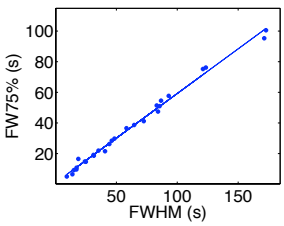

(f) $FW75\%$ as a function of $FWHM$. The slope is 0.58 ± 0.01 and the correlation coefficient $R = 1.00$.

Figure 4.13: Relations between t_r, t_d and $FWHM$, t_r and t_d, the asymmetry and $FWHM$ and $FWHM$ and $FW75\%$.

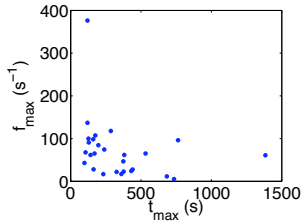

(a) f_{max} as a function of t_{max}.

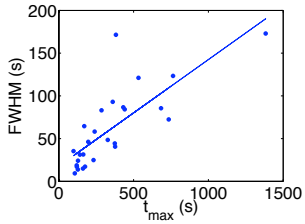

(b) $FWHM$ as a function of t_{max}. The slope is 0.13 ± 0.02 and the correlation coefficient $R = 0.78$.

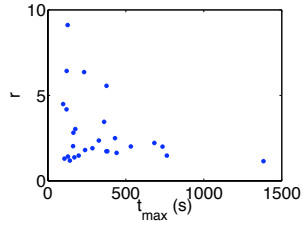

(c) r as a function of t_{max}.

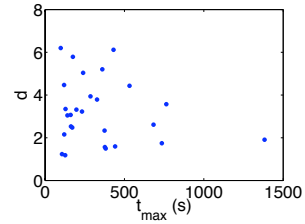

(d) d as a function of t_{max}.

Figure 4.14: f_{max}, $FWHM$, r and d as functions of t_{max}.

4.3.4 The decay slope as a function of asymmetry

In figure 4.16(a) $\ln d$ is plotted as a function of $t_r/FWHM$. Linear regression yield the values 7.6 ± 0.3 for the slope and -1.6 ± 0.1 for the m-value (with a correlation coefficient $R = 0.98$). The straight line is also plotted in figure 4.16(a).

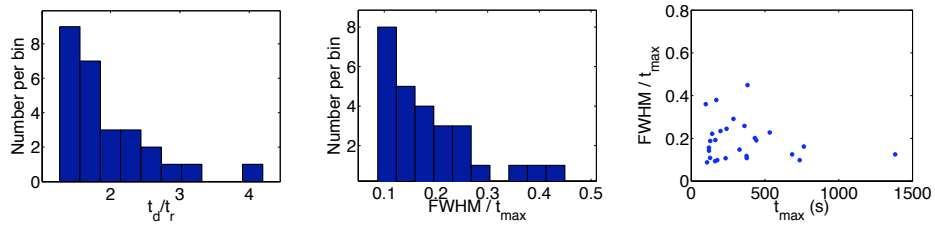

Figure 4.15: The distribution of t_d/t_r and $FWHM/t_{max}$, and $FWHM/t_{max}$ as a function of t_{max}.

The values correspond to an exponential of the form $d = 0.20e^{7.6 \cdot \frac{t_r}{FWHM}}$. Figure 4.16(b) shows $\ln(d-1)$ as a function of $t_d/FWHM$. The values in this case correspond to an exponential of the form $d = 10431e^{-13.5 \cdot \frac{t_d}{FWHM}}$. (The correlation coefficient $R = -0.98$.) In figure 4.16(c) $\ln d$ is plotted as a function of t_r/t_d. The values correspond to an exponential of the form $d = 0.46e^{3.3 \cdot \frac{t_r}{t_d}}$. (The correlation coefficient $R = 0.99$).

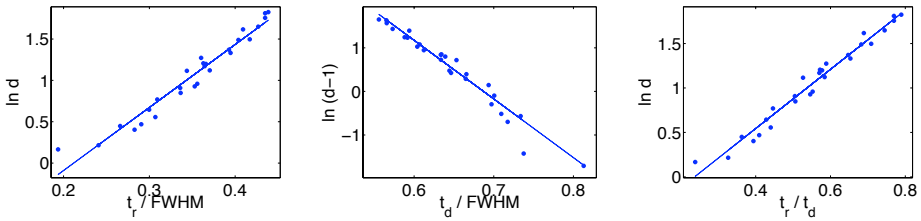

(a) (b) (c)

Figure 4.16: $\ln d$ as a function of $t_r/FWHM$, $\ln(d-1)$ as a function of $t_d/FWHM$ and $\ln d$ as a function of t_r/t_d.

4.3.5 Combinations of the rise and decay indices and the rise and decay times

Figure 4.17 shows different combinations of the parameters r, d, t_r and t_d. The strongest correlations are seen for t_r/r as a function of t_d and t_r/d as a function of t_d. The correlation coefficients are in these cases 0.93 and 0.96 and the slopes 0.32 ± 0.02 and 0.23 ± 0.01 respectively.

4.4 Prompt emission – X-ray flare correlation

To examine whether there is a relation between the number of emission episodes in the prompt emission and in the X-ray afterglow, the BAT and XRT light curves are plotted beside each other (see appendix C), and the numbers of emission episodes in each light curve are counted. See table 3.2 where the number of emission episodes are showed for each GRB and table 4.1, where the distribution of the occurrence of different number of emission episodes in BAT and XRT is displayed.

4.5 Summary of results

The main results from the BAT data are summarized as follows.

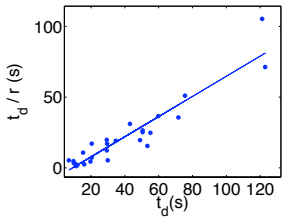

(a) t_d/r as a function of t_d. The proportionality has a constant of 0.71 ± 0.05 and the correlation coefficient $R = 0.94$.

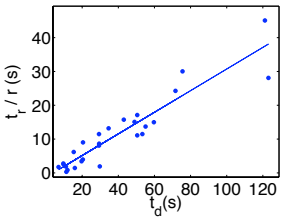

(b) t_r/r as a function of t_d. The correlation coefficient $R = 0.93$. The slope is 0.32 ± 0.02.

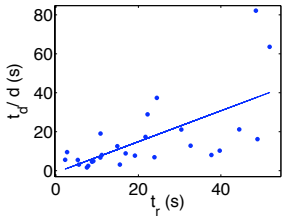

(c) t_d/d as a function of t_r. The correlation coefficient $R = 0.65$. The slope in this case is 0.8 ± 0.2.

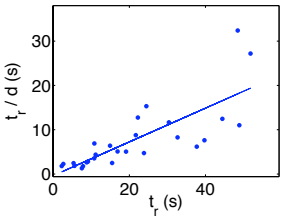

(d) t_r/d as a function of t_r. The slope is 0.38 ± 0.06 and the correlation coefficient is $R = 0.78$.

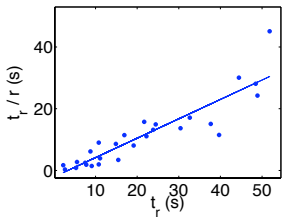

(e) t_r/r plotted against t_r. The slope is 0.63 ± 0.06, and the correlation coefficient $R = 0.90$.

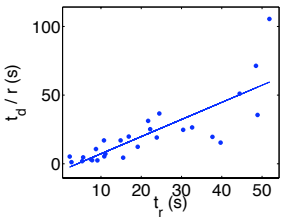

(f) t_d/r as a function of t_r. The correlation coefficient $R = 0.81$ and the slope is 1.2 ± 0.2.

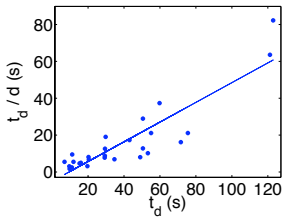

(g) t_d/d plotted against t_d. The correlation coefficient $R = 0.89$ and the slope has a value of 0.54 ± 0.05.

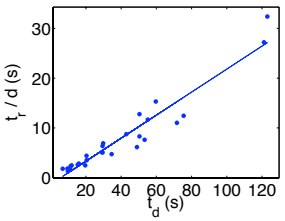

(h) t_d plotted against t_r/d shows a correlation with coefficient $R = 0.96$. The slope is measured to 0.23 ± 0.01.

Figure 4.17: Different combinations of r, d, t_r and t_d.

1. There is no correlation between the power law indices r and d. The average values of r and d are $< r >= 2.7 \pm 1.1$ and $< d >= 3.3 \pm 1.7$.

2. Strong correlations are found between t_r and t_d and $FWHM$, between t_r and t_d and between $FWHM$ and $FW75\%$.

3. There is a weak correlation between t_r/t_d and $FWHM$. For large $FWHM$s the ratio of t_r/t_d approaches 1. The values of t_d/t_r range between 1.2 and

Number of BAT emission episodes	Number of XRT emission episodes	Total number
1	1	3
1	2	2
1	3	1
1	4	1
2	1	2
2	2	3
2	3	1
3	2	1
3	3	1
3	5	1

Table 4.1: The distribution of the number of emission episodes in BAT and XRT.

4.4, and the mean value is calculated to $< t_d/t_r >= 1.94 \pm 0.69$.

4. A correlation is found between f_{max} and t_{max}. As the times get larger, the maximum flux decreases.

5. Correlations are not found between $FWHM$, r or d as functions of t_{max}.

6. The values of $FWHM/t_{max}$ range between -14.3 and 10.8. The average value is 1.5 ± 4.1.

7. The ratio $FWHM/t_{max}$ is approximately constant for increasing values of t_{max}.

8. Correlations are found between d and $t_r/FWHM$, $t_d/FWHM$ and t_r/t_d (the asymmetry). The data follows exponential functions.

9. There are linear relations between t_d/r and t_d, t_r/r and t_d, t_d/d and t_d, t_d/d and t_r, t_r/r and t_r, t_d/r and t_r, t_r/d and t_r and t_r/d and t_d

10. The data does not seem to be affected by different redshift.

The main results from the XRT data are

1. There is no correlation between the power law indices r and d. The average values of r and d are 2.8 ± 2.0 and 3.2 ± 1.5 respectively.

2. Strong correlations are found between t_r and t_d and $FWHM$, t_r and t_d, and $FWHM$ and $FW75\%$.

3. The ratio t_d/t_r show a weak correlation with respect to the widths ($FWHM$s) of the pulses. Large $FWHM$ seem to give a ratio of t_d/t_r that approaches 1. The values range between 1.3 and 4.2 with a mean value of $< t_d/t_r >= 1.95 \pm 0.65$.

4. A tendency for a correlation is found between f_{max} and t_{max}. For increasing values of t_{max} the values of f_{max} seem to decrease.

5. A correlation is found between $FWHM$ and t_{max}. The correlation coefficient is 0.78. For increasing values of t_{max} the values of $FWHM$ increases linearly. The slope of the correlation is 0.13 ± 0.02.

6. A correlation between r and t_{max} is found. For larger values of t_{max} r gets lower. For d as a function of t_{max} a correlation is not as clear as between r and t_{max}, but there is a tendency that even d decreases when t_{max} increases.

7. The values of $FWHM/t_{max}$ range between 0.1 and 0.4. The average value is calculated to 0.19 ± 0.09.

8. The ratio $FWHM/t_{max}$ is more or less constant for increasing values of t_{max}.

9. There are correlations between d and $t_r/FWHM$, $t_d/FWHM$ and t_r/t_d. The data follows exponential functions.

10. Linear relations are found between t_d/r and t_d, t_r/r and t_d, t_d/d and t_d, t_d/d and t_r, t_r/r and t_r, t_d/r and t_r, t_d/d and t_d and t_r/d and t_r.

Furthermore, no correlation is found between the number of emission episodes of BAT and XRT.

The X-ray flares and γ-ray pulses sometimes occur simultaneously.

Chapter 5

Discussion

There are as previously mentioned two main models that explain the origin of the flares. In the refreshed shock model slow shells emitted during the prompt phase are assumed to catch up with the afterglow at late times and re-brighten it, in which case the flares would have an external origin. In the long-lasting central engine activity model the central engine instead is assumed to remain active for a long time, or be re-started, the flares arising from internal origin. More details can be found in section 5.9. With the refreshed shock scenario one could expect differences between the prompt pulses and the flares, since they are created in different ways – the prompt emission is created by internal shocks while the flares are created in external shocks. The shell that produces the afterglow could have different properties than the prompt shells, for example it could be more expanded. In the long-lasting activity model on the other hand, there shouldn't be differences between the pulses observed by BAT and XRT, since it is the same process that creates all pulses.

5.1 Pulse/double pulse and good/less good fits

As can be seen in the plots, the fit to GRB 061202 as a single pulse (the circle) seem to follow the data best. The pulse seem to "be" a single pulse even though it has two peaks, which is visible in figure 4.1. However, this test is made from only one pulse and the behavior in the plots could just depend on the specific properties of this pulse, and not all pulses with two peaks. Further investigation on more pulses would be needed.

It can also be seen in the plots that there isn't a large difference between the good and less good fits. The correlations wouldn't change strongly if only the good, or less good, fits would be considered.

5.2 The rise and decay indices

The average value of r for BAT is very close to the one found by Ryde et al. (2003) of $< r >= 2.6 \pm 0.4$. The average value of the decay index for XRT is also close to the one found by Chincarini et al. (2007a) of $< d >= 3.54 \pm 1.50$. Following the discussion in section 1.6.2 where it was shown that $\mathcal{D} \propto t^{-1}$, and the fact that the energy flux $F \propto \mathcal{D}^3$, the decay parts of the pulses (that are affected by the curvature) have a flux that is expressed as $F \propto t^{-3}$, that is, the decay indices of the pulses should lie around 3. The distributions of d for BAT and XRT are shown in figure 4.4(b) and 4.12(b). The scatter of the d indices can be explained by that the value 3 applies for the slope of the energy flux light curve. In this thesis it is the count

flux pulses that have been examined, and not the energy flux pulses. The count flux pulses and energy flux pulses don't look exactly the same. Additionally, Kumar & Panaitescu (2000) argue that the flux instead of being expressed as $F \propto t^{\alpha}\nu^{\beta}$ (see section 1.4.2. There is only a change in signs due to the definitions of the indices α and β.) should be $F \propto t^{\beta-2}\nu^{\beta}$ $(-1 < \beta < 2)$, where β is the spectral index for each photon spectrum (see section 1.4.2). This spectral index is different for different bursts, and bring that the values of the d parameter isn't exactly 3.

That there isn't a correlation between the r and d indices can be interpreted as that there are different processes creating the rise and decay phases. The rise phase (that is believed to show the actual behavior of the co-moving pulse) is assumed to be an effect of the time of the shell crossing that creates the radiation, while the decay phase is assumed to be an effect of the curvature effect. It can be noted that for the XRT data there is a weak trend, for small r and d values, that increasing values of r produces increasing values of d. This agree with the relation found that the indices are correlated for a single burst (see figure 4.5). The outliers in figure 4.12(c) can still represent real pulses, with a very fast rise and slow decay. Nevertheless, the values of r and d are uncertain, as discussed in section 4.2.1.1 so the result should be taken lightly.

5.3 Properties of pulses with different pulse widths

The relation between t_r and $FWHM$ is also found by Ryde et al. (2003) and Kocevski et al. (2003). The relations show that the shape of the pulses doesn't vary with the widths of the pulses, it is just a scale change. It could be that there is different amounts of material that collides, which would lead to different amounts of synchrotron radiation, creating pulses of different sizes, or that the shells move more slowly so that the shell crossing takes a longer time.

The average value of t_d/t_r is for XRT 1.95 ± 0.65. This can be compared to the value 2.35 ± 1.71 found by Chincarini et al. (2007b). The value of 1.94 ± 0.69 found for BAT can be compared with the value of 0.47 ± 0.08 that Kocevski et al. (2003) found for t_r/t_d. That the average value for both BAT and XRT is $< t_d/t_r > \approx 2 \Rightarrow t_d \approx 2 \times t_r$, so the decay part of the pulse is longer than the rise part, consistent with FRED behavior, and that the curvature mostly affects the decay part of the pulses.

The weak correlation that long bursts are more symmetric is contrary to the results found by Chincarini et al. (2007a) and Norris et al. (1996). However, Kocevski et al. (2003) find no correlation at all between the asymmetry and width of the pulses, when plotting asymmetry against the T_{90} pulse duration (the correlation coefficient calculated is 0.06), and the correlation found here is weak.

5.4 Properties of pulses occurring at different times

That the maximum flux of the pulses seem to get lower at larger times can be explained since as time passes the shells lose velocity due to interaction of the surrounding medium. When collisions occur by shells with lower velocity the power of the synchrotron radiation emitted is less (see equation 1.4). I note that it is difficult to explain the large flux of the flare in GRB 050502B at about 750 s considering that the intensity decreases with time, if the flare would be created from a slow shell emitted during the prompt phase. The flux shouldn't be larger than that of the prompt emission. For $FWHM$ as a function of t_{max} there is a difference between the results from BAT and XRT. The $FWHM$ seem to increase for increasing times for XRT, but not for BAT. However, the times considered for

the BAT results are so small. When looking at the same time interval for the XRT data, there isn't a clear correlation either.

That the pulses get wider with time (that is found for the XRT data) can be explained by that the shells slow down with time, and the curvature effect. For a jet with a very large velocity the shell crossing is very fast, and the time until the maximum flux is obtained is short. The cooling time is also faster for electrons with large velocities. There is also a very rapid change in the number of photons observed, when time passes, due to the curvature effect, for a fast shell. This would mean that both r and d should decrease with increasing time. This is not clear for BAT but for XRT. Again, this can be an effect of the different time scales studied for BAT and XRT.

Chincarini et al. (2007a) found that the decay slope as a function of time can be described as $d = 2.45 + 0.418t$ for $t < 10000$ s for the flares. I however find a weak correlation that the decay slope decreases for increasing times for the XRT data. This could be explained by that different times are used when computing the decay slopes. The times used by Chincarini et al. (2007a) to compute the decay slopes are gotten from where the pulse crosses the fraction f of the peak emission. They chose a value of $f = 0.01$. However, as they discuss, changing this value yields very different slopes. I use a time set by hand. When changing it I also get different values of the rise and decay slopes.

The distributions of $FWHM/t_{max}$ are different for BAT and XRT as can be seen in figures 4.8(b) and 4.15(b). For BAT the pulses have values of $FWHM/t_{max}$ that range between -1 and 11 with an outlier at -14. The average value is calculated to 1.5 ± 4.1. For XRT all values are below 0.5, and the mean value is calculated to 0.19 ± 0.09. The BAT distribution is however somewhat uncertain since the time t_{max} is calculated from the trigger times, where the trigger times is not always at the start of the first pulse (see some of the BAT sample light curves in figure 3.6). If there is a high background noise the actual trigger can be hidden in the background. The trigger time that BAT notes (for a flux above a certain value of the background flux) is then a time after the actual trigger. The outlier in figure 4.8(b) (GRB 060919) seem to lie far away from the other data but it is because it has a negative value of t_{max} ($t_{max} = -0.15$). If it had had, say, $+0.15$ instead, it would have created a value that would lie at the positive side of the histogram. The outlier thus exist because of the difficulty in determining an exact trigger time.

The distribution for XRT is however more certain since the flares occur at such large times. The uncertainty from where the trigger times actually are isn't so big. The mean value of 0.19 ± 0.09 can be compared with the value of 0.13 ± 0.10 found by Chincarini et al. (2007a). For the width of the pulses Chincarini et al. (2007a) instead of the $FWHM$ used the Gaussian width σ. The angular time scale is proportional to the radius of the shell (see section 1.6.2). This means that the flares that occur at late times (where the shell has gotten a large radius) should have a width that also is proportional to the radius (if they are created in external shocks) that is $FWHM/t_{max} \approx 1$ (since t_{max} also is proportional to the radius). The distribution thus show that the flares have a rapid variability, which is a strong argument against external shocks.

The $FWHM/t_{max}$ ratios are more or less constant with increasing t_{max} for the pulses and flares. For the BAT data there are outliers. These can be explained by the pulses having negative peak times, which is a result of the difficulty in determining exact trigger times, as discussed above. They can also result from division with values less than one.

5.5 The decay slope as a function of asymmetry

The relation found between $t_r/FWHM$ and d is surprising since there isn't a relation between r and d. As discussed before the rise time is thought to originate from the shell crossing time, which is believed to be independent of the fall slope of the pulse, which is an effect of the curvature of the jet front. If pulses are affected by curvature they should be asymmetric, and their decay index should be smaller than that from pulses not affected by curvature. In figure 4.9 one can see that it is the most asymmetric pulses that have the small d values. Pulses that are more symmetric have larger d values. An explanation for these can be that the shell crossing time scale dominates over the angular time scale. This bring that the pulses seen look more as they do in the co-moving frame.

The asymptotic behavior of the data points for large and small $t_r/FWHM$, is nevertheless expected. The ratio $t_r/FWHM$ can never be larger than 1, since the value of 1 corresponds to the rise time being the entire part of $FWHM$, which means that the pulse only would consist of a rise phase, and end abruptly after it. The ratio $t_r/FWHM$ can never be less than zero, since a value of zero corresponds to the rise time being 0 and therefore that the decay time takes up all of $FWHM$, meaning the rise time is very steep, and the entire pulse consists of the decay phase. The relation between $t_r/FWHM$ and d has also been found by Ryde et al. (2003) (with a correlation coefficient of $R = 0.86$) and Kocevski et al. (2003) (correlation coefficient $R = 0.80$). Since there is a correlation between t_r and t_d it is not strange that there is a correlation between $t_d/FWHM$ and d as well.

An interesting result is that the asymmetry t_r/t_d is expressed as the logarithm of the decay index. It is not clear what this relation depends on. For small d values the pulses are very asymmetric but when d gets big the pulses get very symmetric. Since a typical pulse has a fast rise and slow decay, a larger decay index directly generates a more symmetric pulse. There is a tendency that the decay index is larger for small values of t_{max} (at least for the XRT data). By plotting the asymmetry as a function of t_{max} (as in figure 5.1) for the XRT data however, the trend isn't really clear. A further investigation would be necessary but it is beyond the scope of this thesis.

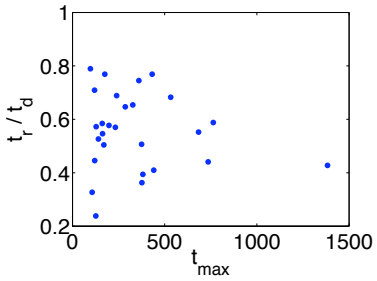

Figure 5.1: Asymmetry as a function of t_{max}.

The asymptotic behavior of t_r/t_d for small d is nevertheless expected. For small d, $t_d \to \infty$ and $t_r/t_d \to 0$. The correlation between the asymmetry and the decay index is also found by Ryde et al. (2003) and Kocevski et al. (2003). The correlation coefficient R in these cases are 0.97 and 0.83 respectively. In both cases the data seem to follow straight lines while the data gotten above is more likely to follow exponential functions. For r as a function of $t_r/FWHM$, $t_d/FWHM$ or t_r/t_d there is however no correlation at all. Commonly for all three correlations with d is that for larger values of d the pulses get more symmetric.

5.6 Combinations of the rise and decay indices and times

The correlations in the plots between the rise and decay indices and times can be explained by that there are strong correlations between the rise and decay times (0.96 and 0.92 for BAT and XRT respectively), and the values of r and d have a quite small sqatter. It is perhaps these correlations that are seen and dividing with r or d only changes these correlations a bit.

For the $t_d - t_r/r$ relation the correlation indices for BAT and XRT are both 0.93, while they are 0.99 and 0.96 (BAT and XRT) for the correlations between t_d and t_r/d, so the correlation seem to have decreased or be approximately the same for the $t_d - t_r/r$ relation but increased for the t_d and t_r/d relation.

5.7 Number of emission episodes in BAT and XRT

There is no correlation found between the number of emission episodes in BAT and XRT. The same result was found by Chincarini et al. (2007a). This means that flares occur randomly and don't depend on the prompt emission. Since many of the light curves have complex appearances, and exactly what is defined as a pulse, the numbers of emission episodes for both BAT and XRT are nevertheless somewhat uncertain. Also, the time it takes for XRT to slew to the position of the source makes that not all the emission, and perhaps flares, are detected. It is nevertheless interesting to study since a relation would be a very strong argument for the refreshed shock scenario.

That there isn't a correlation between the number of flares and gamma-ray pulses seem to rule out a version of the refreshed shock scenario, in which internal shocked shells cause external shocks, and one thereby could expect a correlation. Additionally, in some of the light curves a flare is seen simultaneously as a prompt pulse. Examples of this is shown in the BAT and XRT light curves of GRB 060418, 060607A and 060904B, which are shown in figure 5.2. For GRB 060418 there exists a small pulse at about 130 s. This seems to be at the same time as the flare in the XRT light curve. Similarly, GRB 060607A has a pulse at about 100 s in both BAT and XRT. The XRT light curve show additionally one pulse at about 300 s, but it is unclear whether this has a corresponding BAT pulse, since the BAT light curve ends at 130 s. GRB 060904B also has pulses in both BAT and XRT at about 150-200 s. In this case the flare is very strong. In the cases where the prompt pulses are very weak. If they had been a little weaker, they would have disappeared under the background, and only a flare would be visible. This means that the pulses have a blend of energies and one cannot say that the pulses and flares are different just from observing pulses/flares in different energy bands.

That the pulses and flares occur simultaneously makes it hard to draw a dividing line between them, in particular a naive view that prompt pulses are seen in γ-rays and flares in X-rays. One recent suggestion is given by Moretti et al. (2007), who argue that the spectra consist of a power law and probably a black body, and that the division between the prompt and afterglow phase should start at the time of the intersection between the power law and the decay of the black body.

Over all the behavior of the BAT and XRT data is very similar, which points to a common origin for the flares and the prompt pulses.

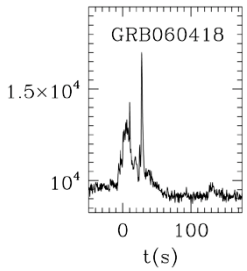

(a) BAT light curve of GRB 060418.

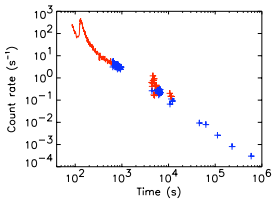

(b) XRT light curve of GRB 060418.

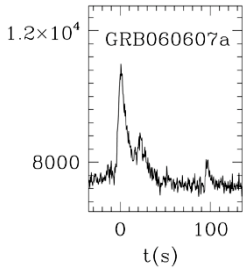

(c) BAT light curve of GRB 060607A.

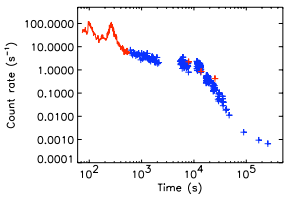

(d) XRT light curve of GRB 060607A.

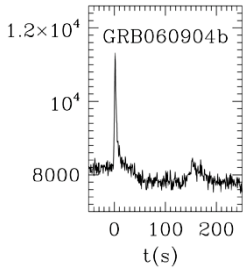

(e) BAT light curve of GRB 060904B.

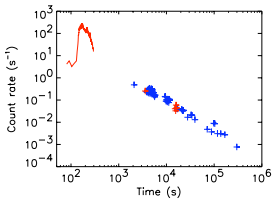

(f) XRT light curve of GRB 060904B.

Figure 5.2: BAT and XRT light curves showing that the flare exist the same time as a prompt pulse. (BAT figures from *Swift* web site.)

5.8 Other studies of the temporal properties of pulses and flares

There has been other studies performed of the temporal properties of both prompt pulses and flares.

5.8.1 Studies of γ-ray pulses

In a study of γ-ray pulses, Norris et al. (1996) for example examined temporal properties of bursts with a least square pulse fitting algorithm, and found that longer pulses have larger spectral lags and are more asymmetric. Most bursts examined had rise to decay ratios between 0.3 and 0.5. They also showed that the most frequently occurring pulse is an average between a Gaussian and an exponential. However, Zhang et al. (2007) studied a sample of 46 short and 51 long single GRBs and found no evidence of a connection between asymmetry and $FWHM$. Their results indicate that most pulses of long GRBs have a FRED shape. The average

value of the asymmetry was computed to 0.47. They also concluded that the pulses have a self-similarity across different energy channels.

Lee et al. (2000) studied a large sample of pulses and concluded that they have shorter rise times than decay times. They also found that the pulses peak earlier at higher energies and that pulses tend to be narrower at higher energies. They didn't find a correlation between the pulse's peak times and any other pulse characteristics, further supporting that the pulses arise from random and independent emission events. That the pulses tend to be narrower at higher energies was also found by Fenimore et al. (1995), and they showed that this narrowing with energy follows a power law of index -0.4.

Berger (2007) found a linear relation in 80% of the bursts in his sample between the γ-ray fluence and the afterglow X-ray flux. Kocevski et al. (2003) present an analytic function to analyze time profiles of FRED pulses (see section 3.2) from BATSE data. He found that the rise phase of pulses are best modeled with a power law of average index $< r >= 1.31 \pm 0.11$. The mean values of the decay index and rise time were computed to $< d >= 2.39 \pm 0.12$ and $< t_r >= 2.40 \pm 0.10$. Kocevski et al. (2003) also found that the pulse asymmetry has an average value of 0.47 ± 0.08. Between the asymmetry and the pulse width ($FWHM$) they found no relation.

Kocevski et al. (2003) however found a linear relation between t_r and $FWHM$. The slope was 0.32 ± 0.01 and the correlation coefficient $R = 0.981$. There was also a correlation between $t_r/FWHM$ and d. The correlation coefficient $R = 0.799$. The correlation shows that the larger part t_r is of $FWHM$ the larger the power law decay index gets. The decay index d also showed a correlation with the asymmetry (with correlation coefficient $R = 0.831$). The pulses that have large d values also have large asymmetries. Between r and the asymmetry there was however no correlation.

Ryde et al. (2003) studied a sample of 11 bursts observed by the INTEGRAL satellite and fitted the pulses with the function by Kocevski et al. (2003). Their results showed a very good correlation between t_r and $FWHM$ (a correlation coefficient of $R = 0.994$). The slope of the linear fit is 0.58 ± 0.02. A relation between the decay time and $FWHM$ is also found, but in this case the correlation coefficient R is only 0.942. The slope is 1.6 ± 0.2. A correlation between the asymmetry of the pulses and $FWHM$ is not found, but a relation between t_r and t_d is, with a slope of 0.31 ± 0.04 (correlation coefficient $R = 0.907$). Furthermore, Ryde et al. (2003) plotted the decay power law index d versus $t_r/FWHM$ and versus t_r/t_d. These correlations have the correlation coefficients $R = 0.86$ and $R = 0.97$ respectively. They also computed that the average values of the r and d power law indices are $< r >= 2.6 \pm 0.4$ and $< d >= 2.37 \pm 0.27$ respectively.

5.8.2 Studies of X-ray flares

A study has also been made of the properties of flares, by Chincarini et al. (2007a). Their sample consists of 69 flares from 33 GRBs observed by *Swift*. The GRBs are both long and short, and have both high and low redshifts. The flares have been fitted with a Gaussian model. They examined whether there was a correlation between the number of pulses detected by BAT, and number of flares detected by XRT, but did not find any. They found, however, that intensity ratios of successive BAT pulses and XRT flares were distributed the same way, and concluded that the relation between successive pulses and between successive flares are the same (on average the next event has a peak that is ~ 0.7 times the previous), which points to a common origin for the prompt pulses and flares. They concluded that 42% of the flares could be explained by the refreshed shock model, while all flares could be explained by the long-lasting central engine model. 10 bursts could however only be explained by a long-lasting activity of the central engine. Chincarini et al. (2007a)

computed the average value of the decay slope to 3.54 ± 1.50. The times before and after the flare were found in the intersection between the flare emission (the Gaussian model) and a fraction f of the flare peak emission. In the calculations the value of f was 0.01. However, as mentioned before the values of the decay slope changes a lot when changing the fraction f to another value. The fraction f is only an arbitrary value with no physical meaning. The values of the decay slope ranged between 1.3 and 6.8. The decay slope as a function of time is computed to $d = 2.45 + 0.418t$, where $t < 10000$. Chincarini et al. (2007a) computed t_r and t_d by using $f = 0.01$. By using $f = 0.05$ T_{90} could be calculated (since T_{90} is the time from which 5 and 95% of the flux is obtained). The values of the decay time divided by the rise time range between 0.5 and 8, with an average value of $< t_d/t_r >= 2.35$. A possible correlation between t_d/t_r and T_{90} is found. Their results showed also that the mean ratio between the width of the pulse and the time of the peak is $< \Delta t/t >= 0.13 \pm 0.10$. The peak times range between 95 s and 75000 s. Flares that occur late have longer durations but a lower peak intensity (strong correlation). Since they last longer their fluence can nevertheless be very large.

5.9 What are X-ray flares?

It is widely believed that γ-ray pulses arise from internal shocks, but it is unclear how the X-ray flares arise. There are two main models that explain their origin. One model is that the flares are created "internally" from a late-time activity of the central engine (Zhang (2006b), Burrows et al. (2007), Cusumano et al. (2006), Chincarini et al. (2007b), Godet et al. (2007), Guetta et al. (2006) and Zhang et al. (2006c)). This means that the same process creates both the prompt pulses and the flares (both created internally).

Flares could also be created by refreshed shocks (Granot et al., 2003), where the flares are assumed to be created from slow shells that were ejected *during* the prompt phase and catch up with the afterglow at late times, causing a re-brightening of the afterglow. Burrows et al. (2007) discuss that the flares can be created when shells with Lorentz factors that differ by only a small amount collide. The shells could also be emitted with very low Lorentz factors, as argued by Chincarini et al. (2007b). These collisions could occur over a wide range of timescales, and distances from the progenitor.

There are arguments that support the two models and arguments against them. For the long-lasting central engine activity model the arguments speaking for the model are that the large fluxes are easy to explain. For the internal shock model the flares could be produced with close to the same amount of energy compared to the prompt emission. The steep rise and decay times are also easy to explain, especially when the central engine is assumed to be re-started, since the clock then is re-set at the start of each flaring episode. Additionally, by studying five subsequent flares in GRB 060714, Krimm et al. (2007) find that the flares and the prompt emission show a similar morphology, and that the flares gradually evolve with time, which makes it probable that the flares and prompt pulses come from the same mechanism.

That the slope of the underlying emission often is the same before and after the flare points at that this emission and the flares come from different processes. If the flares were from refreshed shocks one would expect the flux level to be higher after the flare, since additional energy has been injected. An argument against the long-lasting activity model is that it is difficult to explain large flares several hours after the prompt emission, since the accretion to the black hole is supposed to be over in a short time (Woosley, 1993). If the accretion could be stopped for a time, it could explain late flares, but the disk would still be less massive than during the prompt phase, since it becomes less massive with time. A question in that case

would be what would stop the accretion. This issue has been addressed by Proga & Zhang (2006) who have a theory where the magnetic field around the black hole can stop the accretion. Zhang (2006b) provides several other scenarios.

Burrows et al. (2007) discuss that a large redshift can delay the flaring activity in the observers frame (and make the flares look wider then when emitted), which could explain the late flares. They however claim that the flaring for GRB 050904, with redshift $z = 6.29$, occurs for over an hour in the rest frame of the GRB. Additionally, the GRBs with flares don't have a significantly other mean redshift compared to GRBs without flares. A test of the curvature effect is performed by Liang et al. (2006), which indicates that the flares are distinct events of the central engine, and that the central engine remains active, sometimes up to a day, after the prompt emission is over. Additionally, Burrows et al. (2007) argue that the shapes of X-ray flares and X-ray pulses in the prompt emission are similar, which also favor the theory.

An argument speaking for the refreshed shock model is that the slope of the steep decay part of the afterglow (I in figure 1.6) is so steep that the central engine must have been switched off quickly (Kumar et al., 2007). However, a question is whether a slow shell can create such a fluence seen in the flares. Chincarini et al. (2007b) find it hard to believe that the flares are created without any additional energy input, due to the flare in GRB 050502B, which has a peak flux larger than 500 times that of the underlying afterglow (Falcone et al., 2006). If the flares are created from external shocks an energy compared to the initial blast wave would be required to make a noticeable change of the afterglow flux. The model neither can explain the rapid rise and fall times of the flares, since the curvature time scale is proportional to the radius of the shell (see equation 1.23), and the radius of the afterglow shell is very large. That is argued by Zhang (2006b). Since the rise and fall times of the flares typically are smaller than the time since the burst and since several flares are sometimes seen, Burrows et al. (2007) argue that the flares are created in internal shocks and so are related to the prompt emission, but at lower energies. The existence of multiple flares disfavors scenarios where only one flare can be created, for example the onset of the afterglow (Burrows et al., 2007). Since flares are detected in both long and short burst Zhang (2006b) argue that there should be a similar mechanism creating the flares in both cases. Chincarini et al. (2007b) believes that the origin of the flares not should depend on the progenitor or the environment surrounding it, but could be related to the accretion disk.

From the above discussion and from my results I argue that the origin of the pulses and flares are the same. This bring that the long time activity of the central engine must be explained. In order to explain this, and the flares, Proga & Zhang (2006) argue for a model in where the magnetic flux at the black hole, that increases with the in-falling material of the disk, stops the accretion. The X-ray flares are assumed to originate from when the accretion is re-started. Another theory is argued for by Perna et al. (2006) and King et al. (2005), where fragmentation of the disk, and subsequent accretion, is believed to create the X-ray flares.

5.10 Future prospects

In the future it would be interesting to examine bursts with flares that can be observed in the gamma-ray energy range and in the X-ray energy range simultaneously, to see if there is a connection between the flares and gamma-ray pulses at very early times. In the comparision between the number of emission episodes in BAT and XRT, the time intervals in the BAT light curves from the *Swift* web site were a bit short. It would be good to make light curves with larger time intervals. It could also be interesting to compute spectral lags for the pulses and flares to see if

there is any difference there. Investigating the spectra would probably also provide interesting information about the flares. These investigations, although important, are beyond the scope of this thesis.

Chapter 6

Conclusions

A gamma-ray burst light curve consists of pulses (seen in γ-rays) and flares (seen in X-rays). The goal of this thesis is to determine the origin of these flares. From the study made one can make six important notes:

- The asymmetry of the pulses and flares are described by the natural logarithm of the decay power law index – it is however not clear what this relation depends on
- Properties of pulses and flares are very similar
- The pulses and flares become fainter with time
- Flares have rapid and large scale variability
- There is no correlation between the number of pulses and number of flares
- Pulses and flares can occur simultaneously

Since the properties of the pulses and flares are similar and they become fainter with time one can draw the conclusion that the flares arise from a continuous and weakening central engine emission. That many of the flares have rapid and large scale variability is a strong argument against external shocks. That there isn't a correlation between the number of pulses and flares is a further argument against that they arise from the same process, and the simultaneous occurrence of some flares shows that there is no clear border line between the pulses and flares.

I therefore claim that the flares must be produced by a long-lasting central engine. In the general scenario the central engine is assumed to stay active for about 10-100 s but in this thesis I argue for a longer lasting engine. Possible explanations of this is fragmentation of the disk and subsequent accretion (King et al. (2005) and Perna et al. (2006)), or a halt in the accretion due to a strong magnetic flux accumulated at the black hole (Proga & Zhang, 2006).

However, it can be noted that differences between pulses and flares have been found. By studying five flares detected in GRB 060714, Krimm et al. (2007) found that the last three flares weren't consistent with the Amati relation (a relation between the energy of the peak and the isotropic energy), while the first two flares, and the prompt emission were.

A study of X-ray flares have previously been performed by Chincarini et al. (2007a) from a sample of 69 flares. They found that the ratio between the width of the pulses and the peak time is 0.13 ± 0.10, which can be compared to the value I found of 0.19 ± 0.09. They neither found a correlation between the number of BAT pulses and XRT flares. A strong correlation was however found between the time

of the peak and the peak intensity. My results only show a tendency for the same correlation. However, the time scale I study is much smaller. Both Chincarini et al. (2007a) and Norris et al. (1996) have found that short bursts are more symmetric, which is contrary to the results I find, but my results are only tentative.

Acknowledgments

I first of all would like to thank my supervisor Felix Ryde for giving me inspiration, good advice and encouragement. I have enjoyed this time. I also want to thank Milan Battelino, Luis Borgonovo, Jacob Trier Frederiksen, Stefan Larsson, Magnus Axelsson and Linnea Hjalmarsdotter in the high energy astrophysics group for appreciated help, interesting discussions and feedback on my work. Thanks also to Kjell Rosqvist for an interesting discussion about jet launching around black holes. Finally I want to thank Andrej Kuutmann and Niklas Höglund for company in the student room, and for practical help.

In this thesis I have used data supplied by the UK *Swift* Science data center at the university of Leicester.

Stockholm in December 2007.

Åsa Höglund

Bibliography

Bagoly, Z., et al. 2006, A&A, 453, 797

Barthelmy, S. D., et al. 2005, Space Science Reviews, 120, 143

Beloborodov, A. M. 2001, Gamma-ray Bursts in the Afterglow Era, 321

Berger, E. 2007, ArXiv Astrophysics e-prints, arXiv:astro-ph/0702694

Burrows, D. N., et al. 2005, Space Science Reviews, 120, 165

Burrows, D. N., et al. 2006, ESA Special Publication, 604, 877

Burrows, D. N., et al. 2007, ArXiv Astrophysics e-prints, arXiv:astro-ph/0701046

Chincarini, G., et al. 2007, ArXiv Astrophysics e-prints, arXiv:astro-ph/0702371

Chincarini, G., et al. 2007, ArXiv Astrophysics e-prints, arXiv:astro-ph/0701450

Cusumano, G., et al. 2006, Nature, 440, 164

Evans, P. A., et al. 2007, ArXiv e-prints, 704, arXiv:0704.0128

Falcone, A. D., et al. 2006, ApJ, 641, 1010

Fenimore, E. E., in 't Zand, J. J. M., Norris, J. P., Bonnell, J. T., & Nemiroff, R. J. 1995, ApJ, 448, L101

Frail, D. A., et al. 2001, ApJ, 562, L55

Frederiksen, J. T., Hededal, C. B., Haugbølle, T., & Nordlund, Å. 2004, ApJ, 608, L13

Gehrels, N., et al. 2004, ApJ, 611, 1005

Godet, O., et al. 2007, ArXiv Astrophysics e-prints, arXiv:astro-ph/0702262

Granot, J., Nakar, E., & Piran, T. 2003, Nature, 426, 138

Granot, J., Piran, T., & Sari, R. 2000, ApJ, 534, L163

Guetta, D., D'Elia, V., Fiore, F., Conciatore, M. L., Antonelli, A., & Stella, L. 2006, ArXiv Astrophysics e-prints, arXiv:astro-ph/0610512

King, A., O'Brien, P. T., Goad, M. R., Osborne, J., Olsson, E., & Page, K. 2005, ApJ, 630, L113

Kocevski, D., Ryde, F., & Liang, E. 2003, ApJ, 596, 389

Kouveliotou, C., Meegan, C. A., Fishman, G. J., Bhat, N. P., Briggs, M. S., Koshut, T. M., Paciesas, W. S., & Pendleton, G. N. 1993, ApJ, 413, L101

Krimm, H. A., et al. 2007, ArXiv Astrophysics e-prints, arXiv:astro-ph/0702603

Kumar, P., & Panaitescu, A. 2000, ApJ, 541, L51

Kumar, P., et al. 2007, MNRAS, 376, L57

Lee, A., Bloom, E. D., & Petrosian, V. 2000, ApJS, 131, 1

Liang, E. W., et al. 2006, ApJ, 646, 351

MacFadyen, A. I., & Woosley, S. E. 1999, ApJ, 524, 262

Mangano, V., et al. 2007, ArXiv Astrophysics e-prints, arXiv:astro-ph/0701812

Mészáros, P. 2001, Science, 291, 79

Mészáros, P. 2006, Reports of Progress in Physics, 69, 2259

Moretti, A., et al. 2007, ArXiv e-prints, 711, arXiv:0711.3739

Nomoto, K., Tanaka, M., Tominaga, N., Maeda, K., & Mazzali, P. A. 2007, ArXiv e-prints, 707, arXiv:0707.2219

Norris, J. P., Nemiroff, R. J., Bonnell, J. T., Scargle, J. D., Kouveliotou, C., Paciesas, W. S., Meegan, C. A., & Fishman, G. J. 1996, ApJ, 459, 393

O'Brien, P. T., Willingale, R., Osborne, J. P., & Goad, M. R. 2006, New Journal of Physics, 8, 121

Panaitescu, A. 2006, ArXiv Astrophysics e-prints, arXiv:astro-ph/0607396

van Paradijs, J. A. 2001, Black Holes in Binaries and Galactic Nuclei, 316

Perna, R., Armitage, P. J., & Zhang, B. 2006, ApJ, 636, L29

Proga, D., & Zhang, B. 2006, MNRAS, 370, L61

Qin, Y.-P., Xie, G.-Z., Xue, S.-J., Liang, E.-W., Zheng, X.-T., & Mei, D.-C. 2000, PASJ, 52, 759

Rees, M. J., & Mészáros, P. 1994, ApJ, 430, L93

Rosswog, S. 2004, ArXiv Astrophysics e-prints, arXiv:astro-ph/0401022

Rybicki, G. B., & Lightman, A. P. 1979, Radiative Processes in Astrophysics (New York: Wiley)

Ryde, F. 2005, ApJ, 625, L95

Ryde, F., Borgonovo, L., Larsson, S., Lund, N., von Kienlin, A., & Lichti, G. 2003, A&A, 411, L331

Ryde, F., & Petrosian, V. 2002, ApJ, 578, 290

Sari, R., Piran, T., & Halpern, J. P. 1999, ApJ, 519, L17

Sari, R., Piran, T., & Narayan, R. 1998, ApJ, 497, L17

Willingale, R., O'Brien, P. T., Goad, M. R., Osborne, J. P., Page, K. L., & Tanvir, N. R. 2007, ArXiv e-prints, 710, arXiv:0710.3727

Woosley, S. E. 1993, ApJ, 405, 273

Woosley, S. E., & Heger, A. 2006, ApJ, 637, 914

Zhang, B. 2006, 36th COSPAR Scientific Assembly, 36, 77

Zhang, B. 2006, AIP Conf. Proc. 836: Gamma-Ray Bursts in the Swift Era, 836, 392

Zhang, B., Fan, Y. Z., Dyks, J., Kobayashi, S., Mészáros, P., Burrows, D. N., Nousek, J. A., & Gehrels, N. 2006, ApJ, 642, 354

Zhang, Z. B., Xie, G. Z., Deng, J. G., & Wei, B. T. 2007, Astronomische Nachrichten, 328, 99

Appendix A

Data reduction scripts

A.1 batlc.sh

```
 cd 00103647000/bat/hk

src= 'swt00103647000bcbdq.hk.gz'

if [ ! -f $src ]
then
echo "File $src does not exists"
echo "Run BAT_QMap_103647000.sh"
exit 1
elif [ -f $targ ]
then
echo "File $src exists - OK"
fi

#mkdir ../../../00103647000_results
#cd 00103647000/bat/event
cd ../event

batbinevt infile=sw00103647000bevshsp_uf.evt.gz outfile=00103647000.lc
outtype=LC timedel= 0.008 timebinalg=u energybins=15-25,25-50,50-100,100-350
detmask=../hk/swt00103647000bcbdq.hk.gz clobber=YES

echo "**************** NAXIS2 *******"
fkeyprint 00103647000.lc+1 NAXIS2
echo "***************** NAXIS2 *******"

mv 00103647000.lc ../../../
#mv 00103647000.lc ../../../00103647000_results/.

echo "************* TSTART *******"
fkeyprint sw00103647000bevshsp_uf.evt.gz TSTART
echo "*************** TSTART ********"

echo "**************** TRIGTIME *******"
fkeyprint sw00103647000bevshsp_uf.evt.gz TRIGTIME
echo "***************** TRIGTIME *******"

echo "fplot 00103647000.lc offset=yes"
echo "X column = TIME-TRIGTIME"
echo "Y column = RATE[ERROR]"
```

A.2 BAT_QMap.sh

```
 cd 00103647000/bat/event

echo "**** Changed the detmask? ****"
echo "*** Creating Quality Map *****"


batbinevt infile=sw00103647000bevshsp_uf.evt.gz outfile=total.dpi
outtype=DPI timedel=0 timebinalg=u energybins=-
```

```
weighted=NO outunits=COUNTS clobber=YES

bathotpix infile=total.dpi outfile=total.qmap
detmask=../hk/swt0128258618bdecb.fits.gz clobber=YES

cp total.qmap ../hk/swt00103647000bcbdq.hk
gzip ../hk/swt00103647000bcbdq.hk

echo "**** if no enable/disable file available: ******"
echo "****** Start time ********"
ftlist sw00103647000bevshsp_uf.evt.gz K — grep TSTART
echo "*** Find file at
ftp://heasarc.gsfc.nasa.gov/swift/data/trend/YYYY_MM/bat/bdetflag"
```

A.3 time-corr.sh

```
 trigtime=128259002.24

fcalc 00103647000.lc 00103647000_time-corr.lc TIME "TIME-$trigtime" clobber=yes
```

A.4 short.sh

```
 fcopy "00103647000_time-corr.lc[TIME>-2 && TIME<6]"
00103647000_time-corr_short.lc
```

Appendix B

The pulse analysis program `srice2.pro`

B.1 srice2.pro

Different parts of the program and the most important changes that have been made are marked with red. Commands mentioned in section 3.3 are marked with purple.

```
pro xvoigt_ev, event
COMMON Cxvoigt,voigt_base,rslider,xslider,dslider,x0,ymin,x,a,c,r,d,tmax,fmax,tid,
result,data,param,xmin,xmax,field,field2,counts,array,yfit,trigger,file,sigmaa,model,
times,xfwhm,xfwhmerror,xfwtm,t1,t2,yfit2,chisqr,back,curve,lm,setmodel,t90,tmaxs,
midtimes,string,plotwhat,psplot,plottext,n_e,axis,bxis,xfwtm_error

WIDGET_CONTROL, event.id, GET_UVALUE = eventval ev=eventval

CASE eventval OF

"XVOIGT_XRT" : begin
axis='64ms'
bxis=64
file=dialog_pickfile(/read, filter="*xrt")
openr,111,file
slask=' '
readf,111,slask
inputdata=fltarr(2,slask)
readf,111,inputdata
close,111
counts=inputdata(1,*)
times=fltarr(2,n_elements(counts))
x=indgen(n_elements(counts))
times(0,*)=inputdata(0,*)
times(1,*)=times(0,*)
string=strmid(file,2,/reverse_offset)
if string eq 'par' then begin
temp=strsplit(file,'/')
trigger=strmid(file,temp(4),temp(4)-temp(3)-1)
endif else begin
trigger=strmid(file,3,5,/reverse_offset)
endelse
temp=strpos(trigger,0)
if temp eq 0 then begin
trigger=strmid(trigger,1,3)
endif
plottext=0.0
plotwhat=0
end

"XVOIGT_BAT" : begin
axis='BAT'
bxis=999
file=dialog_pickfile(/read, filter="*_time-corr_short.lc")
data1=mrdfits(file,1,header1)
data2=mrdfits(file,2,header2)
arate=data1.rate
atimes=data1.time
```

```
channel=data2.channel
sizechann=size(channel)
no_channels=sizechann(1)
emin=data2.e_min
emax=data2.e_max
aantal=size(atimes)
times=fltarr(2,aantal(1))
times(0,*)=atimes
times(1,*)=times(0,*)
array=arate
data=arate(0,*)+arate(1,*)+arate(2,*)+arate(3,*)
counts=data
string=strmid(file,2,/reverse_offset)
if string eq '.lc' then begin
temp=strpos(file,'00')
test=strmid(file,temp+11,1)
if (test eq '_') then begin
trigger=strmid(file,temp+2,9)
endif endif

plottext=0.0
plotwhat=0
end

"XVOIGT_FIT" : begin
print,'.....fitting.....'
indices=where((times(0,*) ge xmin) and (times(1,*) le xmax),n_i)
w=1/counts(indices)
get_midtimes,times, indices,midtimes,string
konst= param(0)
param2=fltarr(4)
param2(0)=param(1)
param2(1)=param(2)
param2(2)=param(3)
param2(3)=param(4)

yfit=curvefit2(konst,midtimes,counts(indices),w,param2,sigmaa,
function_name='ricemodel3',chi2=chisqr)
model=yfit
a=param
maxcounts=max(counts(indices))
limit=maxcounts/10.
plot_counts,times,counts,xmin,xmax,axis,trigger
oplot, midtimes, model, thick=2,color=150

xyouts,.65,.80,string('t!L0!N =',param(0),'+/-',0),/norm
xyouts,.65,.75,string('r =',param2(0),'+/-',sigmaa(0)),/norm
xyouts,.65,.70,string('d =',param2(1),'+/-',sigmaa(1)),/norm
xyouts,.65,.65,string('tmax =',param2(2),'+/-',sigmaa(2)),/norm
xyouts,.65,.60,string('fmax =',param2(3),'+/-',sigmaa(3)),/norm

mint=times(0,indices(0))+param(0)
maxt=times(1,indices(n_i-1))+50.
resolution=0.01
```

```
antal=((maxt-mint)/resolution)-((maxt-mint) mod resolution)
antal=fix(antal)
modeltimes=fltarr(antal)
modelw=fltarr(antal)
modeltimes(0)=mint-20.
for i=1,antal-1 do begin
modeltimes(i)=modeltimes(i-1)+resolution
endfor

ricemodel3, konst, modeltimes, param2, modelw, pder
nollorw=where(finite(modelw) eq 0,rakna)
if (rakna ne 0) then modelw(nollorw)=-1.0
peak=where(modelw eq max(modelw))
hm=max(modelw(0:*))/2
komst=modelw
komst(0:*)=hm
peak=peak(0)
diffmodel1=abs(modelw(0:peak)-komst(0:peak))
diffmodel2=abs(modelw(peak:*)-komst(peak:*))
i1=(where(min(diffmodel1) eq diffmodel1))
i2=(where(min(diffmodel2) eq diffmodel2))
fwhm=modeltimes(peak+i2)-modeltimes(i1)
oplot, [modeltimes(i1),modeltimes(peak+i2)],[hm,hm],$
linestyle=1,thick=2, color=150
hmerror=SQRT(hm)
xyouts,.65,.55,string('fwhm =',fwhm),/norm
if n_elements(chisqr) ne 0 then begin
xyouts,.65,.45,string('!7v!S!E2!N!3 =!17',chisqr),/norm
endif
tm=max(modelw(0:*))*0.75
komst=modelw
komst(0:*)=tm
peak=peak(0)
diff1=abs(modelw(0:peak)-komst(0:peak))
diff2=abs(modelw(peak:*)-komst(peak:*))
ind1=(where(min(diff1) eq diff1))
ind2=(where(min(diff2) eq diff2))
fwtm=modeltimes(peak+ind2)-modeltimes(ind1)
oplot, [modeltimes(ind1),modeltimes(peak+ind2)],[tm,tm], $
linestyle=2,thick=2, color=150
xfwtm_error=1.41*sigmaa(2)
xyouts,.65,.50,string('!17fw.75m = ',fwtm),/norm,size=0.9
xyouts,.85,.50,string('!17+/- ',xfwtm_error),/norm,size=0.9
xyouts,.85,.55,string('!17+/- ',xfwtm_error),/norm,size=0.9
xfwhm=fwhm
xfwtm=fwtm

;print,'t_0 = ',param(),'+-',sigmaa(0)
print,'r = ',param2(0),'+- ',sigmaa(0)
print,'d = ',param2(1),'+- ',sigmaa(1)
print,'t_max = ',param2(2),'+- ',sigmaa(2)
print,'f_max = ',param2(3),'+- ',sigmaa(3)
print, 'fwhm =',fwhm,'+- ',hmerror
print,'FW75% =',xfwtm,'+- ',xfwtm_error
```

```
print, 'chisqr = ',chisqr
return
end

"XVOIGT_SAVE" : begin
writefile='laganalysis.dat'
openw,80,writefile,/append
openw,90,'fits_to_pulses.dat',/append
printtrigger=float(trigger)+float(plottext)/10.
printdata=bxis
printf,90,printtrigger,printdata,param,sigmaa,chisqr
slask=fltarr(4)
slask=[param(3),sigmaa(3),xfwtm,xfwtm_error]
printf,80,printtrigger,printdata,slask
close,80
close,90
Print, 'Fit data saved to ', writefile
return
end

"XVOIGT_PRINT" : begin
set_plot, 'ps'
device, filename='idl_temp.ps'
psplot=1
voigt_show
psplot=0
device, /close
set_plot, 'x'
print, 'plot sent to printer'
return
end

"XVOIGT_EXIT" : begin
WIDGET_CONTROL, event.top, /DESTROY
return
end

"XVOIGT_REDRAW" : begin
widget_control, field,get_value=x1
widget_control, field2,get_value=x2
end

"XVOIGT_SUM" : begin
plottext=0.
plotwhat=5
end

"XVOIGT_CHAN1" : begin
plottext=1.0
plotwhat=1
end

"XVOIGT_CHAN2" : begin
plotwhat=2
```

```
plottext=2.0
end

"XVOIGT_CHAN3" : begin
plottext=3.0
plotwhat=3
end

"XVOIGT_CHAN4" : begin
plotwhat=4
plottext=4.0
end

"c_slider": begin
c=event.value
end
"r_slider": begin
r=event.value
end
"d_slider": begin
d=event.value
end
"tmax_slider": begin
tmax=event.value
end
"fmax_slider": begin
fmax=event.value
end

else : begin
dpar=2.
r=4.
message, "Event User Value Not Found"
return
end
endcase

widget_control, field,get_value=xmin
widget_control, field2,get_value=xmax
voigt_show
return
end

pro plot_counts,times,counts,xmin,xmax,axis,trigger
indices=where((times(0,*) ge xmin) and (times(1,*) le xmax),n_i)
maxcounts=max(counts(indices))
limit=maxcounts/10.
maxN=size(times)

if axis eq 'BAT' then begin
plot,[0,0],[0,0],xrange=[xmin-1,xmax+1],
yrange=[0.,maxcounts+limit], title=trigger+axis,
xtitle='Time (sec)', ytitle='Photon Flux (cm!E-2!N sec!E-1!N)'
for i=0,maxN(2)-2 do begin
```

```
oplot,[(times(0,i)+times(1,i))/2,
(times(0,i+1)+times(1,i+1))/2],[counts(i),counts(i+1)]
endfor
endif

if axis eq 'XRT' then begin
plot, times(0,*),counts, xrange=[xmin-1,xmax+1],
yrange=[0.,maxcounts+limit],title=trigger+axis, xtitle='Time(sec)',
ytitle='Counts',xstyle=1,ystyle=1
endif
end

pro get_midtimes,times,indices,midtimes,string
midtimes=fltarr(n_elements(times(indices)))
if string eq 'par' then begin
midtimes=0.5*(times(0,indices)+times(1,indices))
endif else begin
midtimes=times(0,indices)
endelse
end

pro readydata_notrig, data, array, back, barray, error, file
temp=strpos(file,'cat')
directory=strmid(file,0,temp)
trigger=strmid(file,3,5,/reverse_offset)
temp=strpos(trigger,0)
temp=fix(temp)
if temp eq 0 then begin
trigger=strmid(trigger,1,3)
endif

data=read_64ms(trigger,array=array,dir=directory)
back=back_64ms(trigger,barray=barray)
data=data-back
array(0,*)=array(0,*)-barray(0,*)
array(1,*)=array(1,*)-barray(1,*)
array(2,*)=array(2,*)-barray(2,*)
array(3,*)=array(3,*)-barray(3,*)
error=data+back
return
end

pro voigt_show
COMMON Cxvoigt,voigt_base,rslider,xslider,dslider,x0,ymin,x,a,c,r,d,tmax,fmax,tid,
result,data,param,xmin,xmax,field,field2,counts,array,yfit,trigger,file,sigmaa,model,
times,xfwhm,xfwhmerror,xfwtm,t1,t2,yfit2,chisqr,back,curve,lm,setmodel,t90,tmaxs,
midtimes,string,plotwhat,psplot,plottext,n_e,axis,bxis,xfwtm_error

if (plotwhat eq 1) then begin
counts(*)=array(0,*)
endif
if (plotwhat eq 2) then begin
counts(*)=array(1,*)
endif
```

```
if (plotwhat eq 3) then begin
counts(*)=array(2,*)
endif
if (plotwhat eq 4) then begin
counts(*)=array(3,*)
endif
if (plotwhat eq 5) then begin
counts=data
endif

tid=fltarr(1000)
xmin=xmin(0)
xmax=xmax(0)
if xmin lt times(0,0) then xmin=times(0,0)
if xmax eq 0. then xmax=times(1,n_elements(times(1,*))-1)
if xmax gt times(1,n_elements(times(1,*))-1) then
xmax=times(1,n_elements(times(1,*))-1)
indices=where((times(0,*) ge xmin) and (times(1,*) le xmax),n_i)
param=fltarr(5)
param(0)=c
param(1)=r
param(2)=d
param(3)=tmax
param(4)=fmax

string=strmid(file,2,/reverse_offset)
mint=times(0,indices(0))+param(0)
maxt=times(1,indices(n_i-1))+100.
resolution=0.001
antal=((maxt-mint)/resolution)-((maxt-mint) mod resolution)
if antal gt 10000. then begin
resolution=0.1
antal=((maxt-mint)/resolution)-((maxt-mint) mod resolution)
endif
antal=fix(antal)
modeltimes=fltarr(antal)
modelz=fltarr(antal)
modeltimes(0)=mint-10.
for i=1,antal-1 do begin
modeltimes(i)=modeltimes(i-1)+resolution
endfor

ricemodel, modeltimes, param, modelz, pder
plot_counts,times,counts,xmin,xmax,axis,trigger
oplot, modeltimes, modelz
xyouts,0.01,0.01,string('r=',r),/norm
xyouts,.25,0.01,string('d=',d),/norm
xyouts,.50,.01,string('tmax=',tmax),/norm
xyouts, .75,0.01,string('fmax=',fmax),/norm

get_midtimes,times,indices,midtimes,string
if plotwhat eq 5 then begin
for qq=0,2,2 do begin
oplot, midtimes, array(qq,indices),linestyle=2,thick=qq+1
```

```
endfor
endif
if psplot eq 1 then return
end

pro srice2
device,/pseudo_color
COMMON Cxvoigt,voigt_base,rslider,xslider,dslider,x0,ymin,x,a,c,r,d,tmax,fmax,tid,
result,data,param,xmin,xmax,field,field2,counts,array,yfit,trigger,file,sigmaa,model,
maxN,times,xfwhm,xfwhmerror,t1,t2,yfit2,chisqr,back,curve,lm,setmodel,t90,tmaxs,
midtimes,string,plotwhat,psplot,plottext,n_e,axis,bxis,xfwtm_error
plottext=0.0
psplot=0
r=1.7
x0=12
d=double(2.3)
tmax=0.5
fmax=1.1
c=0.9
voigt_base = WIDGET_BASE(TITLE = "GRB Pulse") ; create the main base
r_base = WIDGET_BASE(voigt_base,/row)
c_base = WIDGET_BASE(r_base,/column)
rc_base = WIDGET_BASE(c_base,/row)

channels=['"Channels"   ', '"Sum" XVOIGT_SUM', '"Channel 1" XVOIGT_CHAN1',
'"Channel 3" XVOIGT_CHAN3','']

File=['"File"   ', 'Load" ','"BAT" XVOIGT_BAT', '"XRT" XVOIGT_XRT', ,
'"Save"XVOIGT_SAVE','"Print" XVOIGT_PRINT', '"Exit"XVOIGT_EXIT','']

XPdMenu, [ File, '" Fit "XVOIGT_FIT', channels, '" Redraw " XVOIGT_REDRAW'],
c_base ; top buttons
field=CW_FIELD(c_base, Title="xmin",/frame,value=0.)
field2=CW_FIELD(c_base,Title="xmax",/frame,value=0.)
xmin=0.
xmax=0.

cslider = CW_FSLIDER(c_base, $ ;slider for c parameter
XSIZE = 256, $
MINIMUM = -80.0, $
MAXIMUM = 10.0, $
VALUE = c, $
/DRAG, /EDIT, $
TITLE = 'c value', $
UVALUE = "c_slider")

rslider = CW_FSLIDER(c_base, $ ; slider for r parameter
XSIZE = 256, $
MINIMUM = 0.01, $
MAXIMUM = 20.0, $
VALUE = r, $
/DRAG, /EDIT, $
TITLE = 'r value', $
UVALUE = "r_slider")
```

```
dslider = CW_FSLIDER(c_base, $ ; slider for d value
XSIZE = 256, $
MINIMUM = 0.01, $
MAXIMUM = 10.0, $
VALUE = d, $
/DRAG, /EDIT, $
TITLE = 'd value', $
UVALUE = "d_slider")

tmaxslider = CW_FSLIDER(c_base, $ ;slider for tmax parameter
XSIZE = 256, $
MINIMUM = 0, $
MAXIMUM = 100.0, $
VALUE = tmax, $
/DRAG, /EDIT, $
TITLE = 'tmax value', $
UVALUE = "tmax_slider")

fmaxslider = CW_FSLIDER(c_base, $ ;slider for the fmax parameter
XSIZE = 256, $
MINIMUM = 1E-1, $
MAXIMUM = 10, $
VALUE = fmax, $
/DRAG, $
/EDIT, $
TITLE = 'fmax value', $
UVALUE = "fmax_slider")

draw = WIDGET_DRAW(r_base, $ ; drawing window
XSIZE=600, $
YSIZE=450)

WIDGET_CONTROL, voigt_base, /REALIZE ; create the widgets
xyouts,100,300,'!17Stanford-Rice GRB Analysis Package', charsize=2,
charthick=1,/device
xyouts,200,250,'I: Light Curve Fitting',charsize=1.5,
charthick=1,/device
xyouts,220,200,'Load a Data File! ',charsize=1.5,charthick=1,/device
XManager, "xvoigt", voigt_base, $ ; start background process
EVENT_HANDLER = "xvoigt_ev", $
GROUP_LEADER = GROUP
return
end
```

Appendix C

BAT and XRT light curves

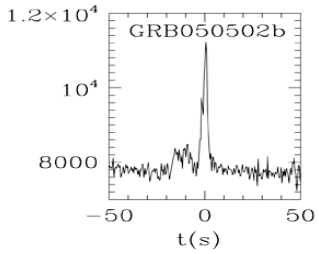

BAT light curve of GRB 050502B

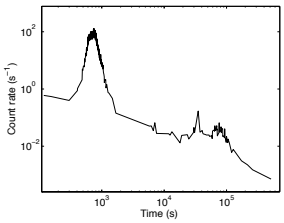

XRT light curve of GRB 050502B

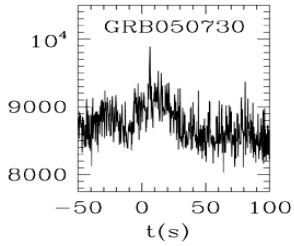

BAT light curve of GRB 050730

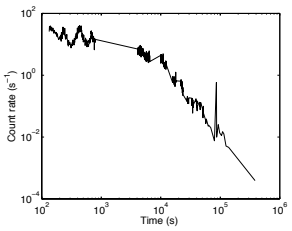

XRT light curve of GRB 050730

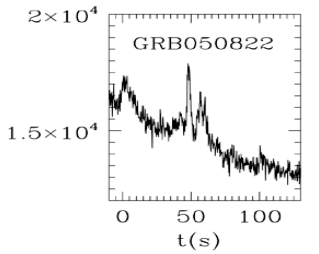

BAT light curve of GRB 050822

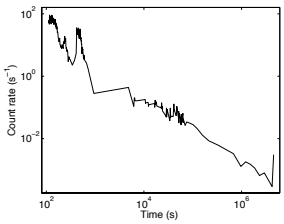

XRT light curve of GRB 050822

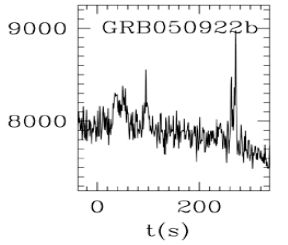

BAT light curve of GRB 050922B

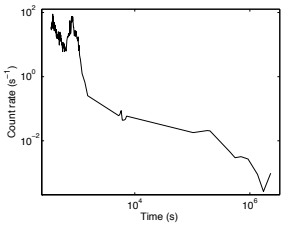

XRT light curve of GRB 050922B

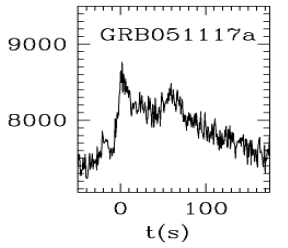

BAT light curve of GRB 051117A

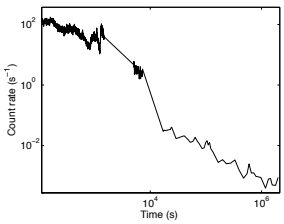

XRT light curve of GRB 051117A

Figure C.1: BAT and corresponding XRT light curves. Note that there is no unit of the BAT light curves. These light curves are from the *Swift* web site. It is not necessary to have correct units since it only is emission episodes that are of interest, not the actual count rates.

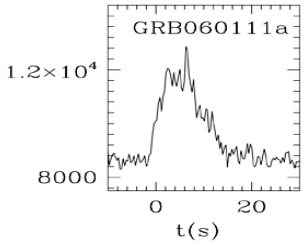

BAT light curve of GRB 060111A

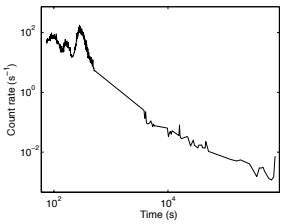

XRT light curve of GRB 060111A

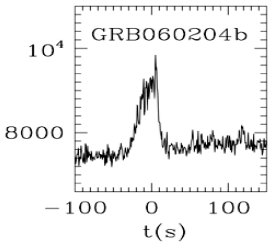

BAT light curve of GRB 060204B

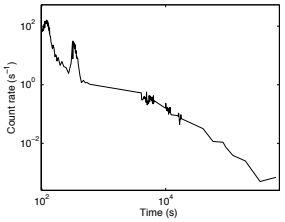

XRT light curve of GRB 060204B

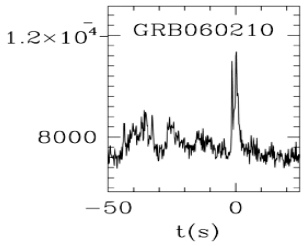

BAT light curve of GRB 060210

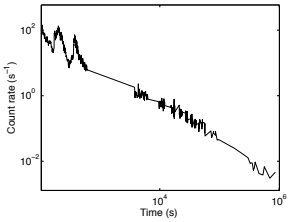

XRT light curve of GRB 060210

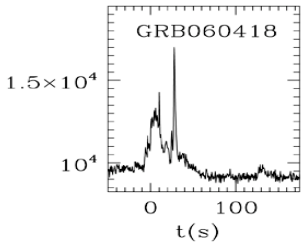

BAT light curve of GRB 060418

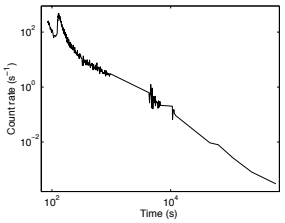

XRT light curve of GRB 060418.

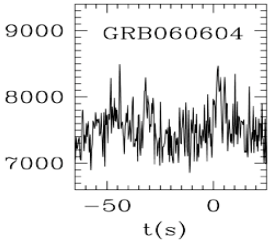

BAT light curve of GRB 060604

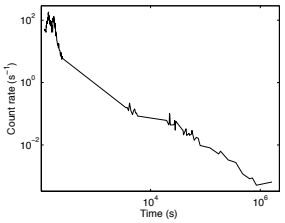

XRT light curve of GRB 060604

Figure C.1: (continued)

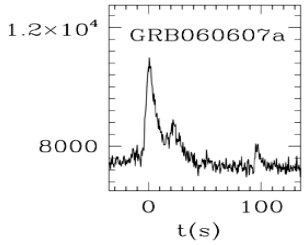

BAT light curve of GRB 060607A

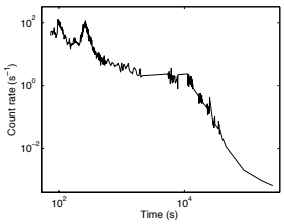

XRT light curve of GRB 060607A

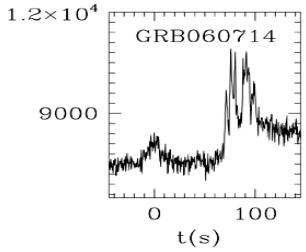

BAT light curve of GRB 060714

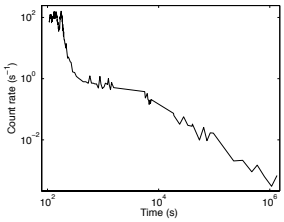

XRT light curve of GRB 060714

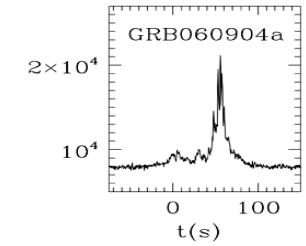

BAT light curve of GRB 060904A

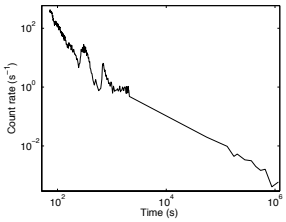

XRT light curve of GRB 060904A

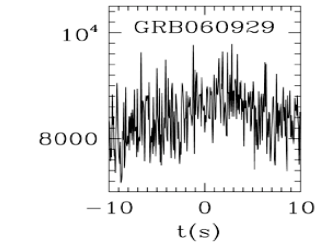

BAT light curve of GRB 060929

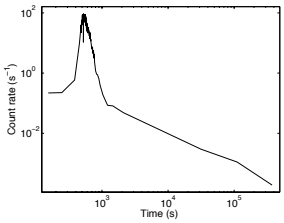

XRT light curve of GRB 060929

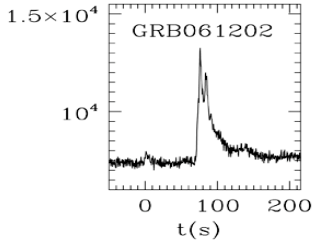

BAT light curve of GRB 061202

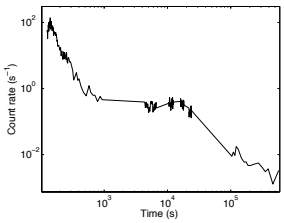

XRT light curve of GRB 061202

Figure C.1: (continued)

Appendix D

XRT light curves with assumed power law emission and background subtracted flares

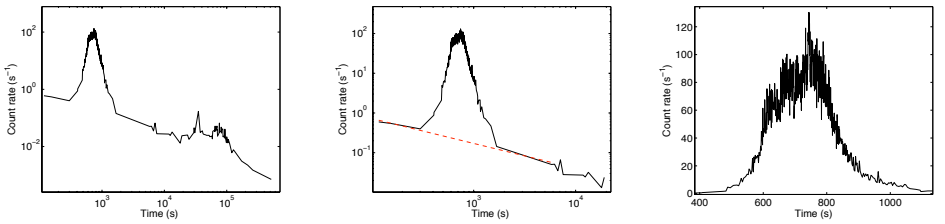

(a) GRB 050502B

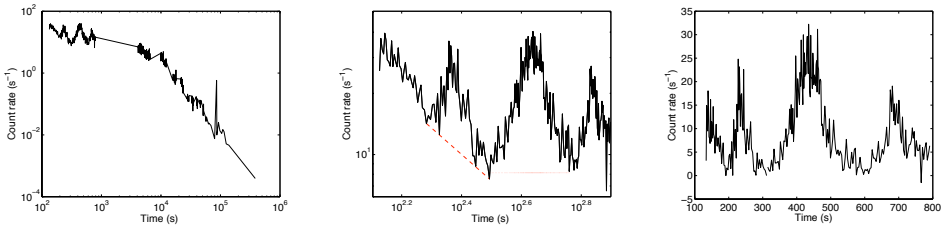

(b) GRB 050730

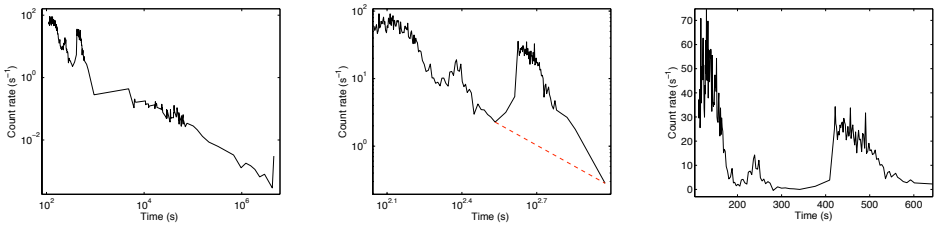

(c) GRB 050822

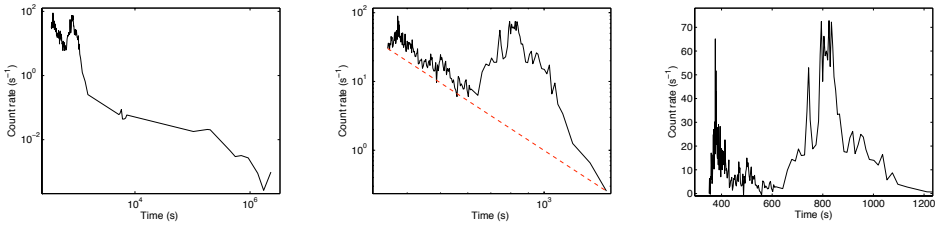

(d) GRB 050922B

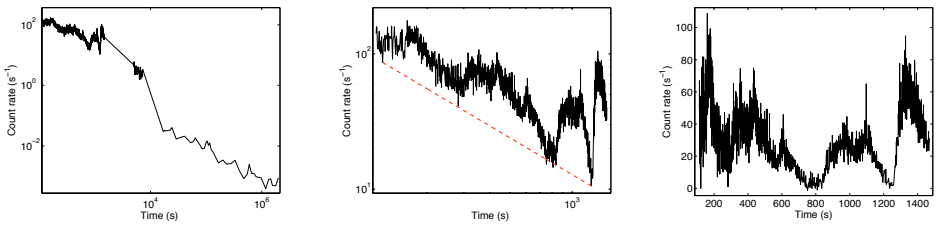

(e) GRB 051117A

Figure D.1: The left column shows the X-ray light curves of the bursts in the X-ray flare sample. The column in the middle shows the flares from the light curves zoomed in, with a red dashed line indicating the assumed underlying background, that is to be subtracted. To choose the background of the flares it is a good thing to look at the whole light curve. The right column shows the background subtracted X-ray flares, which are to be fitted in `srice2.pro`.

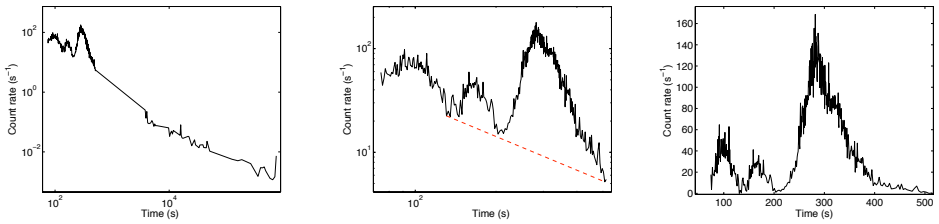

(f) GRB 060111A

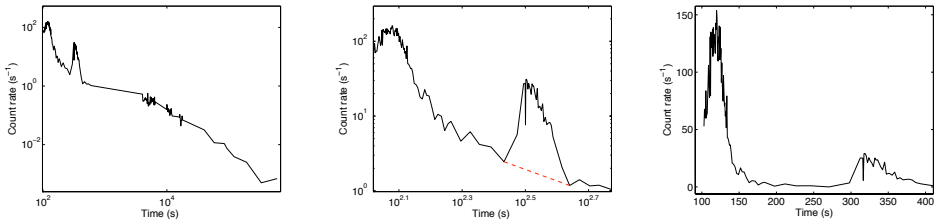

(g) GRB 060204B

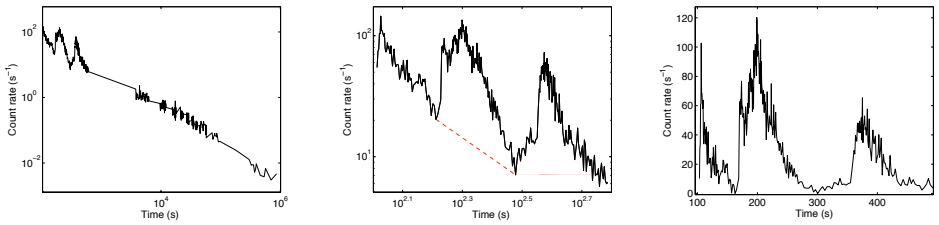

(h) GRB 060210

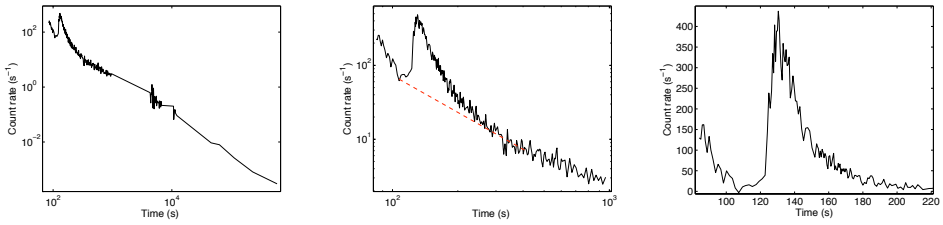

(i) GRB 060418

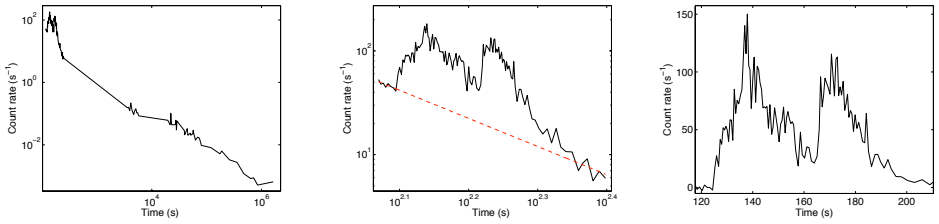

(j) GRB 060604

Figure D.1: (continued)

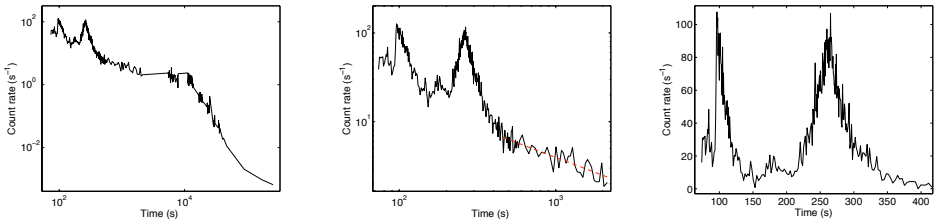

(k) GRB 060607A

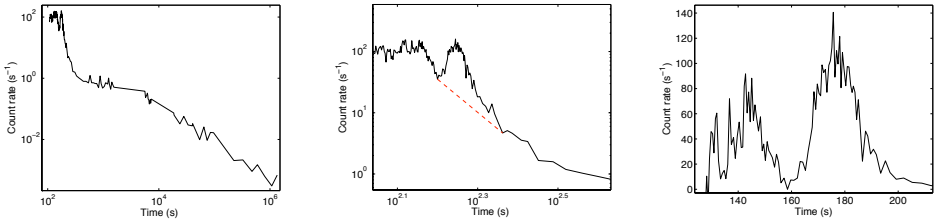

(l) GRB 060714

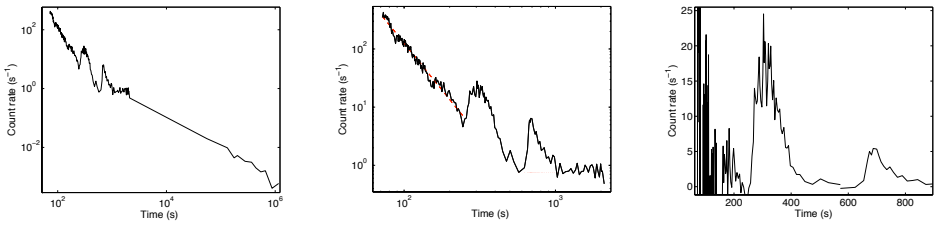

(m) GRB 060904A

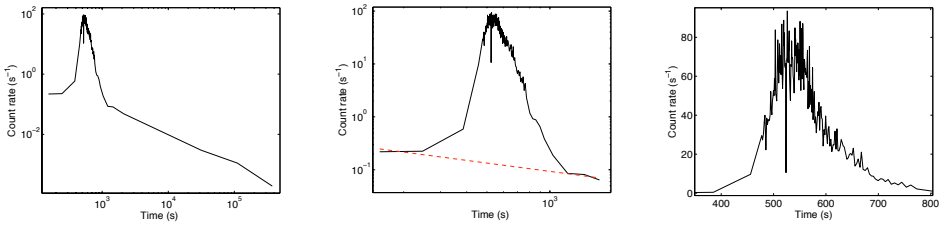

(n) GRB 060929

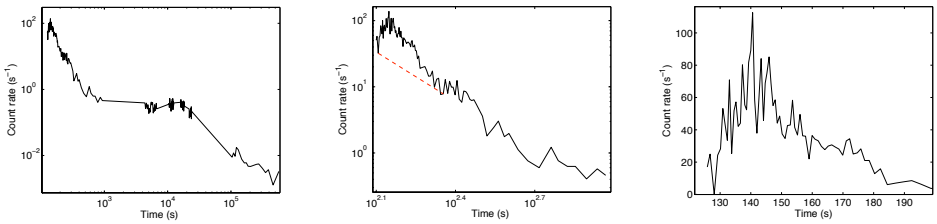

(o) GRB 061202

Figure D.1: (continued)

Appendix E

BAT and XRT fit parameters

GRB	*Trigger number*	*Pulse*	Good pulse	c (s)	r	d	t_{max} (s)	f_{max} (Counts/s)	$FWHM$ (s)	$FW75\%$ (s)	χ^2
050124	103647	1		0.9	2.6±1.5	3.5±2.9	0.2±0.2	67±20	1.3±0.3	0.8±0.3	0.09
		2		2.0	1.1±2.2	5.0±52.6	2.4±0.3	48±20	0.8±0.4	0.5±0.4	0.10
050318	111529			0.5	2.5±5.5	5.8±13.5	0.8±0.5	4.8±2.0	1.3±0.7	0.8±0.7	0.05
050401	113120			-22.6	3.3±4.0	1.3±3.2	24.8±0.6	18.6±4.3	3.5±0.9	1.9±0.9	0.09
050416B	114797			1.3	4.0±1.6	2.7±5.5	0.5±0.2	39.0±5.0	1.7±0.3	1.0±0.3	-0.06
050603	131560	1		3.4	2.2±0.9	3.4±3.3	-2.7±0.1	75±15	0.9 ±0.2	0.5 ±0.2	0.21
		2		1.3	3.7±1.9	2.0±1.8	-0.8±0.1	100±20	0.6±0.1	0.4±0.1	0.27
		3	*	0.1	1.6±0.8	2.9±1.4	0.2±0.0	329±45	0.4±0.0	0.3±0.0	0.29
051109A	163136			3.8	2.9±3.6	7.0±22.3	1.2±1.2	2.7±1.1	4.3±1.7	2.7±1.7	0.01
051111	163438		*	8.3	2.0±0.8	3.7±2.2	1.1±1.5	3.1±1.0	11.9±2.1	7.3±2.1	0.02
051113	163765			35.9	0.9±0.8	2.0±2.5	-29.1±2.7	0.50±0.16	16.6±3.8	9.7±3.8	-0.00
060117	177666			0.5	2.0±3.1	2.2±1.0	0.4±0.2	181±10	1.5±0.3	0.9±0.3	0.03
060206	180455		*	1.7	3.8±1.0	5.9±3.0	2.3±0.3	12.4±3.3	3.0±0.4	1.9±0.4	-0.01
060306	200638			-42.0	3.7±6.5	0.8±0.5	43.1±0.4	3.8±2.0	2.6±0.6	1.2±0.6	-0.04
060428A	207364		*	-1.1	2.8±6.2	2.7±5.6	4.6±1.2	2.6±1.0	4.0±1.7	2.4± 1.7	0.01
060719	220020			0.9	1.7±2.3	2.3±4.0	0.5±0.6	1.2±0.5	2.4±0.9	1.4±0.9	-0.01
060814	224552	1	*	-56.8	2.6±1.6	2.8±1.9	69.5±2.3	1.9±0.5	15.3±3.2	9.1±3.2	0.01
		2	*	-120.0	4.6±17.0	3.1±14.0	129.5±4.6	0.6±0.5	7.9±6.5	4.7±6.5	0.01
060904B	228006			4.2	5.1±5.1	2.8±6.6	1.8±1.3	1.0±0.5	5.1±1.8	3.0±1.8	-0.03
060908	228581		*	-8.2	2.7±5.6	4.2±38.0	10.1±0.8	4.3±2.5	1.9±1.2	1.2±1.2	0.02
060912A	229185		*	0.5	2.0±1.3	1.4±0.4	0.2±0.2	26.3±7.5	1.4±0.2	0.8±0.2	0.01
060919	230115			2.6	3.0±3.0	2.6±7.2	-0.2±0.8	3.3±1.3	2.2±1.2	1.5±1.2	0.02
061019	234516			5.0	1.4±0.8	2.3±2.1	2.8±1.9	0.27±0.14	14.6±2.7	8.7±2.7	-0.06
061021	234905		*	-1.6	1.3±1.4	2.1±3.2	2.8±0.4	13.3±3.3	2.5±0.6	1.5±0.6	0.01
061121	239899			3.4	2.7±5.1	7.3±42.2	1.9±1.6	2.2±1.0	4.7±2.3	3.0±2.3	0.01
061126	240766			-17.6	3.4±1.8	2.8±2.1	21.1±0.7	5.0±1.3	3.6±0.9	2.2±0.9	0.02
061222A	252588		*	-24.7	4.2±7.0	1.2±0.9	25.8±0.5	4.0±2.5	1.7±0.7	0.9±0.7	0.01

Table E.1: The obtained parameters from the fits with `srice2.pro` for the pulses in the BAT sample.

GRB	*Trigger number*	*Pulse*	c (s)	r	d	t_{max} (s)	f_{max} (Counts/s)	$FWHM$ (s)	$FW75\%$ (s)	χ^2
050502B	116116		-755.6	1.5 ± 0.1	3.6 ± 0.3	763.5 ± 1.4	96.0 ± 1.1	12.3 ± 0.2	76.2 ± 2.1	1.3
050730	148225	1	-196.3	6.4 ± 1.0	3.2 ± 0.6	232.3 ± 1.3	16.9 ± 1.5	25.0 ± 1.9	14.7 ± 1.9	2.6
		2	-343.1	2.5 ± 0.4	6.1 ± 1.5	431.2 ± 2.1	24.3 ± 1.0	86.7 ± 2.9	54.5 ± 3.0	1.1
		3	-620.6	2.2 ± 0.6	2.6 ± 1.5	683.4 ± 4.9	11.7 ± 0.9	85.5 ± 6.9	51.0 ± 6.9	1.1
050822	151486		-399.1	1.6 ± 0.3	1.6 ± 0.3	440.9 ± 2.6	27.7 ± 1.2	84.2 ± 3.7	47.4 ± 3.7	1.0
050922B	156434		-340.8	5.6 ± 1.2	1.6 ± 0.5	376.1 ± 1.6	22.9 ± 1.3	40.6 ± 2.2	21.6 ± 2.2	3.6
051117A	164268	1	-135.1	1.4 ± 0.1	2.5 ± 0.4	170.4 ± 0.9	66.4 ± 1.3	64.6 ± 1.3	38.7 ± 1.3	5.1
		2	-297.2	1.7 ± 0.1	1.5 ± 0.2	381.6 ± 1.8	61.8 ± 0.8	171.5 ± 2.6	95.3 ± 2.6	1.8
		3	-306.4	1.1 ± 0.1	1.9 ± 0.3	383.2 ± 2.0	61.0 ± 0.8	173.0 ± 2.9	100.5 ± 2.9	1.8
060111A	176818	1	- 45.0	4.5 ± 0.4	6.2 ± 1.5	98.0 ± 0.9	42.9 ± 1.3	35.3 ± 1.2	21.9 ± 1.2	2.3
		2	-137.3	2.8 ± 0.4	2.5 ± 1.0	163.4 ± 1.3	28.3 ± 1.5	31.5 ± 1.9	18.6 ± 1.9	1.9
		3	-221.9	1.9 ± 0.1	3.9 ± 0.3	285.5 ± 0.6	117.8 ± 1.3	83.1 ± 0.9	51.4 ± 0.9	1.8
060204B	180241	1	-95.4	1.8 ± 0.1	8.6 ± 1.5	119.8 ± 0.3	131.4 ± 2.5	25.9 ± 0.4	16.5 ± 0.4	2.1
		2	-285.3	2.4 ± 0.6	3.8 ± 1.4	327.2 ± 2.1	21.9 ± 1.4	48.5 ± 2.9	29.8 ± 2.9	1.9
060210	180977	1	-103.2	1.3 ± 0.2	1.2 ± 0.5	106.6 ± 0.3	68.1 ± 3.5	9.3 ± 0.4	5.0 ± 0.4	2.3
		2	-168.4	1.5 ± 0.1	3.3 ± 0.5	197.2 ± 0.6	84.6 ± 1.8	46.2 ± 0.8	28.4 ± 0.8	1.9
		3	-348.0	1.7 ± 0.2	2.3 ± 0.4	374.9 ± 1.0	46.6 ± 1.5	44.2 ± 1.4	26.2 ± 1.4	1.5
060418	205851		-100.7	6.4 ± 0.2	2.2 ± 0.0	120.5 ± 0.1	376.3 ± 5.2	17.2 ± 0.2	9.6 ± 0.2	3.9
060604	213486	1	-113.5	1.4 ± 0.1	3.3 ± 0.9	128.3 ± 0.4	91.1 ± 2.2	24.2 ± 0.6	14.8 ± 0.6	3.9
		2	-150.3	2.0 ± 0.2	3.1 ± 0.3	161.4 ± 0.2	98.4 ± 2.9	15.0 ± 0.3	9.1 ± 0.3	1.9
060607A	213823	1	-116.0	9.1 ± 1.4	1.2 ± 0.1	127.2 ± 0.3	99.8 ± 3.6	13.8 ± 0.4	6.5 ± 0.4	1.4
		2	-193.2	1.8 ± 0.1	5.0 ± 0.6	238.9 ± 0.7	74.6 ± 1.3	58.3 ± 0.9	36.6 ± 0.9	2.0
060714	219101		-156.1	3.0 ± 0.2	5.8 ± 0.6	175.7 ± 0.2	107.5 ± 2.6	17.2 ± 0.4	10.8 ± 0.4	2.2
060904A	227996	1	-247.7	3.4 ± 0.9	5.2 ± 2.7	360.2 ± 4.8	17.2 ± 1.1	93.0 ± 6.7	57.7 ± 6.7	0.6
		2	-693.1	2.0 ± 1.1	1.7 ± 0.9	734.9 ± 8.9	5.3 ± 1.0	72.4 ± 12.5	41.2 ± 12.5	0.0
060929	231702		-433.5	2.0 ± 0.1	4.4 ± 0.6	532.4 ± 1.3	65.0 ± 1.0	121.0 ± 1.8	75.3 ± 1.8	3.1
061202	241963		-124.5	1.2 ± 0.2	3.0 ± 0.8	141.3 ± 0.8	61.6 ± 1.9	31.3 ± 1.1	19.1 ± 1.1	3.8

Table E.2: The obtained parameters from the fits with `srice2.pro` for the X-ray flares in the XRT sample.